THE UNIVERSITY OF CHICAGO

NEXT GENERATION SYNTHETIC ROUTES TO COLLOIDAL III-V QUANTUM DOTS

A DISSERTATION SUBMITTED TO

THE FACULTY OF THE DIVISION OF THE PHYSICAL SCIENCES

IN CANDIDACY FOR THE DEGREE OF

DOCTOR OF PHILOSOPHY

DEPARTMENT OF CHEMISTRY

BY

VISHWAS SRIVASTAVA

CHICAGO, ILLINOIS

AUGUST 2018

TABLE OF CONTENTS

List of Figures

List of Tables

Acknowledgements

First and foremost, I wish to thank Professor Dmitri V. Talapin for his guidance, encouragement and support as an advisor throughout my graduate work. I was particularly inspired from his enthusiasm and dedication towards science and discovery. I also thank the other members of my thesis committee, Professor Gregory S Engel and Professor John S Anderson, for their thoughtful advice and motivation on many occasions during these five years.

My journey at the University of Chicago has been enriched from my interaction with a wonderful set of people both inside and outside of the laboratory. I am thankful to Dr Wenyong Liu, my first mentor in the Talapin laboratory who introduced me to the world of III-V nanocrystals. Thanks are due to my seniors in the lab Prof. Matthew Panthani, Prof. Jaeyoung Jang, Dr. Chunxing She, Dr Dmitriy Dolzhnikov, Dr. Hao Zhang, Dr. Michael Boles and Dr. J. Matthew Kurley who let my find my own feet in the lab. Special thanks are due to Dr. Igor Fedin who not only made me feel at home with his great sense of humor, but was also someone I could always go to when I needed scientific advice. I was fortunate to make some truly wonderful friends in my labmates Patrick Cunningham, Eric Janke, Maggie Hudson, Vladislav Kamysbayev, Dr. Abhijit Hazarika, Dr. Yuanyuan Wang, Dr. Xinzheng Lan, and Jake Russel. The coffee walks to the Divinity School, lab soccer games and group outings were always great stress busters. I am also grateful to my colleagues Dr. Igor Coropceanu, Dr. Jianwei Nai, Dr. Tae Kyu An, Dr. Ke Gong, Joshua Portner, Jia Ahn Pan, Wooje Cho, Eleanor Dunietz, Kavan Mulloy, Stephanie Diaz, Hannah Muir, Dr. João Batista Souza and Dr. Daniel Haubold.

The research outlined in this thesis would not be possible without the use of all the departmental facilities. I particularly thank Dr. Alexander Filatov, Dr. Justin Jureller, Dr. Jotham Austin and Dr. Yimei Chen for their help with a variety of facilities on countless occasions. I am

also thankful to my collaborators at Argonne National Laboratories Prof. Richard Schaller, Dr. Benjamin Diroll, Dr Tijana Rajh, Dr. Byeongdu Lee, Dr. Chengjun Sun and Dr. Olaf Borkeiwicz for their help and assistance with ultrafast spectroscopy and X-ray scattering measurements. Finally, I wish to recognize Tanya Shpigel for her assistance with obligations outside of research.

My journey through these 5 long years would have been incomplete without my friends outside of the academic realm. One or the other of these amazing people was always there to take me out of the frustration of research. In a chronological order of their appearance in my life, I would like to thank Krithika Mohan, Manas Sajjan, Soudeep Deb, Kushal Kumar Dey, Sayar Karmakar, Luke Hwang, Swati, Sumitra Badrinathan, Dr. Sabyasachi Chatterji, Piyush Arya, Debsouri Kundu and Preeti Poddar.

Finally, it's the constants of my life, I wish to acknowledge. The innumerable sacrifices that my parents have made, no achievement of mine can match them. My sister, Shraddha, has been my biggest source of joy since the day she was born! My grandparents have been instrumental in instilling in me the values of life. I was also fortunate to add a few new members to what I call family, my in-laws, who have also contributed to this journey significantly. Last but not the least, Nitya, now my wife, I am eternally grateful for your constant companionship through thick and thin.

Abstract

Colloidal semiconductor nanocrystals (NCs) or Quantum Dots (QDs) have seen tremendous development in the past 25 years as solution processed semiconductors for optoelectronic applications. While colloidal semiconductors of the II-VI family have reached the stage of commercialization, their III-V cousins, arguably the most important class of semiconductors, are still lagging behind in their colloidal form. One such class of semiconductors is the III-V compounds such as InP, InAs, GaAs, GaP etc. In this thesis, I present my work on the development of new synthetic methodologies for a variety of III-V semiconductors such as InAs, GaAs, $In_xGa_{1-x}P$, $In_xGa_{1-x}As$ etc. These new methodologies enable the preparation of high quality III-V QDs whose structural and optical properties are then studied from the perspective of their applications in optoelectronic devices.

In Chapters 2 and 3, novel syntheses of InAs QDs from aminoarsine precursors are discussed. In Chapter 2, the activation of aminoarsines using a reducing agent for the synthesis of InAs QDs is discussed and this general synthetic route for the synthesis of other arsenide materials is explored. In Chapter 3, the role of reducing agents in governing the precursor conversion kinetics is elucidated and an improved reaction scheme for the synthesis of monodisperse InAs QDs is shown. The emission properties of these near-IR emitting materials are also demonstrated by growing appropriate wide band gap shells on them.

In Chapter 4, the synthesis and properties of colloidal GaAs NCs are discussed. It describes a novel synthesis protocol for colloidal GaAs nanocrystals for a range of sizes and discusses the structural properties of the NCs obtained via this approach. The anomalous optical properties of GaAs are rationalized from a structural point of view.

Chapter 5 is devoted to the exploration of nanocrystal colloids in molten salts and ionic liquids. The dispersions of NCs, III-V and others, are prepared in a variety of molten salt eutectics and their physical state is probed in depth via synchrotron X-ray scattering studies. These measurements help gain a better understanding of the mechanism of stabilization of NCs in molten salts and ionic liquids and demonstrate their potential as non-traditional solvents for colloidal chemistry.

In Chapters 6 and 7, I discuss the applications of molten salts as high temperature solvents for the synthesis and processing of colloidal III-V QDs. A defect annealing protocol for GaAs QDs using molten salts as high temperature solvents is proposed in Chapter 6. The annealing of defects at high temperature was shown to improve the optical properties of GaAs NCs. Chapter 7 describes the synthesis of ternary III-V alloy QDs ($In_xGa_{1-x}P$ and $In_xGa_{1-x}As$) in molten salts via a cation exchange approach. It is demonstrated that molten salts enable the formation of these alloys which are otherwise difficult to synthesize via direct colloidal routes. These QDs show quantum confined absorption and emission features. The optical properties of these alloy nanocrystals are studied in depth and the potential of InGaP QDs as a material for display applications is assessed in comparison to InP QDs.

Parts of this document have been published or are under preparation for publication in peer-reviewed journals.

Chapter 1.

An Introduction to colloidal semiconductor nanocrystals

Since the discovery of quantum confinement effects in semiconductor nanocrystallites in the 1980s,[1-2] chemists all over the world have been working to perfect the synthesis of colloidal nanocrystals of semiconductor compounds using a bottom-up approach. These nanocrystals (NCs), consisting of a few hundred atoms show properties that are drastically different from their bulk analogs, thus making them special.[3-4] For example, the band gap of bulk cadmium selenide (CdSe) is 1.74 eV, however when synthesized at the nanoscale, their band-gap shows a size dependent change (increasing band gap with decreasing size) below the Bohr-exciton diameter according to the Brus Equation.[4]

$$\Delta E(r) = E_g + \frac{h^2}{8r^2}\left(\frac{1}{m_e^*} + \frac{1}{m_h^*}\right)$$

This special property of quantum confined semiconductors, also called quantum dots (QDs) makes them attractive building blocks for a variety of optoelectronic applications.[5-6] When synthesized in a colloidal form they can be used as inks for the preparation of low-cost, large area thin film devices. With the unique feature of size dependent electronic structure in colloidal semiconductors comes the challenge of synthesizing a homogenous ensemble of QDs where each individual dot is indistinguishable from the other to realize their true potential. Early success in this regard was achieved by Murray, Norris and Bawendi when they developed an organometallic synthetic route to colloidal CdSe NCs which showed sharp size dependent absorption features and band-edge emission.[7] The synthesis was based on the pyrolysis of organometallic Cd and Se precursors in a coordinating solvent (tri-octyl phosphine) via a hot injection method which temporally separated the nucleation and growth events leading to size controlled colloidal

Quantum dots. This report started the field of solution processed colloidal quantum dots which has seen tremendous progress in the last two and a half decades and is now a commercial commodity.[8]

Several important milestones have been achieved in this journey towards commercialization of quantum dots. The community has learned to synthesize quantum dots of various compositions with precise control over their shape and sizes.[9-11] Colloidal quantum dots of various families of semiconductors can be synthesized which cover a wide range of the electromagnetic spectrum. Table 1.1 gives a few examples of colloidal quantum dots belonging to the various families of semiconductors. Significant progress has been made in the understanding of their surface chemistry which plays a critical role in the emission efficiency of quantum dots.[12-13] Epitaxial growth of precisely engineered wide band gap multi-shells has proven to be the most efficient strategy to confine the carriers in the core leading almost unity emission quantum yields.[14-15] The most recent examples of innovation in the chemistry of colloidal semiconductors include the advent of quasi two dimensional nanoplatelets or "colloidal quantum wells" which show significantly narrow emission linewidths or the synthesis of colloidal nanocrystals of halide perovskites ($CsPbX_3$) with high emission efficiencies. [16-17]

Even though significant progress has been made in our efforts to understand and develop the chemistry of colloidal quantum dots, several challenges remain to be solved before quantum dots can fulfill their true potential as the building blocks of solution processed optoelectronic devices. While Quantum dots of II-VI semiconductors have made their way into consumer goods as chromophores in display technology, they are still far away from being efficient electroluminescent materials. Similarly, while arrays of electronically coupled quantum dots have shown impressive carrier mobilities and charge transport properties in lab scale thin film devices, they are far from being employed as electronic components of an integrated circuit.[18]

Family	Examples	Wavelength Range
II-VI	ZnS,ZnSe,CdS CdSe,CdTe HgS,HgSe,HgTe	UV-Blue Visible Near IR-Mid IR
III-V	GaP, GaN InP, GaAs InAs, InSb	UV-Blue Visible Near IR- Mid IR
IV-VI	PbS,PbSe,PbTe	Near IR- Mid IR
VI	Si, Ge	Near- IR
II-V	Cd_3P_2, Cd_3As_2	Near IR- Mid IR
I-III-VI	$CuInS_2$,$CuInSe_2$ $Ag(In,Ga)(S/Se)_2$, $Cu(In,Ga)S/Se_2$	visible-Near IR Visible

Table 1.1 Classification of quantum dots into their family of compounds and accessible wavelength ranges.

From a synthetic stand point, the quality of nanomaterials achievable via colloidal routes varies widely for different families of semiconductors. While the synthesis of colloidal quantum dots of ionic semiconductors has now been almost perfected, the more covalent semiconductors such as those belonging to the III-V groups are still difficult to be synthesized in as high quality as their III-V counterparts. This difference in the maturity of the two classes of quantum dot is not due to lack of effort by researchers, but due to the inherent difficulty in the synthetic control of III-V quantum dots at the nanoscale. In this dissertation, I present the details of the novel approaches developed in the Talapin lab to advance the synthesis of colloidal III-V quantum dots. However, before we delve into the details of colloidal synthesis of III-V quantum dots, it is important to appreciate why they are a desirable class of compounds.

Similar to the II-VI family of semiconductors, III-V compounds form a self-sufficient family of mostly direct gap semiconductors that cover a wide range of electromagnetic spectrum (from GaN (E_g=3.2eV) in the blue to InSb in the mid-IR (E_g = 0.17eV)) and lattice constants (a_{GaP}

= 5.45Å to a_{InSb} = 6.48Å) which makes possible the synthesis of precisely engineered core-shell nanostructures covering essentially the same range as II-VI semiconductors.[19] In contrast to II-VI semiconductors, III-V semiconductors possess much superior electronic properties. They normally have much higher electronic mobilities: GaAs (9200 cm2/V.s) is six times, and InSb (78,000 cm2/V.s) is fifty times higher than silicon, leading to much faster operation speed for the transistors and lower thermal noise.[19] Moreover, owing to the absence of heavy metals, III-V compounds also present less toxic alternatives to their II-VI and IV-VI counterparts.[20] With the recently imposed restrictions on the use of Cd in consumer products, it is imperative to develop non-toxic QD alternatives to replace CdSe in display applications and InP has proven to be the front runner in this regard.

The covalency of III-V semiconductors not only complicates their synthesis but also has significant consequences on its optical properties.[21] The electronic structure of semiconductors is strongly dependent on their dielectric constant. One of the direct consequences of their covalence is that their bohr exciton radii are typically larger than those of the II-VI family which allows quantum confinement effects to be seen in a larger ranges of sizes ($a=a_o(\varepsilon/\mu)$, where a_o is the bohr radius, ε is the dielectric constant and μ is the reduced effective mass). Due to the smaller effective masses of electrons in III-V semiconductors, they also are more sensitive to changes in size. As an example, the change in band gaps with sizes for CdSe and InP QDs are shown for comparison in Figure 1.1. As one can clearly see InP QDs are more sensitive to size and therefore a tighter control of size distribution is required for them to yield similar linewidths to CdSe QDs. Covalent III-V compounds are also characterized by smaller band curvatures which may allow for larger crosstalk between electrons in different valleys. This becomes especially important for semiconductors where the γ–valley is close in energy to L-valley. A case in point can be Quantum

confined GaAs QDs. Due to the difference in the effective masses in the two valleys, the strength of quantum confinement is weaker in the L-valley. This allows for a crossover of L-valley as the lowest energy valley upon decreasing the size of GaAs QDs below 3.4 nm as predicted by Zunger et.al.[22] This is schematically illustrated in Figure 1.2.

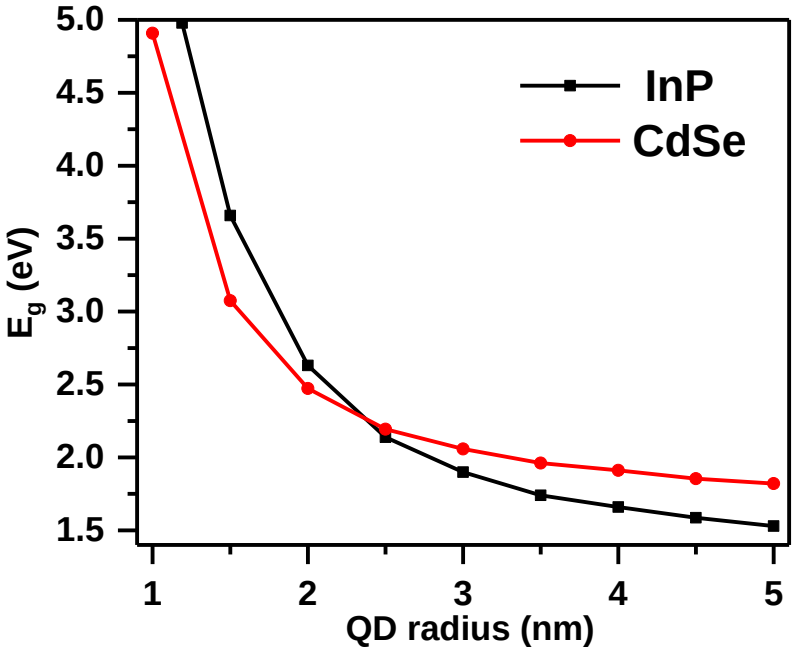

Figure 1.1. Dependence of the band gap on the nanocrystal diameter for InP and CdSe, calculated using the effective mass approximation (used parameters: E_g = 1.35/1.74 eV; ε_r = 12.4/9.5; r_{Bohr} = 9.6/4.6 nm for InP/CdSe)[23]

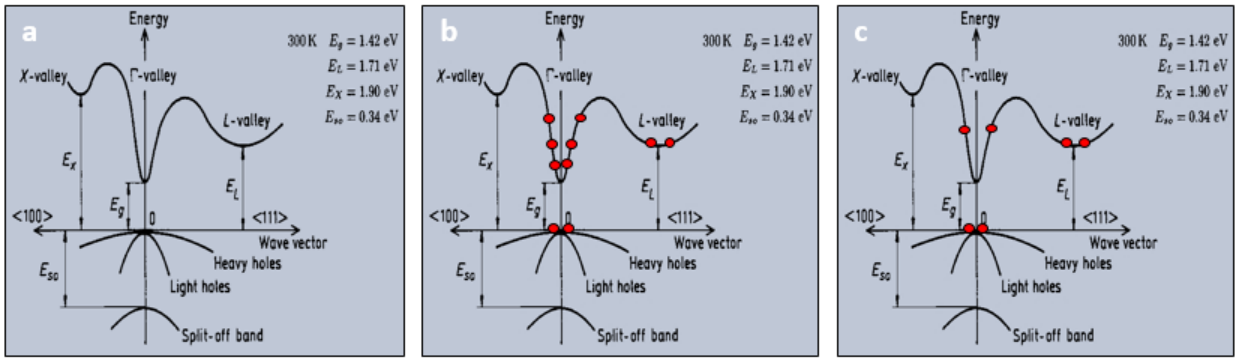

Figure 1.2 Changes in the electronic structure of GaAs upon quantum confinement (a) bulk GaAs (b) Quantum confined GaAs QDs (direct gap) (c) Quantum confined GaAs QDs (direct gap). Red circles represent the quantized discrete energy levels in a quantum confined semiconductor. The crossover from (b) to (c) is predicted to happen at ~3.4 nm by Zunger et.al.

The covalence of III-V semiconductors also brings challenges to the colloidal synthesis of monodisperse III-V QDs. One of the foremost challenges is the limited choice of pnictide (group V) precursors. Typically AsH_3 or PH_3 are used as pnictide precursors in the solid state synthesis of III-V compounds. Both these precursors are not only extremely toxic and pyrophoric, they also exist in gaseous phase at room temperature and are highly unstable. For the colloidal synthesis, pnictide precursors are typically heavily complexed molecules that can stabilized the pnictide ions in their (-III) oxidation states. One of the most widely explored pnictide precursors in the synthesis of III-V nanocrystals is tris-trimethylsilylpnictide ($(TMS)_3P$/$(TMS)_3As$).[24] The Wells dehalosilylation reaction,[24] shown below, yields both InP and InAs QDs in the presence of coordinating ligands like TOP and TOPO. [25-26]

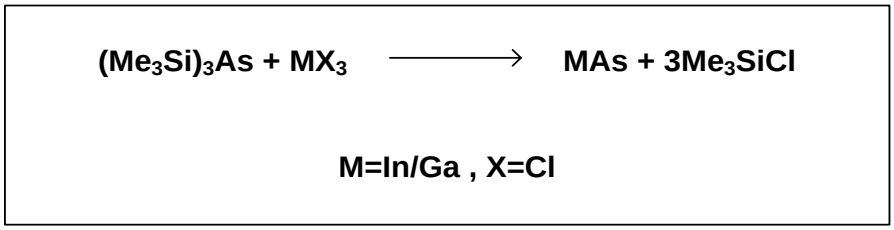

The issue, however, with this reaction is the lack of kinetic control over nucleation and growth events. Several modifications of this reaction have been well studied and the reaction is shown to grow through kinetically persistent intermediates which make the temporal separation of nucleation and growth events difficult.[27] According to the well-known LaMer model of nucleation and growth[28] (See Figure 1.3) it is however important to separate the nucleation and growth events temporally to obtain monodisperse QD populations. Several attempts have been made in this direction by tuning the reactivity of the pnictide precursors by changing the silyl groups to germyl groups or by increasing the steric bulk of the leaving alkyl group, however they have not been as successful as desired.[29-30] In the case of InP QDs, magic sized clusters that persist through out the reaction time interval have been proposed to be a deterrent to monodisperse QD populations.[31-32]

Similar assignments have also been made for InAs QDs.[33] Apart from these problems, the toxicity and difficulty of preparation of these heavily complexed group V precursors have kept the exploration of III-V QD synthesis from more widespread exploration.

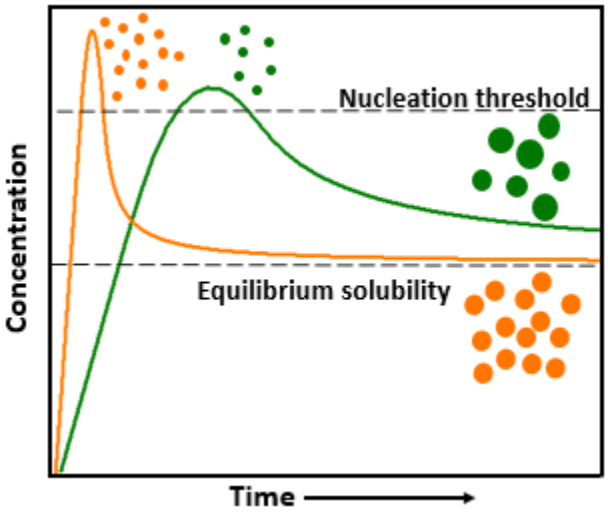

Figure 1.3 LaMer model for the synthesis of colloidal nanocrystals. The scheme represents the effect of precursor conversion kinetics on the size distribution of final NC population. The orange curve represents the case where fast precursor conversion leads to a shorter nucleation event whereas the green curve shows the case where the nucleation stage persists for longer due to slow conversion kinetics leading to a broad size distributions.

For these reasons, the community has constantly looked for alternative pnictide precursors for the synthesis of III-V QDs. In the recent years, the use of aminophosphines for the synthesis of InP QDs has reignited the community's interest in aminopnictides as a suitable alternative pnictide precursor for the synthesis of III-V QDs.[34] Chapter two of this dissertation details the use of aminoarsine as suitable precursors for the synthesis of InAs QDs mediated via a reducing agent mediated approach.[35] In Chapter three of this dissertation, I discuss the role of reducing agents (hydrides) in the kinetics of precursor conversion in the reaction between $InCl_3$ And dimethylaminoarsine ($As(NMe_2)_3$). It is demonstrated that the reducing ability of the hydride indeed has an impact on the final size distribution of the product and an optimal reducing agent,

namely an amine-alane complex, can lead to effective separation between nucleation and growth events, thereby leading to monodisperse populations of InAs QDs.[36] It is our belief that this concept of using appropriate reducing agents for aminopnictide precursors can be extended to the synthesis of other III-V compounds as well and can advance the exploration of colloidal III-V QDs in a variety of applications.

The next issue with the synthetic arsenal of colloidal III-V Quantum dots is the generality or lack there-of, of the dehalosilylation reaction in yielding other important QDs such as GaAs. This reaction was first attempted in 1990 by the Alivisatos group to produce GaAs QDs, however, it led to an amorphous product which had to be annealed at 450°C to yield crystalline GaAs.[37] There were several other attempts in the next two decades to synthesize crystalline GaAs QDs but none of them showed consistent features in the absorption spectrum which would be expected for a quantum confined semiconductor.[38] Indirect approaches such as cation exchange on the more ionic II-V Cd_3As_2 NCs were also explored to synthesize GaAs QDs but they also didn't lead to well-defined optical absorption features.[39] There have been two primary lines of thought to explain this anomaly: 1) the polydispersity of QD ensembles produced via all the approaches 2) indirect transitions dominate in quantum confined GaAs QDs which lead to featureless absorption spectra (See Figure). However, in the absence of high quality GaAs QDs with relatively monodisperse populations, it is difficult to investigate the real reasons behind this apparent anomaly. The lack of crystallinity or the presence of metal impurity have been persistent features in most of the syntheses reported for GaAs QDs. The increased covalence of GaAs as compared to Indium pnictides can be responsible for the formation of structural defects in these semiconductors when synthesized at low temperatures. Literature on bulk GaAs thin films grown through MBE approaches are replete with examples of impurity defects in GaAs synthesized at lower

temperatures (See Figure 1.4).[40] The lower diffusivity in covalent compounds allows easier freezing of core defects in III-V semiconductors as compared to the ionic II-VI semiconductors.[41] In chapter four, I present a novel approach to the synthesis of colloidal GaAs with high crystallinity and monodisperse populations via a reducing agent mediated approach.[42] This synthetic advance enables to to characterize the structural and optical properties of colloidal GaAs NCs in depth and point out the role of structural defects in their anomalous optical properties with reasonable certainity.

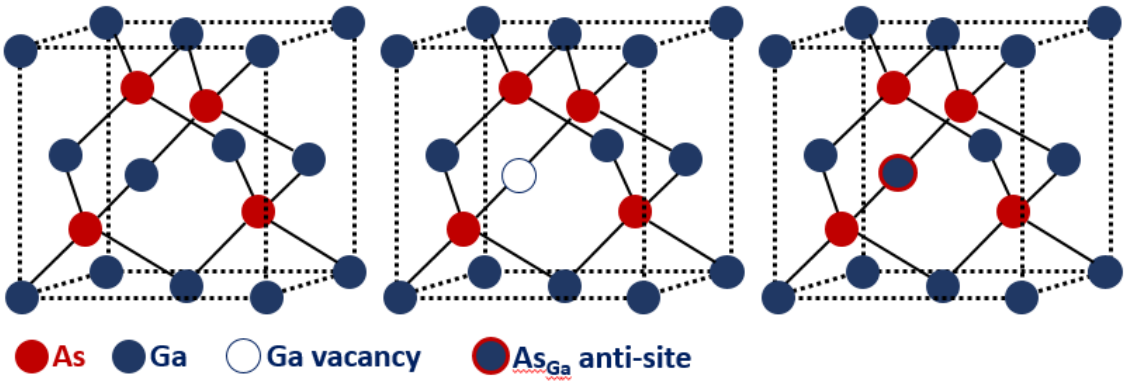

Figure 1.4 Unit cell of cubic zinc blende GaAs and representation of two kinds of structural defects (1) Vacancy defects and (2) Antisite defects.

The low diffusivity of ions is also responsible for the absence of ternary alloy QDs of III-V semiconductors. Direct synthesis of ternary alloys such as $In_{1-x}Ga_xP$ is made difficult due to the rigidity of their lattice which requires higher temperatures to reorganize. This can be contrasted to the success of ternary II-VI systems which are widely used for band gap engineering of core-shell heterostructures.[43-44] Band-gap engineering through alloying in III-V QDs has been rarely explored and the limiting factor in this regard remains the high temperature requirement for the synthesis of these covalent systems.

For reasons detailed above, it is imperative that colloidal chemistry be accessible at temperature beyond its traditional maximum of ~350°C. The ability to manipulate nanostructures in a colloidal form at temperatures beyond 400°C is not only desirable for III-V semiconductors but will also open the avenues of other highly covalent systems such as carbides or nitrides to colloidal chemists. This is the subject of chapter 4 in this dissertation, where I introduce molten inorganic salts as solvents for processing of colloidal nanoparticles and present a deeper understanding of the nature of colloidal stability in these solvents. The ability to prepare stable colloids of inorganic nanoparticles in molten inorganic salts was recently demonstrated by Zhang *et.al*.[45]

In Chapter six and seven, I demonstrate the application of molten salts as high temperature solvents for the synthesis and manipulation of III-V QDs. Chapter Six details the annealing of structural defects in GaAs QDs in molten salts at 500°C which leads to appearance of excitonic features in their absorption spectrum, expected for quantum confined direct gap semiconductors. In Chapter seven, I demonstrate that facile cation exchange reactions can be performed on pre-synthesized QDs in molten salts at high temperatures which lead to ternary $In_{1-x}Ga_xP$ and $In_{1-x}Ga_xAs$ QDs. The optical properties of these compounds are discussed in detail. The ability to synthesize high quality alloy QDs in molten salts opens up the possibility of band gap engineering and heterostructure growth of all III-V QDs on par with that seen in II-VI systems. From the perspective of shell growth, even though the tetrahedral nature of bonding in both cases allows the formation of II-VI shells over III-V cores, the imbalance in electron count at the interface still makes III-V materials a more desirable choice for shell growth. We believe that the ability to handle III-V QDs at high temperature in a colloidal form can enable further work in these directions.

References:

1. Efros, A. L.; Efros, A. L., Interband absorption of light in a semiconductor sphere. *Soviet Physics Semiconductors-Ussr* **1982,** *16* (7), 772-775.
2. Brus, L. E., A simple model for the ionization potential, electron affinity, and aqueous redox potentials of small semiconductor crystallites. *The Journal of Chemical Physics* **1983,** *79* (11), 5566-5571.
3. Alivisatos, A. P., Semiconductor Clusters, Nanocrystals, and Quantum Dots. *Science* **1996,** *271* (5251), 933-937.
4. Brus, L., Electronic wave functions in semiconductor clusters: experiment and theory. *The Journal of Physical Chemistry* **1986,** *90* (12), 2555-2560.
5. Talapin, D. V.; Lee, J.-S.; Kovalenko, M. V.; Shevchenko, E. V., Prospects of Colloidal Nanocrystals for Electronic and Optoelectronic Applications. *Chemical Reviews* **2010,** *110* (1), 389-458.
6. Kovalenko, M. V.; Manna, L.; Cabot, A.; Hens, Z.; Talapin, D. V.; Kagan, C. R.; Klimov, V. I.; Rogach, A. L.; Reiss, P.; Milliron, D. J.; Guyot-Sionnnest, P.; Konstantatos, G.; Parak, W. J.; Hyeon, T.; Korgel, B. A.; Murray, C. B.; Heiss, W., Prospects of Nanoscience with Nanocrystals. *ACS Nano* **2015,** *9* (2), 1012-1057.
7. Murray, C. B.; Norris, D. J.; Bawendi, M. G., Synthesis and characterization of nearly monodisperse CdE (E = sulfur, selenium, tellurium) semiconductor nanocrystallites. *Journal of the American Chemical Society* **1993,** *115* (19), 8706-8715.
8. Owen, J.; Brus, L., Chemical Synthesis and Luminescence Applications of Colloidal Semiconductor Quantum Dots. *Journal of the American Chemical Society* **2017,** *139* (32), 10939-10943.
9. Talapin, D. V.; Nelson, J. H.; Shevchenko, E. V.; Aloni, S.; Sadtler, B.; Alivisatos, A. P., Seeded Growth of Highly Luminescent CdSe/CdS Nanoheterostructures with Rod and Tetrapod Morphologies. *Nano Letters* **2007,** *7* (10), 2951-2959.
10. Manna, L.; Scher, E. C.; Alivisatos, A. P., Synthesis of Soluble and Processable Rod-, Arrow-, Teardrop-, and Tetrapod-Shaped CdSe Nanocrystals. *Journal of the American Chemical Society* **2000,** *122* (51), 12700-12706.
11. Zhou, J.; Pu, C.; Jiao, T.; Hou, X.; Peng, X., A Two-Step Synthetic Strategy toward Monodisperse Colloidal CdSe and CdSe/CdS Core/Shell Nanocrystals. *Journal of the American Chemical Society* **2016,** *138* (20), 6475-6483.
12. Anderson, N. C.; Hendricks, M. P.; Choi, J. J.; Owen, J. S., Ligand Exchange and the Stoichiometry of Metal Chalcogenide Nanocrystals: Spectroscopic Observation of Facile Metal-Carboxylate Displacement and Binding. *Journal of the American Chemical Society* **2013,** *135* (49), 18536-18548.
13. Boles, M. A.; Ling, D.; Hyeon, T.; Talapin, D. V., The surface science of nanocrystals. *Nature Materials* **2016,** *15*, 141.
14. Hines, M. A.; Guyot-Sionnest, P., Synthesis and Characterization of Strongly Luminescing ZnS-Capped CdSe Nanocrystals. *The Journal of Physical Chemistry* **1996,** *100* (2), 468-471.
15. Coropceanu, I.; Rossinelli, A.; Caram, J. R.; Freyria, F. S.; Bawendi, M. G., Slow-Injection Growth of Seeded CdSe/CdS Nanorods with Unity Fluorescence Quantum Yield and Complete Shell to Core Energy Transfer. *ACS Nano* **2016,** *10* (3), 3295-3301.

16. Ithurria, S.; Dubertret, B., Quasi 2D Colloidal CdSe Platelets with Thicknesses Controlled at the Atomic Level. *Journal of the American Chemical Society* **2008,** *130* (49), 16504-16505.
17. Protesescu, L.; Yakunin, S.; Bodnarchuk, M. I.; Krieg, F.; Caputo, R.; Hendon, C. H.; Yang, R. X.; Walsh, A.; Kovalenko, M. V., Nanocrystals of Cesium Lead Halide Perovskites (CsPbX3, X = Cl, Br, and I): Novel Optoelectronic Materials Showing Bright Emission with Wide Color Gamut. *Nano Letters* **2015,** *15* (6), 3692-3696.
18. Kagan, C. R.; Lifshitz, E.; Sargent, E. H.; Talapin, D. V., Building devices from colloidal quantum dots. *Science* **2016,** *353* (6302).
19. Adachi, S., *Physical properties of III-V semiconductor compounds*. John Wiley & Sons: 1992.
20. Lin, G.; Ouyang, Q.; Hu, R.; Ding, Z.; Tian, J.; Yin, F.; Xu, G.; Chen, Q.; Wang, X.; Yong, K.-T., In vivo toxicity assessment of non-cadmium quantum dots in BALB/c mice. *Nanomedicine: Nanotechnology, Biology and Medicine* **2015,** *11* (2), 341-350.
21. R. Heath, J., Covalency in semiconductor quantum dots. *Chemical Society Reviews* **1998,** *27* (1), 65-71.
22. Luo, J.-W.; Franceschetti, A.; Zunger, A., Quantum-size-induced electronic transitions in quantum dots: Indirect band-gap GaAs. *Physical Review B* **2008,** *78* (3), 035306.
23. Brus, L. E., Electron–electron and electron-hole interactions in small semiconductor crystallites: The size dependence of the lowest excited electronic state. *The Journal of Chemical Physics* **1984,** *80* (9), 4403-4409.
24. Wells, R. L.; Pitt, C. G.; McPhail, A. T.; Purdy, A. P.; Shafieezad, S.; Hallock, R. B., The use of tris(trimethylsilyl)arsine to prepare gallium arsenide and indium arsenide. *Chemistry of Materials* **1989,** *1* (1), 4-6.
25. Micic, O. I.; Curtis, C. J.; Jones, K. M.; Sprague, J. R.; Nozik, A. J., Synthesis and Characterization of InP Quantum Dots. *The Journal of Physical Chemistry* **1994,** *98* (19), 4966-4969.
26. Guzelian, A. A.; Banin, U.; Kadavanich, A. V.; Peng, X.; Alivisatos, A. P., Colloidal chemical synthesis and characterization of InAs nanocrystal quantum dots. *Applied Physics Letters* **1996,** *69* (10), 1432-1434.
27. Cossairt, B. M., Shining Light on Indium Phosphide Quantum Dots: Understanding the Interplay among Precursor Conversion, Nucleation, and Growth. *Chemistry of Materials* **2016,** *28* (20), 7181-7189.
28. LaMer, V. K.; Dinegar, R. H., Theory, Production and Mechanism of Formation of Monodispersed Hydrosols. *Journal of the American Chemical Society* **1950,** *72* (11), 4847-4854.
29. Daniel, F.; K., H. D.; Lisi, X.; F., J. K.; G., B. M., The Unexpected Influence of Precursor Conversion Rate in the Synthesis of III–V Quantum Dots. *Angewandte Chemie International Edition* **2015,** *54* (48), 14299-14303.
30. Harris, D. K.; Bawendi, M. G., Improved Precursor Chemistry for the Synthesis of III–V Quantum Dots. *Journal of the American Chemical Society* **2012,** *134* (50), 20211-20213.
31. Xie, L.; Shen, Y.; Franke, D.; Sebastián, V.; Bawendi, M. G.; Jensen, K. F., Characterization of Indium Phosphide Quantum Dot Growth Intermediates Using MALDI-TOF Mass Spectrometry. *Journal of the American Chemical Society* **2016,** *138* (41), 13469-13472.
32. Gary, D. C.; Terban, M. W.; Billinge, S. J. L.; Cossairt, B. M., Two-Step Nucleation and Growth of InP Quantum Dots via Magic-Sized Cluster Intermediates. *Chemistry of Materials* **2015,** *27* (4), 1432-1441.

33. Tamang, S.; Lee, S.; Choi, H.; Jeong, S., Tuning Size and Size Distribution of Colloidal InAs Nanocrystals via Continuous Supply of Prenucleation Clusters on Nanocrystal Seeds. *Chemistry of Materials* **2016,** *28* (22), 8119-8122.
34. Tessier, M. D.; De Nolf, K.; Dupont, D.; Sinnaeve, D.; De Roo, J.; Hens, Z., Aminophosphines: A Double Role in the Synthesis of Colloidal Indium Phosphide Quantum Dots. *Journal of the American Chemical Society* **2016,** *138* (18), 5923-5929.
35. Srivastava, V.; Janke, E. M.; Diroll, B. T.; Schaller, R. D.; Talapin, D. V., Facile, Economic and Size-Tunable Synthesis of Metal Arsenide Nanocrystals. *Chemistry of Materials* **2016,** *28* (18), 6797-6802.
36. Srivastava, V.; Dunietz, E.; Kamysbayev, V.; Anderson, J. S.; Talapin, D. V., Monodisperse InAs Quantum Dots from Aminoarsine Precursors: Understanding the Role of Reducing Agent. *Chemistry of Materials* **2018,** *30* (11), 3623-3627.
37. Olshavsky, M. A.; Goldstein, A. N.; Alivisatos, A. P., Organometallic synthesis of gallium-arsenide crystallites, exhibiting quantum confinement. *Journal of the American Chemical Society* **1990,** *112* (25), 9438-9439.
38. Lauth, J.; Strupeit, T.; Kornowski, A.; Weller, H., A Transmetalation Route for Colloidal GaAs Nanocrystals and Additional III–V Semiconductor Materials. *Chemistry of Materials* **2013,** *25* (8), 1377-1383.
39. Beberwyck, B. J.; Alivisatos, A. P., Ion Exchange Synthesis of III–V Nanocrystals. *Journal of the American Chemical Society* **2012,** *134* (49), 19977-19980.
40. Look, D. C., Molecular beam epitaxial GaAs grown at low temperatures. *Thin solid films* **1993,** *231* (1-2), 61-73.
41. Shaw, D., *Atomic diffusion in semiconductors*. Springer Science & Business Media: 2012.
42. Srivastava, V.; Liu, W.; Janke, E. M.; Kamysbayev, V.; Filatov, A. S.; Sun, C.-J.; Lee, B.; Rajh, T.; Schaller, R. D.; Talapin, D. V., Understanding and Curing Structural Defects in Colloidal GaAs Nanocrystals. *Nano Letters* **2017,** *17* (3), 2094-2101.
43. Bailey, R. E.; Nie, S., Alloyed semiconductor quantum dots: tuning the optical properties without changing the particle size. *Journal of the American Chemical Society* **2003,** *125* (23), 7100-7106.
44. Mahler, B.; Nadal, B.; Bouet, C.; Patriarche, G.; Dubertret, B., Core/shell colloidal semiconductor nanoplatelets. *Journal of the American Chemical Society* **2012,** *134* (45), 18591-18598.
45. Zhang, H.; Dasbiswas, K.; Ludwig, N. B.; Han, G.; Lee, B.; Vaikuntanathan, S.; Talapin, D. V., Stable colloids in molten inorganic salts. *Nature* **2017,** *542* (7641), 328.

Chapter 2.

Aminoarsines as arsenic precursors for the synthesis of metal arsenide nanocrystals

2.1 Introduction

Colloidal NCs of semiconductor, metal or dielectric compounds are a compelling class of building blocks for low-cost and large-area devices.[1-2] In particular, the subset of nanomaterials which absorb and emit in the IR wavelength (700nm to 1mm) may find use in applications such as telecommunication[3,4], in vivo biological imaging[5], IR photodetectors[6], night vision[7], machine vision[8] and photovoltaics[9]. While current investigations of IR-active semiconductor nanomaterials have primarily focused on II-VI and IV-VI compounds, III-V semiconductors such as InAs [10],[11],[12] and InSb[13-14] have garnered attention as a less-toxic potential alternative to lead[15] and mercury[16] chalcogenides.

Whereas the colloidal synthesis of II-VI and IV-VI materials has been well developed, the same is not true for III-V materials. The covalent character of III-V semiconductors makes it difficult to separate the nucleation and growth stages.[17],[18] Established models for the growth of II-VI NCs do not apply here and control of size distribution is challenging.[19] In particular, the only well-established way to synthesize InAs NCs is the dehalosilylation reaction developed by Wells more than two decades ago.[20] This reaction requires tris-trimethylsilylarsine (TMS_3As) as the arsenic precursor which is air, moisture and light sensitive, highly pyrophoric and not commercially available. The difficult synthesis of this compound increases cost and reduces practical utility of arsenide quantum dots. Other methods have been proposed for the synthesis of InAs, but they either use very toxic AsH_3 gas as the As precursor or the quality of the resultant nanocrystals is not comparable to that from the dehalosilylation route.[21,22-23] Recently

aminophosphines have been used as phosphorus precursors for the synthesis of InP nanocrystals providing the first successful example of InP NC synthesis from aminopnictide precursors.[24-25] Additionally, amidoantimony precursors have been used for the synthesis of InSb NCs as well using a superhydride mediated approach.[13]

Synthesis of colloidal nanomaterials of other important metal arsenide compounds, such as Cd_3As_2, has also been limited by the lack of convenient arsenic precursors. Cd_3As_2 is a compound semiconductor of the II-V family with a unique electronic structure. Until recently it was believed to have an inverted band structure with a band gap of -0.19 eV, however, recent reports have suggested it to be a Dirac semimetal , a 3-D analog of graphene.[26],[27] With a large Bohr exciton radius of 47 nm, strong quantum confinement effects are expected in this material, opening its band gap up in the IR.[28] Colloidal II-V nanocrystals are still under-explored and their synthesis is still in the stage of development.[29] Bawendi group recently reported the synthesis of size-tunable Cd_3As_2 NCs with well resolved excitonic features using a continuous injection of TMS_3As for several hours to grow Cd_3As_2 of sizes up to 5 nm.[28] Synthesis of Cd_3As_2 from AsH_3 gas has also been reported[30].

In this chapter I present the case for tris-dimethylaminoarsine ($As(NMe_2)_3$) as a compelling arsenic precursor for the synthesis of size and shape uniform InAs NCs. $As(NMe_2)_3$ is a commercially available, easy to handle and reasonably inexpensive compound making it a desirable precursor choice. In the subsequent sections I will detail how this precursor can be used to prepare high quality InAs NCs with controlled size distributions. The approach employs a reaction between $InCl_3$ and $As(NMe_2)_3$ using diisobutylaluminum hydride (DIBAL-H) to convert $As(NMe_2)_3$ *in situ* into reactive intermediates $AsH_x(NMe_2)_{3-x}$ where x=1,2,3. NC size can be varied by changing DIBAL-H concentration and growth temperature, with colloidal solutions of InAs

showing size dependent absorption and emission features tunable across wavelengths of 750-1450 nm. This approach works well for the colloidal synthesis of Cd_3As_2 NCs. By circumventing the preparation of notoriously unstable and dangerous arsenic precursors (eg. AsH_3 and $As(SiMe_3)_3$), this work improves the synthetic accessibility of arsenide-based NCs and, by extension, the potential of such NCs for use in infrared(IR) applications such as communications, medical imaging and photodetection.

2.2 DIBAL-H mediated synthesis of InAs Nanocrystals

$As(NMe_2)_3$ does not react with typical In precursors (e.g. $InCl_3$) but we found that $As(NMe_2)_3$ dissolved in oleylamine can be activated by diisobutylaluminum hydride (DIBAL-H) to produce InAs NCs upon reaction with $InCl_3$ at elevated temperatures. We could synthesize InAs NCs by sequentially injecting $As(NMe_2)_3$ and DIBAL-H to a pre-heated solution of $InCl_3$ in oleylamine and continuing the growth for 5-60 minutes. The reaction scheme is presented in Figure 2.1. The DIBAL-H concentration and reaction temperature were chosen based on the target NC size. In a typical synthesis, 0.2 mmol $InCl_3$ and 5mL Oleylamine were loaded in a 100 mL 3-neck flask and dried at 130° C under vaccum for 1 hr. The reaction mixture was then heated to 250°C (290°C for larger InAs NCs). The As stock solution was then quickly injected into the flask followed by the injection of 1.2 mL of 1M DIBAL-H in toluene (this amount was varied between 0.2 mmol to 1.2 mmol to achieve desired NC sizes). Upon DIBAL-H addition, the temperature dropped by ~ 10°C. The growth was carried out for 5-60 min at this temperature to achieve the target NC sizes. The reaction was cooled to room temperature and transferred into a nitrogen glovebox. The reaction mixture was diluted with 10 mL toluene and 15 mL ethanol was added to precipitate the NCs. Addition of excess ethanol led to the precipitation of organic byproducts. The precipitated NCs were re-dispersed in toluene or TCE and centrifuged to separate the insoluble

particles and other byproducts. The soluble portion was washed once again with ethanol and re-dispersed in TCE for all the characterization. Size selective precipitation, if necessary, was carried out in a solvent-non solvent mixture of toluene and ethanol.

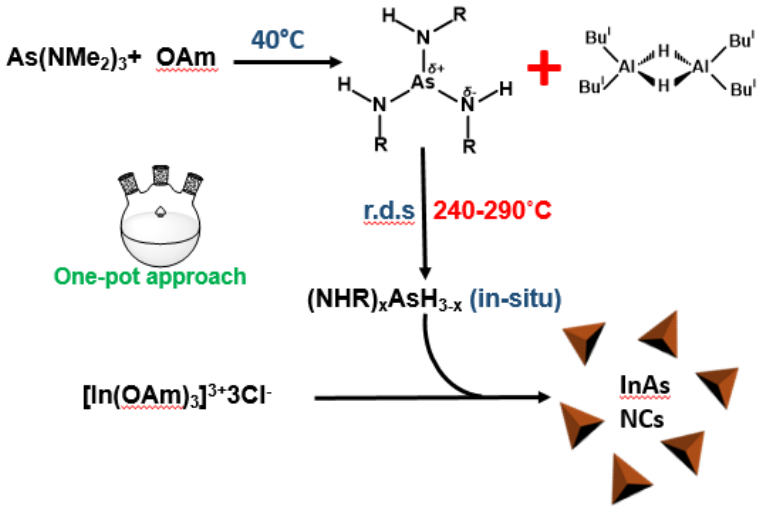

Figure 2.1. Activation of the aminoarsine precursor with alkyaluminum hydride (DIBAL-H). This activated precursor can react with $InCl_3$ in Oleylamine (RNH_2) to form InAs NCs. The amount of aluminum hydride added controls the precursor conversion rate and hence is the nucleation rate determining step (r.d.s).

We believe that DIBAL-H plays a critical role in activating the arsenic precursor which allows the formation of InAs upon reaction with $InCl_3$ at elevated temperatures. Alkylaluminum hydrides (such as DIBAL-H) are known to cleave the As-N bond in alkyl substituted aminoarsines to form As-H bonded intermediates and eventually generate As-As bonded species.[31],[32] For instance, when monoaminodimethylarsine was reacted with dimethylaluminum hydride , dimethylarsine could be isolated as one of the products.[31] Such As-H bonded species should also be produced as intermediates when DIBAL-H is reacted with $As(NMe_2)_3$. We thought these reduced intermediates can be used as nucleophiles to react with $InCl_3$. It was recently found that

in the synthesis of InP, aminophosphines are not merely the phosphorus precursors but also act as a reducing agent by forming P(V) phosphonium salt.[33] The transaminated As $(NHR)_3$ is a much weaker nucleophile than its phosphorus analog and cannot donate its lone-pair on its own. This is proven by the fact that a reaction between $As(NMe_2)_3$ and $InCl_3$ in oleylamine at temperatures as high as 300°C does not yield InAs NCs (Figure 2.2). However, upon DIBAL-H addition, the aminoarsine transforms into As-H bond containing transient species which can react with $[In(OAm)_3]^{3+}Cl_3^-$ complex at temperatures high enough to form crystalline InAs.

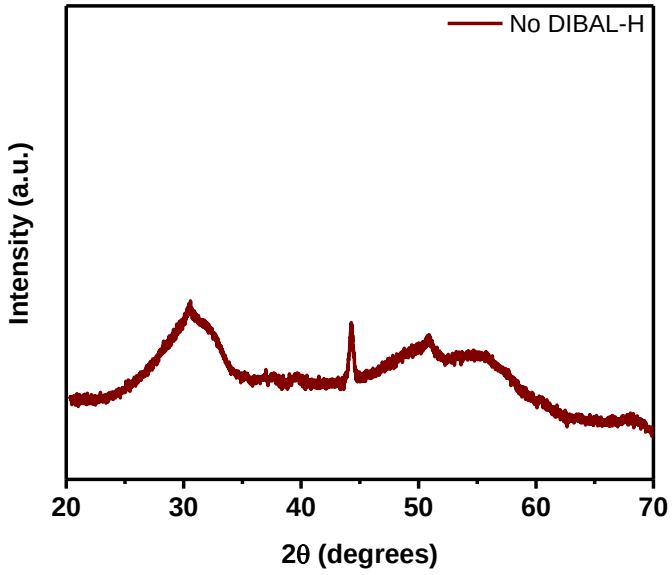

Figure 2.2. Powder XRD pattern of a reaction between $InCl_3$ and As $(NMe_2)_3$ in oleylamine in the absence of DIBAL-H.

2.3 Effect of DIBAL-H concentration and temperature on NC size

DIBAL-H was found to be a convenient lever to tune the size of InAs NCs which further supports our hypothesis about the mechanism of InAs formation. Figure 2.3a shows the effect of DIBAL-H on the size of NCs, as evidenced through the shift in the excitonic features in the absorption spectrum, when all the other reaction parameters were kept constant. The growth in all three cases

was carried out at 240°C for 5 min. It can be seen that higher concentration of DIBAL-H resulted in smaller nanocrystals. It is due to the fact that a larger amount of DIBAL-H leads to a higher concentration of activated As-H bonded species in the solution and hence faster nucleation. Modulation of nucleation rates is a well-known strategy to control final nanocrystal sizes.[34] The growth of the NCs with time was followed by taking aliquots from the reaction pot at regular intervals of time. It was seen that NCs slowly grow with time and there is a slight improvement in the size distribution over time. Higher injection temperatures also led to larger NC sizes. The growth profile of the NCs with time at two different temperatures is shown in Figure 2.4. Similar growth profiles have been observed for InP NCs synthesized from aminophosphines.[24, 35] By combining the effect of temperature, DIBAL-H concentration and growth time, the size of InAs NCs could be continuously tuned between ~2nm and 7nm, such that the lowest excitonic transition varied from 750 nm for the smallest NCs to 1450 nm for the largest InAs NCs as shown in Fig 2.3b. The NC size can be increased further but it requires further optimization to keep narrow size distributions. As synthesized NCs showed band edge emission in the NIR. Figure 2.3c shows an example photoluminescence spectrum for ~ 5 nm InAs NCs centered at 1350 nm with a Stokes shift of ~ 60 meV and a full-width half maximum of 130 meV. The emission intensities varied from sample to sample and were generally comparable to those measured on InAs NCs synthesized with $(TMS)_3As$. The accessible sizes of InAs NCs and conditions for their synthesis are summarized in Table 2.1.

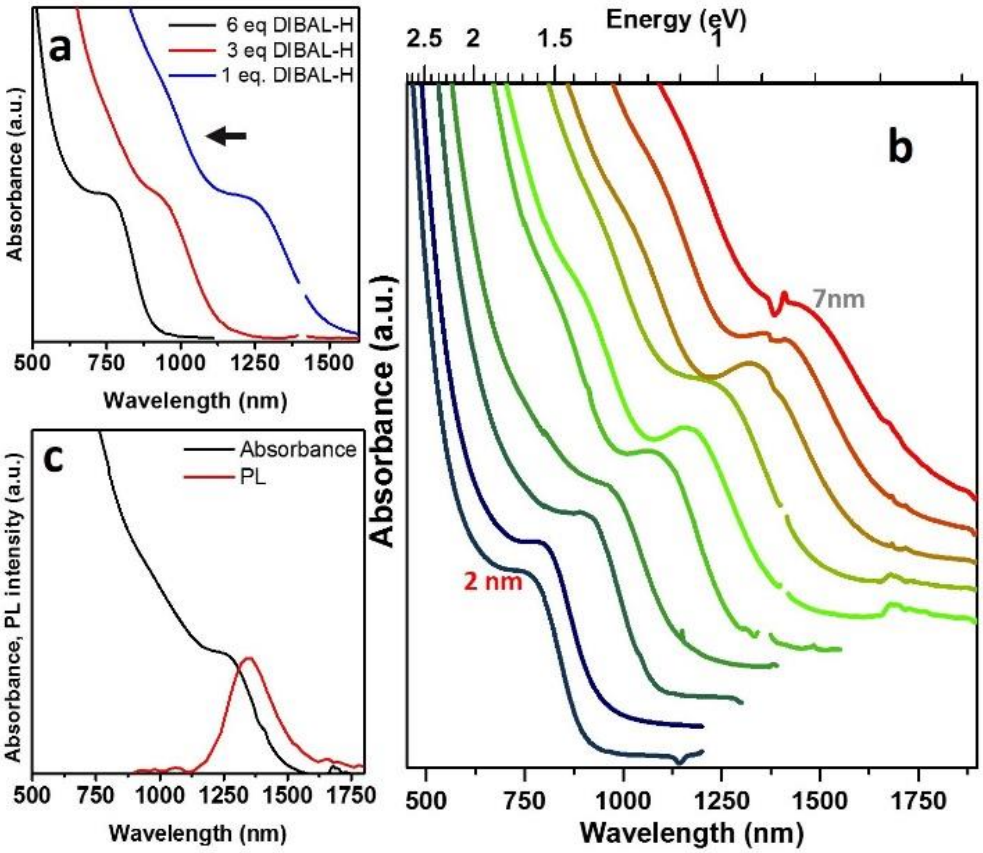

Figure 2.3. Size dependent optical properties of InAs NCs. (a) Absorption spectra of InAs NCs grown at 240°C for 5 min with different concentration of DIBAL-H. (b) Absorption spectra of InAs NCs in the size range of ~2 nm to ~7 nm showing tunability of the synthetic protocol. (c) Representative Absorption and PL spectrum of ~5 nm InAs NCs.

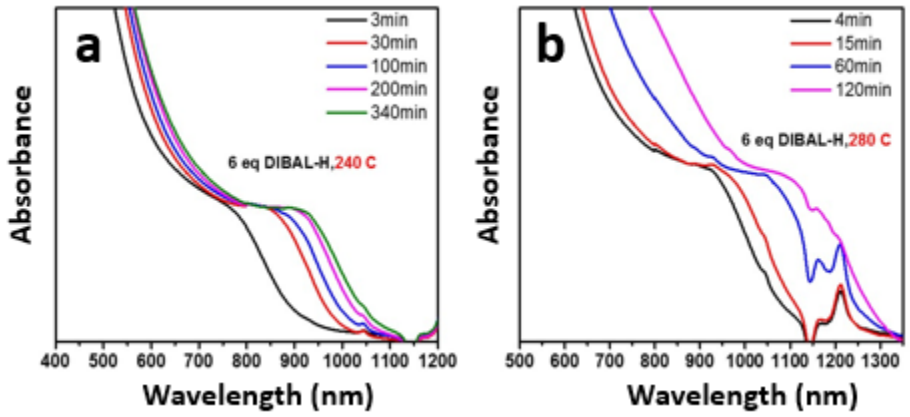

Figure 2.4 Effect of temperature on the growth of InAs NCs (a) Reaction temperature was fixed to 240°C and (b) Reaction temperature was fixed to 280°C. Absorption spectra of aliquots taken at regular time intervals.

$InCl_3$ (mmol)	$As(NMe_2)_3$ (mmol)	DIBAL-H (1M) (mL)	Temp (°C)	Time (mins)	λ_{abs} (nm)
0.2	0.2	1.2	240	3	760
0.2	0.2	1.2	240	5	800
0.2	0.2	1.2	240	50	860
0.2	0.2	1.2	280	15	960
0.2	0.2	1.2,0.6	280,240	60,10	1050
0.2	0.2	0.6,1.2	260,240	15,100	1100
0.4	0.4	1	280	10	1165 (s.f.)
0.2	0.2	0.2	240	5	1250
0.4	0.4	0.4	280	5	1330
0.4	0.4	0.4	280	15	1400(s.f.)
0.4	0.4	0.4	280	15	1450(s.f.)

Table 2.1. Synthetic parameters used to produce InAs NCs. (red color indicates different reaction conditions, s.f.= size fractioned).

2.4 Structural Characterization of InAs NCs

The InAs NCs synthesized using this protocol were tetrahedral in shape as can be seen in TEM image in Figure 2.5. Figures 2.5a and 2.5b show NCs with an average edge length of ~7 nm and ~ 5nm respectively. The high resolution images shown in Figures 2.5c and 2.5d show different facets of InAs tetrahedra. Powder X-ray diffraction pattern of the InAs NCs is consistent with the cubic zinc blende crystal structure of bulk InAs. The NC sizes were calculated using Scherrer equation from the width of diffraction peaks and were in good agreement with the NC size seen in respective TEM images, which speaks for the high crystallinity of the InAs NCs synthesized by this approach (Figure 2.5e). Smaller InAs NCs appeared more spherical. The size distribution of the as synthesized NCs was reasonably good for smaller NCs and well defined excitonic features could be seen from aliquots taken directly from the reaction pot. For larger NCs, size selection helped to achieve monodisperse populations of large InAs NCs. A representative TEM image for ~6 nm InAs NCs along with a size distribution histogram is shown in Figure 2.6.

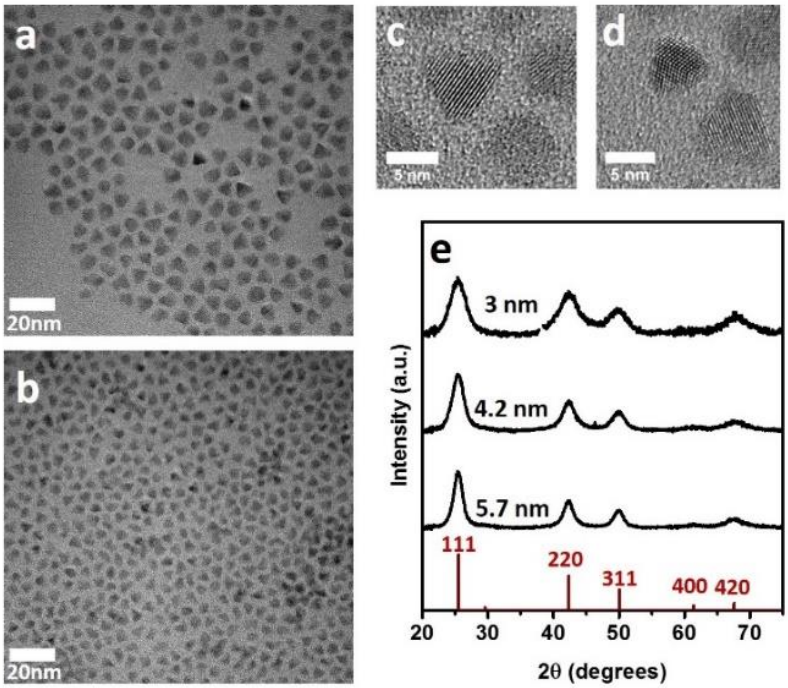

Figure 2.5 Structural characterization of InAs NCs (a,b) TEM images of ~6.5 nm and ~4.5 nm InAs NCs. (c,d) High resolution TEM images of InAs NCs viewed along different zone axes. (e) Powder X-ray diffraction patterns of InAs NCs with various sizes. Sizes above each curve are derived from the Scherrer equation, applied to the fwhm of the (111) reflection. The vertical lines on the bottom are the corresponding positions and intensities of X-ray reflections for bulk InAs.

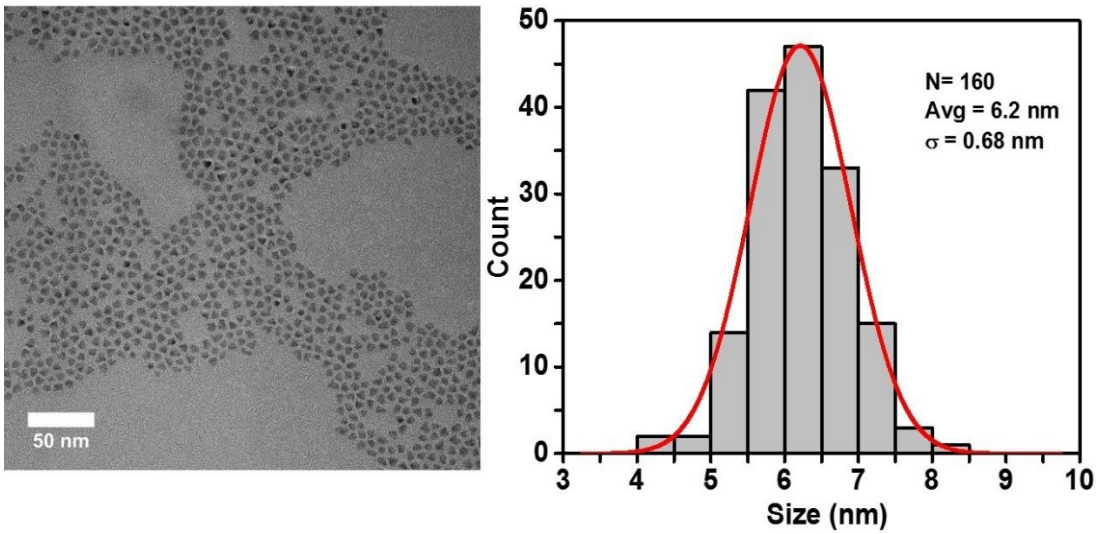

Figure 2.6. A representative TEM image of InAs NCs and the size-distribution histogram.

Spectroscopic characterization of phonons in the confined NCs can be an important tool to assess their crystalline quality. Raman spectroscopy is very sensitive to lattice disorder and defects like vacancies, interstitials and antisites in bulk semiconductors. Figure 2.7a shows the resonance Raman spectra for the same particles that were used for the measurement of XRD patterns shown in Figure 2.5e. All the NCs showed the characteristic transverse optical (TO) and longitudinal optical (LO) phonon modes that correspond well with bulk InAs. The TO and LO phonon modes centered at 218 cm^{-1} and 237 cm^{-1} for the largest InAs NCs broaden as the NC size decreases and cannot be easily distinguished for the smallest NC samples (~2nm). There is a slight shift of the TO phonon to higher wavenumbers and the LO phonon shifts to lower wavenumbers. These spectral features in our NCs matched well with reports in the literature for colloidal InAs NCs.[36] For comparison, we also measured the resonance Raman spectrum of spherical InAs NCs of similar size synthesized from the dehalosilylation reaction. The comparison is shown in Figure 2.7b. The two spectra were very similar to each other in terms of peak position and peak width highlighting the comparable quality of InAs NCs synthesized from both approaches.

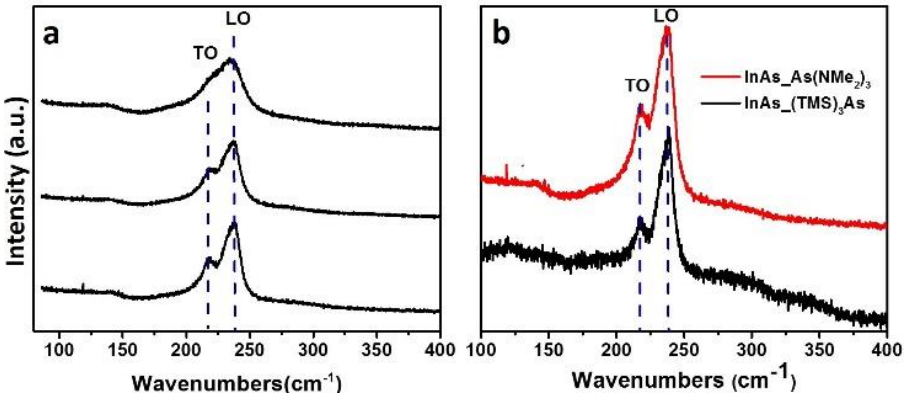

Figure 2.7. Raman Spectra of InAs NCs (a) Raman spectra of InAs NCs with various sizes. The three spectra correspond to the same InAs samples for which XRD patterns are shown in Figure 2e.(b) Comparison of Raman spectra of InAs NCs (~5 nm) prepared by the approach in this report with InAs NCs of similar sizes prepared by dehalosilylation reaction.

2.5 Synthesis of InAs/CdSe core-shell NCs for NIR emission

Growing a thin shell of a wide band gap semiconductor over the bare nanocrystals is a proven strategy to enhance their PL efficiency. It also helps the stability of the core material against oxidation. It is well known that CdSe acts as an efficient shell material for InAs NCs.[10, 37] There is nearly a 0% mismatch between InAs and CdSe. As a proof of concept, a shell of CdSe over small InAs NC cores was grown by using the successive ionic layer adsorption and reaction (SILAR) technique. A 0.04 M Cd precursor solution was prepared by heating CdO (52 mg) and oleic acid (1ML) in ODE (27 mL) at 150°C under nitrogen until a colorless solution is obtained. 0.04mmol Se precursor was prepared by heating 32 mg Selenium powder in 10 mL ODE at 220° C until a clear yellow solution was obtained. For the growth of CdSe shells on ~ 2nm NCs, 3mg InAs NCs were dissolved in 2mL ODE and 1mL oleylamine and heated to 220°C. 80 uL of Cd precursor solution was then injected into the reaction mixture and stirred for 10 mins. Then, 80uL of Se precursor was injected and stirred for 10 mins to complete the growth of first monolayer. For the 2nd monolayer, 100 ul of Cd and Se precursor were respectively added at 10 min intervals to grow the 2nd monolayer. After completion of the shell growth, the reaction was cooled to room temperature and the NCs were precipitated with ethanol. The washed NCs were re-dispersed in TCE for PL measurements. The growth of the shell was monitored by Absorption spectroscopy (Figure 2.8). There was a red shift in the first exciton absorption upon the growth of every monolayer consistent with the partial leakage of the wavefunction into the CdSe shell. The size of the NC also increased consistent with the growth of CdSe shell. We observed a ~100 fold increase in the PL upon growing two monolayers of CdSe over InAs (Figure 2.8). We also observed a significant change in the time-resolved PL decay characteristics of InAs NCs upon CdSe shell growth. There was a significant increase in the lifetime at short timescales and an overall increase in the PL lifetimes (Figure 2.9).

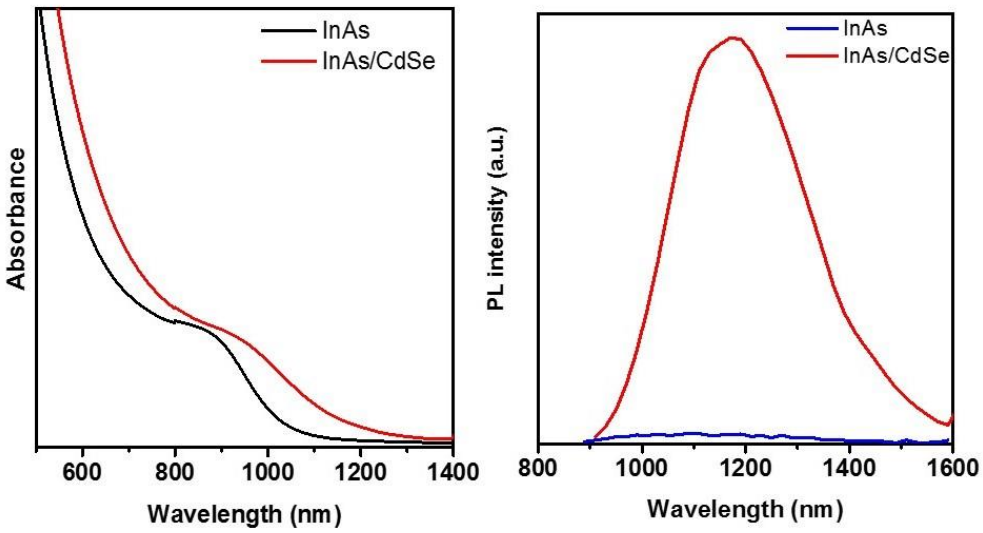

Figure 2.8. Characterization of InAs/CdSe core-shell NCs (Left) Absorption spectra of ~3nm InAs cores and InAs/CdSe core shells. (Right) PL spectra of InAs cores and InAs/CdSe Core shell NCs showing ~100 fold increase in PL efficiency upon shell growth.

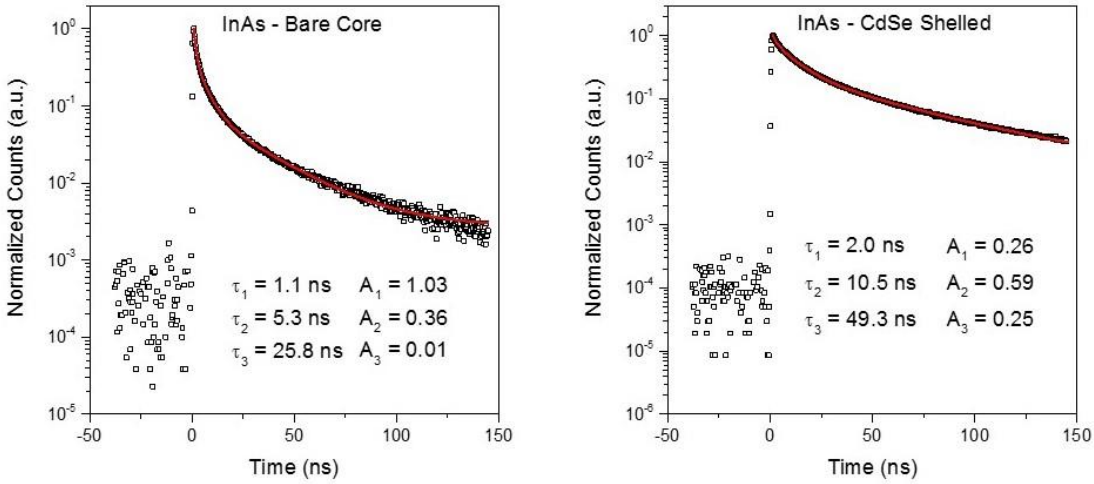

Figure 2.9. Comparison of PL decay times of InAs core vs core shell for which the Absorption and PL are shown in the top panel. There is significant increase in PL decay times due to reduction in trap states upon shell growth.

2.6 Aminoarsines as general Arsenic precursors: Synthesis of Cd_3As_2 NCs

In order to test the versatility and scope of our approach, I attempted the synthesis of Cd_3As_2 NCs using this approach. High quality Cd_3As_2 NCs were synthesized by an approach very similar to that used for the synthesis of InAs NCs described above. In a typical synthesis, 0.3 mmol

$CdCl_2$ and 5mL oleylamine were loaded in a 100 mL 3-neck flask and dried at 130° C under vacuum for 1 hr. The reaction mixture was then heated to 140°C (or 160° C/180° C for size variation). The As stock solution was then quickly injected into the flask followed by the injection of 0.6 mL of 1M DIBAL-H in toluene. Upon DIBAL-H addition, the temperature dropped by ~ 10°C. The growth was carried out for 5 min at this temperature to achieve the target NC sizes. Washing procedure was similar to that described for InAs NCs. Size selective precipitation (based on the difference in solubility between NCs of different size) was necessary here to obtain monodisperse Cd_3As_2 NCs. TEM image of 4.5 nm Cd_3As_2 NCs is shown in Figure 2.10a. The particles were uniform and spherical in shape. The PXRD pattern shown in Figure 2.10b matched well the tetragonal phase of Cd_3As_2. NCs prepared by this approach show well resolved excitonic features and the position of the first excitonic maxima is in good agreement with that reported in reference 35. The absorption and PL spectra of ~ 6nm Cd_3As_2 NCs are shown in figure 2.10c.

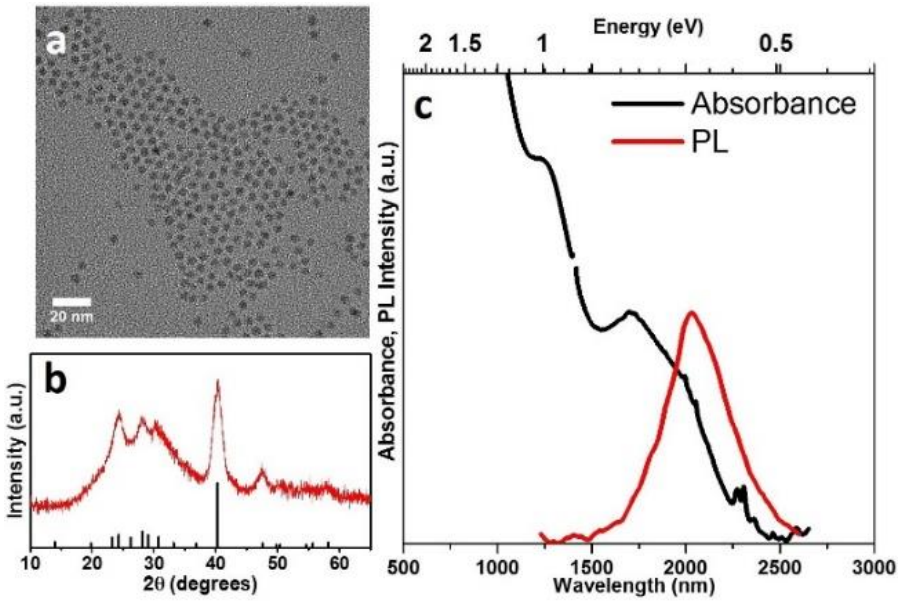

Figure 2.10. Cd_3As_2 NCs prepared using $As(NMe_2)_3$ and DIBAL-H. (a) TEM image of 4.5 nm Cd_3As_2 NCs. (b) Powder X-ray diffraction patterns of Cd_3As_2 NCs. The vertical lines on the bottom are the corresponding positions and intensities of X-ray reflections for bulk tetragonal Cd_3As_2. (c) Representative Absorption and PL traces of ~6nm Cd_3As_2 NCs

The DIBAL-H concentration did not have a sharp effect on the Cd_3As_2 NC size as seen for InAs. This may be due to the fact that the kinetics of this reaction are much faster than InAs NC formation. Temperature variation was found to be a more efficient strategy for tuning the NC size where higher temperatures led to larger average NC size as monitored by the PL spectra of the NCs (Figure 2.11a). The bare Cd_3As_2 NCs showed strong band-edge luminescence without any shell growth. Time resolved PL decay of small Cd_3As_2 NCs with PL maximum at 1300 nm is shown in Figure 2.11b. The trace could be fitted to a bi-exponential function with decay times of 24.1 ns ($A_1 = 0.4$) and 85.2 ns ($A_2 = 0.58$) respectively. Lack of fast radiative decay in bare cores indicated that Cd_3As_2 based nanomaterials can be a potential candidate for emission applications in the region of 1200 nm- 3000 nm.

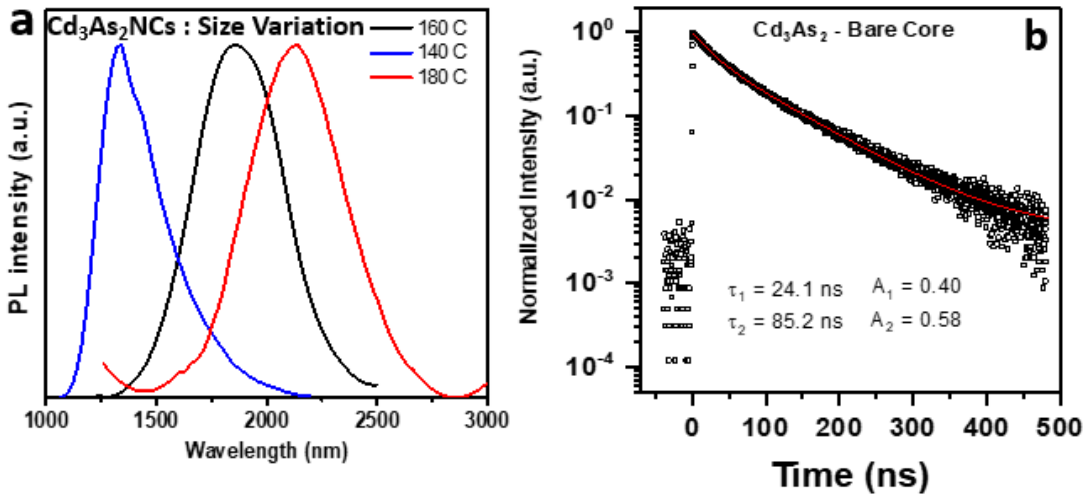

Figure 2.11. Emission from Cd_3As_2 NCs. (a) PL spectra of Cd_3As_2 NCs grown at different temperature and (b) time-resolved PL decay of small Cd_3As_2 NCs (corresponding to blue curve in the panel (a)).

2.7 Conclusions

In summary, a new approach to synthesize arsenide based semiconductor nanocrystals (InAs and Cd_3As_2) starting from a commercially available precursor, $As(NMe_2)_3$, was demonstrated in this chapter. The NCs synthesized by this method have high crystallinity, show well resolved excitonic features and are luminescent in the infra-red. DIBAL-H plays a crucial role in governing the nanocrystal size and hence can be used as a handle to precisely tune the final size of the nanocrystals. We believe that this new synthetic approach will promote further research on these infra-red emitters due to its relative ease as compared to previous approaches which required dealing with toxic gases or synthesizing the precursors under rigorous conditions. This approach also opens up a platform for the systematic investigation of reducing agent mediated synthesis of III-V nanocrystals starting from aminopnictide precursors. The role of reducing agents in governing the kinetics on nanocrystals formation is the subject of the next chapter in this thesis.

2.8 References

1. Talapin, D. V.; Lee, J.-S.; Kovalenko, M. V.; Shevchenko, E. V., Prospects of colloidal nanocrystals for electronic and optoelectronic applications. *Chemical reviews* **2009,** *110* (1), 389-458.
2. Kovalenko, M. V.; Manna, L.; Cabot, A.; Hens, Z.; Talapin, D. V.; Kagan, C. R.; Klimov, V. I.; Rogach, A. L.; Reiss, P.; Milliron, D. J.; Guyot-Sionnnest, P.; Konstantatos, G.; Parak, W. J.; Hyeon, T.; Korgel, B. A.; Murray, C. B.; Heiss, W., Prospects of Nanoscience with Nanocrystals. *ACS Nano* **2015,** *9* (2), 1012-1057.
3. Talapin, D. V.; Murray, C. B., PbSe nanocrystal solids for n-and p-channel thin film field-effect transistors. *Science* **2005,** *310* (5745), 86-89.
4. Klem, E. J.; Levina, L.; Sargent, E. H., PbS quantum dot electroabsorption modulation across the extended communications band 1200–1700 nm. **2005**.
5. Michalet, X.; Pinaud, F.; Bentolila, L.; Tsay, J.; Doose, S.; Li, J.; Sundaresan, G.; Wu, A.; Gambhir, S.; Weiss, S., Quantum dots for live cells, in vivo imaging, and diagnostics. *science* **2005,** *307* (5709), 538-544.
6. McDonald, S. A.; Konstantatos, G.; Zhang, S.; Cyr, P. W.; Klem, E. J. D.; Levina, L.; Sargent, E. H., Solution-processed PbS quantum dot infrared photodetectors and photovoltaics. *Nat Mater* **2005,** *4* (2), 138-142.

7. Gong, X.; Yang, Z.; Walters, G.; Comin, R.; Ning, Z.; Beauregard, E.; Adinolfi, V.; Voznyy, O.; Sargent, E. H., Highly efficient quantum dot near-infrared light-emitting diodes. *Nature Photonics* **2016**.
8. Jaworski, F.; Jack, M.; Bawendi, M.; Scherer, J.; Geyer, S. In *The use of colloidal quantum dots on focal plane arrays for optical communications*, 2012 IEEE Photonics Society Summer Topical Meeting Series, 9-11 July 2012; 2012; pp 127-127.
9. Sargent, E. H., Colloidal quantum dot solar cells. *Nature photonics* **2012,** *6* (3), 133-135.
10. Aharoni, A.; Mokari, T.; Popov, I.; Banin, U., Synthesis of InAs/CdSe/ZnSe Core/Shell1/Shell2 Structures with Bright and Stable Near-Infrared Fluorescence. *Journal of the American Chemical Society* **2006,** *128* (1), 257-264.
11. Allen, P. M.; Liu, W.; Chauhan, V. P.; Lee, J.; Ting, A. Y.; Fukumura, D.; Jain, R. K.; Bawendi, M. G., InAs(ZnCdS) Quantum Dots Optimized for Biological Imaging in the Near-Infrared. *Journal of the American Chemical Society* **2010,** *132* (2), 470-471.
12. Soreni-Harari, M.; Mocatta, D.; Zimin, M.; Gannot, Y.; Banin, U.; Tessler, N., Interface Modifications of InAs Quantum-Dots Solids and their Effects on FET Performance. *Advanced Functional Materials* **2010,** *20* (6), 1005-1010.
13. Liu, W.; Chang, A. Y.; Schaller, R. D.; Talapin, D. V., Colloidal InSb Nanocrystals. *Journal of the American Chemical Society* **2012,** *134* (50), 20258-20261.
14. Yarema, M.; Kovalenko, M. V., Colloidal Synthesis of InSb Nanocrystals with Controlled Polymorphism Using Indium and Antimony Amides. *Chemistry of Materials* **2013,** *25* (9), 1788-1792.
15. Hines, M. A.; Scholes, G. D., Colloidal PbS Nanocrystals with Size-Tunable Near-Infrared Emission: Observation of Post-Synthesis Self-Narrowing of the Particle Size Distribution. *Advanced Materials* **2003,** *15* (21), 1844-1849.
16. Keuleyan, S.; Lhuillier, E.; Brajuskovic, V.; Guyot-Sionnest, P., Mid-infrared HgTe colloidal quantum dot photodetectors. *Nat Photon* **2011,** *5* (8), 489-493.
17. Peng, X.; Wickham, J.; Alivisatos, A. P., Kinetics of II-VI and III-V Colloidal Semiconductor Nanocrystal Growth: "Focusing" of Size Distributions. *Journal of the American Chemical Society* **1998,** *120* (21), 5343-5344.
18. Nozik, A. J.; Mićić, O. I., Colloidal quantum dots of III-V semiconductors. *MRs Bulletin* **1998,** *23* (02), 24-30.
19. Franke, D.; Harris, D. K.; Xie, L.; Jensen, K. F.; Bawendi, M. G., The Unexpected Influence of Precursor Conversion Rate in the Synthesis of III–V Quantum Dots. *Angewandte Chemie International Edition* **2015,** *54* (48), 14299-14303.
20. Wells, R. L.; Pitt, C. G.; McPhail, A. T.; Purdy, A. P.; Shafieezad, S.; Hallock, R. B., The use of tris(trimethylsilyl)arsine to prepare gallium arsenide and indium arsenide. *Chemistry of Materials* **1989,** *1* (1), 4-6.
21. Zhang, J.; Zhang, D., Photoluminescence and Growth Kinetics of High-Quality Indium Arsenide and InAs-Based Core/Shell Colloidal Nanocrystals Synthesized Using Arsine (AsH3) Generated via Zinc Arsenide as the Arsenic Source. *Chemistry of Materials* **2010,** *22* (4), 1579-1584.
22. Das, A.; Shamirian, A.; Snee, P. T., Arsenic Silylamide: An Effective Precursor for Arsenide Semiconductor Nanocrystal Synthesis. *Chemistry of Materials* **2016**.
23. Uesugi, H.; Kita, M.; Omata, T., Synthesis of size-controlled colloidal InAs quantum dots using triphenylarsine as a stable arsenic source. *Journal of Crystal Growth* **2015,** *416*, 134-141.

24. Tessier, M. D.; Dupont, D.; De Nolf, K.; De Roo, J.; Hens, Z., Economic and Size-Tunable Synthesis of InP/ZnE (E = S, Se) Colloidal Quantum Dots. *Chemistry of Materials* **2015,** *27* (13), 4893-4898.
25. Song, W.-S.; Lee, H.-S.; Lee, J. C.; Jang, D. S.; Choi, Y.; Choi, M.; Yang, H., Amine-derived synthetic approach to color-tunable InP/ZnS quantum dots with high fluorescent qualities. *Journal of nanoparticle research* **2013,** *15* (6), 1-10.
26. Aubin, M.; Caron, L.; Jay-Gerin, J., Band structure of cadmium arsenide at room temperature. *Physical Review B* **1977,** *15* (8), 3872.
27. Jeon, S.; Zhou, B. B.; Gyenis, A.; Feldman, B. E.; Kimchi, I.; Potter, A. C.; Gibson, Q. D.; Cava, R. J.; Vishwanath, A.; Yazdani, A., Landau quantization and quasiparticle interference in the three-dimensional Dirac semimetal Cd3As2. *Nat Mater* **2014,** *13* (9), 851-856.
28. Harris, D. K.; Allen, P. M.; Han, H.-S.; Walker, B. J.; Lee, J.; Bawendi, M. G., Synthesis of cadmium arsenide quantum dots luminescent in the infrared. *Journal of the American Chemical Society* **2011,** *133* (13), 4676-4679.
29. Xie, R.; Zhang, J.; Zhao, F.; Yang, W.; Peng, X., Synthesis of Monodisperse, Highly Emissive, and Size-Tunable Cd3P2 Nanocrystals. *Chemistry of Materials* **2010,** *22* (13), 3820-3822.
30. Li, D.; Peng, L.; Zhang, Z.; Shi, Z.; Xie, R.; Han, M.-Y.; Yang, W., Large scale synthesis of air stable precursors for the preparation of high quality metal arsenide and phosphide nanocrystals as efficient emitters covering the visible to near infrared region. *Chemistry of Materials* **2014,** *26* (12), 3599-3602.
31. Lagrone, C. B.; Schauer, S. J.; Thomas, C. J.; Gray, G. M.; Watkins, C. L.; Krannich, L. K., Reactivity of R2AlH (R = Me, Bui) with Selected Aminoarsines and Secondary Amines. *Organometallics* **1996,** *15* (10), 2458-2464.
32. Watkins, C. L.; Krannich, L. K.; Thomas, C. J.; Srivastava, D., The reactivity of dimethylaluminum hydride with the aminoarsines Me2AsNMe2, MeAs(NMe2)2, and As(NMe2)3. *Polyhedron* **1994,** *13* (24), 3299-3307.
33. Tessier, M. D.; De Nolf, K.; Dupont, D.; Sinnaeve, D.; De Roo, J.; Hens, Z., Aminophosphines: A Double Role in the Synthesis of Colloidal Indium Phosphide Quantum Dots. *J. Am. Chem. Soc.* **2016,** *138* (18), 5923-5929.
34. Shevchenko, E. V., Talapin, D.V., Schnablegger, H., Kornowski, A., Festin, O., Svedlindh, P., Haase, M., Weller, H., Study of Nucleation and Growth in the Organometallic Synthesis of Magnetic Alloy Nanocrystals: The Role of Nucleation Rate in Size Control of CoPt3 Nanocrystals. *J. Am. Chem. Soc.* **2003,** *125* (30), 9090-9101.
35. Kim, K.; Yoo, D.; Choi, H.; Tamang, S.; Ko, J.-H.; Kim, S.; Kim, Y.-H.; Jeong, S., Halide–Amine Co-Passivated Indium Phosphide Colloidal Quantum Dots in Tetrahedral Shape. *Angew. Chem. Int. Ed.* **2016,** *55* (11), 3714-3718.
36. Rolo, A.; Vasilevskiy, M., Raman spectroscopy of optical phonons confined in semiconductor quantum dots and nanocrystals. *J. Raman. Spectr.* **2007,** *38* (6), 618-633.
37. Xie, R.; Peng, X., Synthetic Scheme for High-Quality InAs Nanocrystals Based on Self-Focusing and One-Pot Synthesis of InAs-Based Core–Shell Nanocrystals. *Angewandte Chemie International Edition* **2008,** *47* (40), 7677-7680.

Chapter 3.

Role of reducing agents in Aminoarsine based synthesis of InAs Quantum Dots: Search for an optimal reducing agent

3.1 Introduction

Aminopnictides have recently emerged as convenient and versatile precursors for the synthesis of III-V quantum dots (QDs). The recent exploration of aminophosphines as precursors for synthesis of InP QDs has re-ignited general interest in aminopnictides as safer and economic alternatives to their tris-trimethylsilyl-pnictide counterparts.[1] Initial reports have suggested and demonstrated the need for an additional reducing agent to *in situ* transform As(+III) to As(-III) state which participates in the formation of InAs QDs.[2] The use of DIBAL-H as an appropriate reducing agent for this approach was detailed in the previous chapter. Griegel *et. al.* showed that $P(NEt_2)_3$ can also behave as a reducing agent for aminoarsine precursors to enable the formation of InAs QDs.[3] Similarly, reductive activation of aminostibine precursors enabled the successful synthesis of InSb QDs.[4] The success of these approaches has conclusively demonstrated the potential of aminopnictides as precursors for synthesis of III-V QDs. The next step is to develop approaches to control the reaction kinetics and produce monodisperse QD populations using this approach.

Indium Arsenide (InAs) QDs are one of the promising candidates for SWIR applications as they combine the superior electronic and optoelectronic properties of the III-V semiconductor family with the virtues of size tunable optical properties and solution processability afforded by colloidal QDs.[5] Colloidal InAs QDs show size tunable emission in the critical SWIR window of 750 nm-1400 nm where the main competitor is PbS QDs.[6-7] The toxicity and chemical instability of PbS makes InAs a more favorable choice for both bio imaging and optoelectronic devices.[8-9]

An important advantage of InAs over PbS is its tetrahedrally coordinated zinc blende lattice that can be expitaxially matched to a variety of III-V and II-VI materials in core-shell nanostructures. However the synthesis of InAs QDs has lagged behind II-VI and IV-VI semiconductor QDs due to the lack of suitable group V precursors and increased covalency of the III-V lattice.[10-11] The broad size distributions observed for as-synthesized III-V nanocrystals (NCs) are an important factor limiting their use in commercial applications.[12] Since the first colloidal synthesis of InAs using the Wells' dehalosilylation reaction[13] between Indium chloride and tris-trimethylsilyl arsine ($(TMS)_3As$), the community has extensively explored the reactions between InX_3 (where X=halide or carboxylate) and $\{E(CH_3)_3\}_3As$ (where E=Si or Ge) seeking to improve the size distribution of InAs QDs.[7, 14-17] However efforts to tune precursor conversion kinetics to achieve temporal separation between nucleation and growth have only been moderately successful in the case of III-V NCs.[16, 18] Several other arsenic precursors have been explored but with limited success.[19-21] It has been established that III-V NCs synthesized using these approaches involve non classical nucleation and growth processes where NC growth occurs through the formation of cluster-like intermediates.[22-23] Pre-synthesized InAs clusters can be used as precursors for the size focused growth from smaller seeds resulting in populations of InAs QDs with reasonably narrow size distributions.[24] Even though significant advances have been made in the understanding of InAs QD synthesis, the commercial unavailability, chemical instability and acute toxicity of $(TMS)_3As$ introduce a bottleneck for systematic exploration of InAs QDs in thin-film devices.

In this chapter, I show that the hydride donor ability of the reducing agent can be used as the tuning knob for the kinetics of QD nucleation and growth. Alane N, N-dimethyethylamine complex (DMEA-AlH_3), a well-known reductant in organic synthesis, is shown to be a superior reducing agent for the controlled activation of aminoarsines in the synthesis of InAs QDs. This

simple, one-pot approach leads to monodisperse spherical InAs QDs with tunable sizes that show band edge emission. The optimized reaction kinetics enables the narrowest absorption and emission linewidths for InAs QDs synthesized from convenient aminoarsine precursors. This work demonstrates the possibility of rational tuning the reaction space in the synthesis of colloidal III-V QDs.

3.2 Control of precursor conversion kinetics in NC syntheses

According to the LaMer model of nucleation and growth[25] (Figure 3.1a), the synthesis of a monodisperse colloid should be designed in such a way that the monomer concentration increases rapidly to above the critical saturation limit when a short burst of nucleation occurs. These nuclei then grow rapidly to lower the monomer concentration below the critical limit, thereby allowing further particle growth at a rate determined by the slowest step in the process. The time scale of the nucleation stage in this model determines the temporal separation between nucleation and growth and hence the monodispersity of the colloid. In the general reaction scheme, In^{+III} + As^{+III} + [Reductant] → InAs, the reducing ability of the reducing agent can be used as a handle to control the precursor conversion rate. An optimal reducing agent should maximize temporal separation between nucleation and growth stages of NC formation (see orange curve in Figure 1a) while not triggering undesired side reactions such as reduction of In^{III} to In^{0}. We hypothesized that if the reducing agent used in the synthesis is weak, such as $P(NEt_2)_3$, the precursor conversion will be slow and should result in a broad size distribution whereas if the reducing agent is too strong, such as $LiEt_3BH$ it may lead to simultaneous reduction of both In(+III) and As(+III) (See Figure 3.1b).

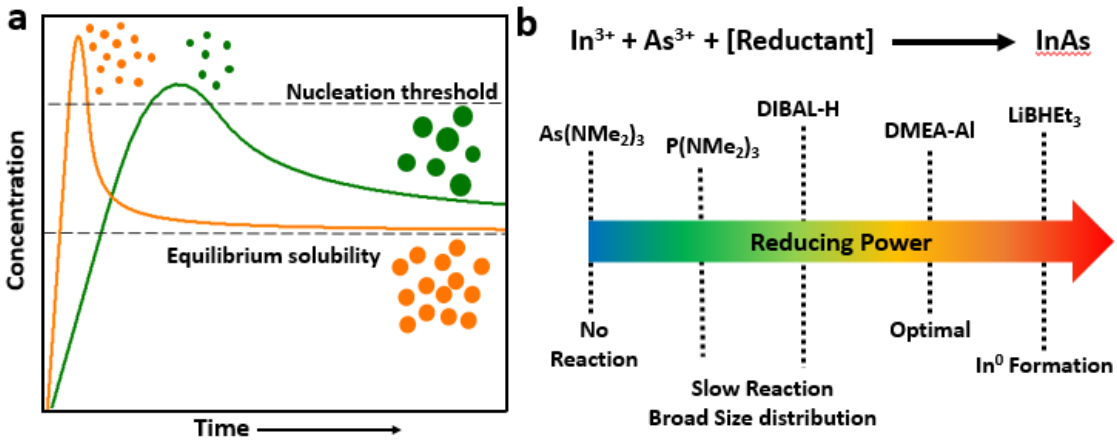

Figure 3.1. Controlling nanocrystals formation kinetics (a) LaMer model for the synthesis of colloidal nanocrystals. The scheme represents the effect of precursor conversion kinetics on the size distribution of final NC population. The orange curve represents the case where fast precursor conversion leads to a shorter nucleation event whereas the green curve shows the case where the nucleation stage persists for longer due to slow conversion kinetics leading to a broad size distributions. (b) Schematic depiction of the reducing power of different reducing agents used in this work and their effect on the formation of InAs nanocrystals.

3.3 Comparison of InAs QDs synthesized using different reducing agents.

InAs QDs can be synthesized with $P(NEt_2)_3$, DIBAL-H, DMEA-AlH_3 and $LiEt_3BH$ as reducing agents. In a typical reaction, 0.4 mmol of $InCl_3$ was dissolved in 6 mL Oleylamine and heated to temperatures in the range of 150°C to 200°C. Subsequently, 1 molar equivalent of ($As(NMe_2)_3$) (0.4mmol) and 3 molar equivalents of the reducing agent were sequentially injected into the flask and the reaction mixture was heated further to a desired temperature (240°C-280°C). The DIBAL-H and $P(NEt_2)_3$ based syntheses were optimized based on the reported protocols.[2-3] We found that the size and size distribution of the final product were strongly dependent on the reducing agent used. InAs QDs synthesized using DMEA-AlH_3 as the reducing agent showed a significantly narrower size distribution than the InAs QDs synthesized using other reducing agents. Figure 3.2 shows the absorption spectra of similar sized InAs QDs obtained by using $P(NEt_2)_3$,

DIBAL-H and DMEA-AlH_3 complex for comparison. InAs QDs produced from $LiEt_3BH$ showed featureless absorption spectrum.

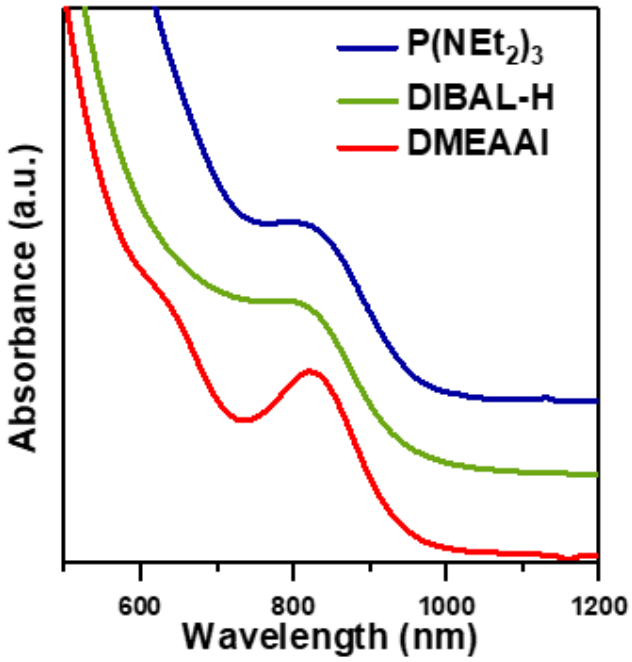

Figure 3.2. Absorption spectra of small InAs QDs (~2.5 nm) synthesized using different reducing agents.

The effect of different reducing agents on the size distribution of InAs QDs can be rationalized in terms of their respective precursor conversion rates. For example, the weakly reducing $P(NEt_2)_3$ did not react with a solution of $InCl_3$ and $As(NMe_2)_3$ in oleylamine at room temperature and had to be injected at elevated temperatures in the reaction mixture to crystallize InAs NCs. However, when we injected DIBAL-H or DMEA-AlH_3 in the reaction mixture at room temperature, the reaction mixture slowly turned red indicating the formation of molecular intermediates related to InAs ("clusters") (Figures 3.3 and Figure 3.4). The broad absorption spectra indicated that these intermediates were not homogenous in nature.

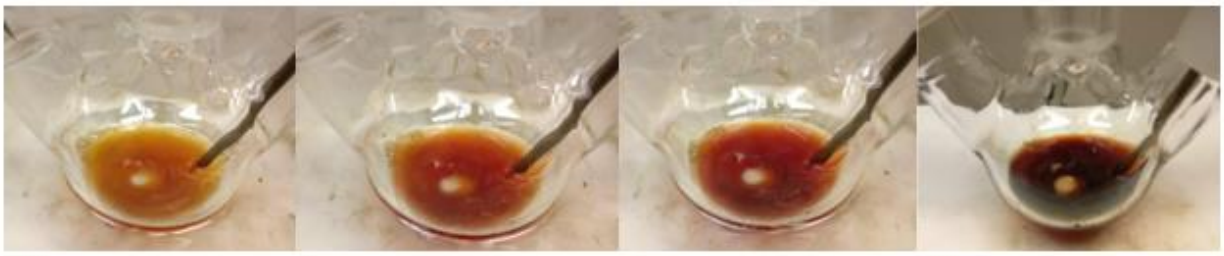

Figure 3.3. **InAs molecular intermediates ("clusters").** Temporal snapshots of the formation of InAs nanoclusters at room temperature when DMEA-Al was used as the reducing agent. The coloration takes place when 0.6mmol of DMEA-Al is injected into 0.2 mmol of $InCl_3$ and $As(NMe)_3$ in 6 mL oleylamine.

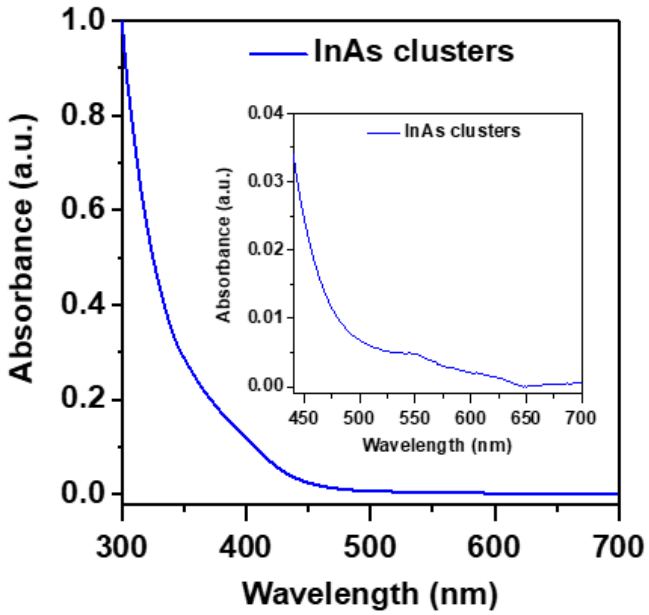

Figure 3.4. Absorption spectrum of amorphous InAs "clusters" produced when the reaction shown in Figure 3a is run at room temperature. The absorption tail in the red is responsible for the deep red color of the solutions in Figure 3.3.

We monitored the evolution of absorption of solutions at 400 nm with time as a reporter of the the precursor conversion kinetics with different reducing agents (Figure 3.5). We found that the precursor conversion was faster when DMEA-AlH_3 was used as the reducing agent as compared to DIBAL-H. On the other hand, when the strongly reducing $LiEt_3BH$ was injected into a solution of $InCl_3$ and $As(NMe_2)_3$ in oleylamine, we observed the reduction of $InCl_3$ to In metal

along with the formation of large InAs crystallites likely via a solution-liquid-solid process[26] (Figure 3.6). The reducing ability of main group hydrides can be quantified in terms of their hydride donor ability. Heiden *et.al.* computed the hydride donor ability of $LiEt_3BH$ to be 24 kcal/mol which is in close agreement to experimentally measured value of 26 kcal/mol.[27] DMEA-AlH_3 and DIBAL-H were found to be 37 kcal/mol and 46 kcal/mol less reducing than $LiEt_3BH$ respectively which explains the reduction of In^{III} to In^0 by $LiEt_3BH$.[28] On the other hand, both DIBAL-H and DMEA-AlH_3 selectively cleave the As-N bond in aminoarsine to produce As-H bonded intermediates which further react with In^{3+} to form InAs.[2] Since DMEA-AlH_3 is slightly more reducing than DIBAL-H, the aminoarsine activation with DMEA-AlH_3 leads to a more uniform nucleation event which leads to monodisperse InAs QDs.

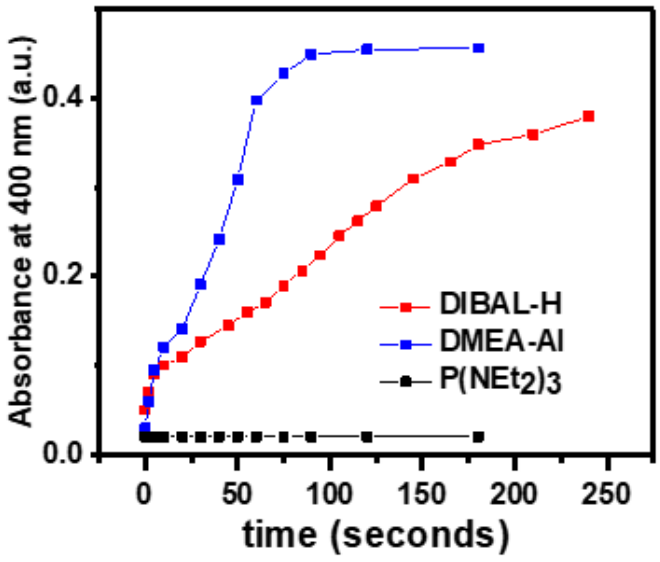

Figure 3.5. **Kinetics of InAs cluster formation** when DIBAL-H and DMEA-Al are used as the reducing agents. The absorbance was monitored at 400 nm at regular time intervals after the injection of the reducing agent into a diluted mixture of In and As stock solutions in toluene.

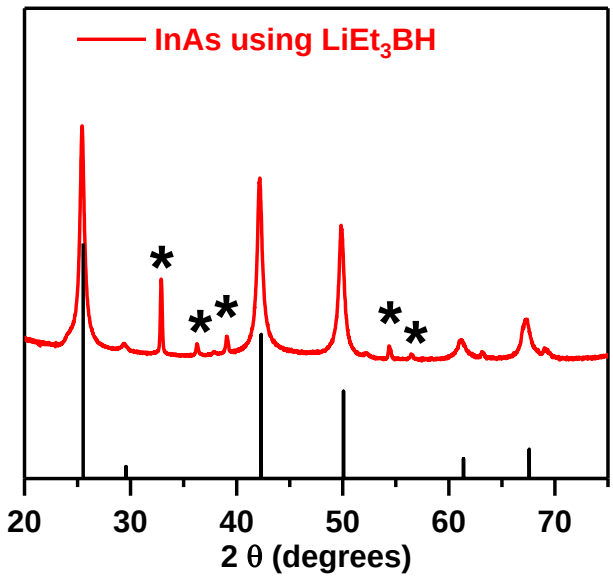

Figure 3.6. InAs from $LiEt_3BH$. X-ray diffraction pattern of the product obtained when $LiEt_3BH$ (superhydride) was used as the reducing agent in place of DMEA-Al. The injection temperature was 150°C. * indicated peaks related to metallic indiums. Vertical lines correspond to the peaks of bulk InAs. The sharp peaks indicate the large size of the InAs nanocrystals obtained when $LiEt_3BH$ is used as the reducing agent.

3.4 Monodisperse InAs QDs synthesized using Dimethylethylamine-Alane Complex

The general reaction scheme for the synthesis of monodisperse InAs QDs using DMEA-AlH_3 as the reducing agent is shown in Figure 3.7a. In a typical synthesis, 0.4 mmol $InCl_3$ and 6mL Oleylamine were loaded in a 100 mL 3-neck flask and dried at 120° C under vaccum for 1 hr. The reaction mixture was then brought to a desired temperature (150°C -220°C) depending on the target NC size. The As stock solution (0.4 mmol $As(NMe_2)_3$ was dissolved in 1 mL dry Oleylamine and kept at 40°C for 2 mins till bubbles stopped evolving. This bubble formation indicates transamination and the evolution of dimethylamine.) was then quickly injected into the flask followed by the injection of 2.4mL of 0.5 M DMEA-Al in toluene. The temperature was then further increased to 240°-290°C depending on the target NC sizes. The reaction was cooled to room temperature and transferred into a nitrogen glovebox. The reaction mixture was diluted with

5 mL toluene and 15 mL ethyl alcohol was added to precipitate the NCs. The washing cycle was repeated twice and the precipitated particles were resdispered in toluene for further characterization. Representative absorption spectra of several different sizes of InAs QDs synthesized using this approach are shown in Figure 3.7b. All the absorption spectra were collected on diluted aliquots taken directly out of the reaction pot without any washing or precipitation. Well resolved excitonic features can be seen for all the InAs QD sizes. A representative TEM image of ~ 3.5 nm InAs QDs (λ_{max} = 850 nm) is shown in Figure 2c. The powder X-ray diffraction pattern (Figure 3.7d) of the InAs QDs was consistent with the cubic zinc blende crystal structure of bulk InAs. QD sizes calculated from the width of the 111 diffraction peak were in a good agreement with the sizes estimated from TEM images. The sizes of InAs QDs could be tuned by varying the injection temperatures and the final synthesis temperatures. We observed that larger InAs QDs could be obtained when DMEA-AlH_3 injection was performed at higher temperatures (Figure 3.8a). The NC size could also be increased by increasing the final crystallization temperature (Figure 3.8b). The reaction was monitored by taking aliquots and terminated as soon as the desired NC size was reached. Lattice fringes could be clearly seen in high resolution TEM images (Figure 3.9) indicating good crystallinity of the particles. ICP-OES analyses showed that the QDs were In-rich and there was no Al incorporation in the QDs from the reducing agent (Table 3.1).

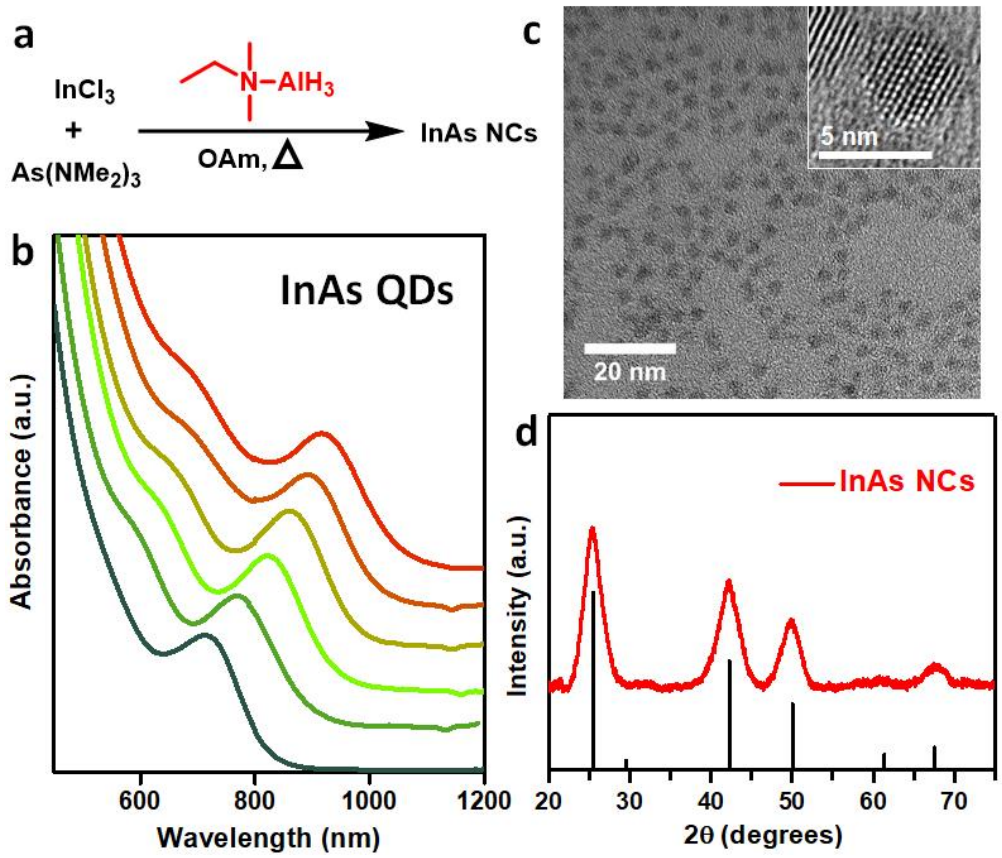

Figure 3.7. Characterization of InAs QDs synthesized using DMEA-AlH_3 as the reducing agent (a) Reaction scheme for the synthesis of InAs QDs using DMEA-AlH_3 as the activating agent for $As(NMe_2)_3$. (b) Absorption spectra of several different sizes of InAs QDs synthesized using this approach. (c) TEM image of ~3.5 nm InAs QDs Inset: High resolution TEM of InAs QD showing lattice planes. (d) Powder X-ray diffraction pattern of InAs QDs. The vertical lines show the corresponding positions and intensities of X-ray reflections for bulk InAs.

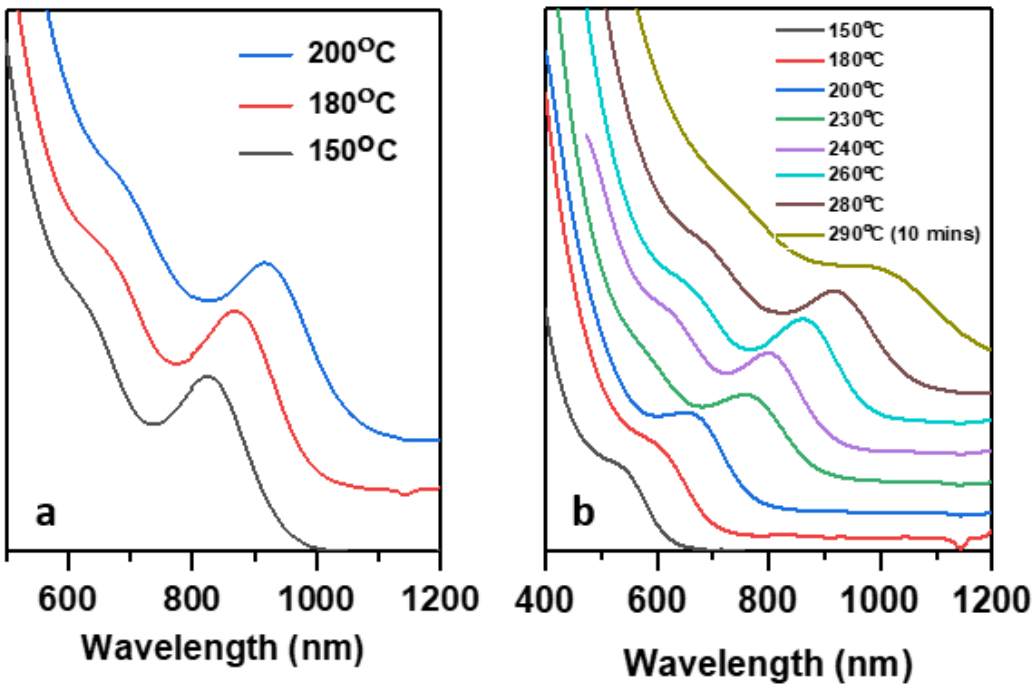

Figure 3.8. **Tuning InAs QD size**. (a) Absorption Spectra of InAs QDs where the DMEA-Al was injected at different temperatures. The reaction was terminated at 250°C in all the cases. All other parameters were kept constant across the three reactions to the best of our abilities. (b) NC growth with temperature after DMEA-Al injection at 150°C. The size distribution becomes worse if the reaction is kept at high temperature (290°C) for long.

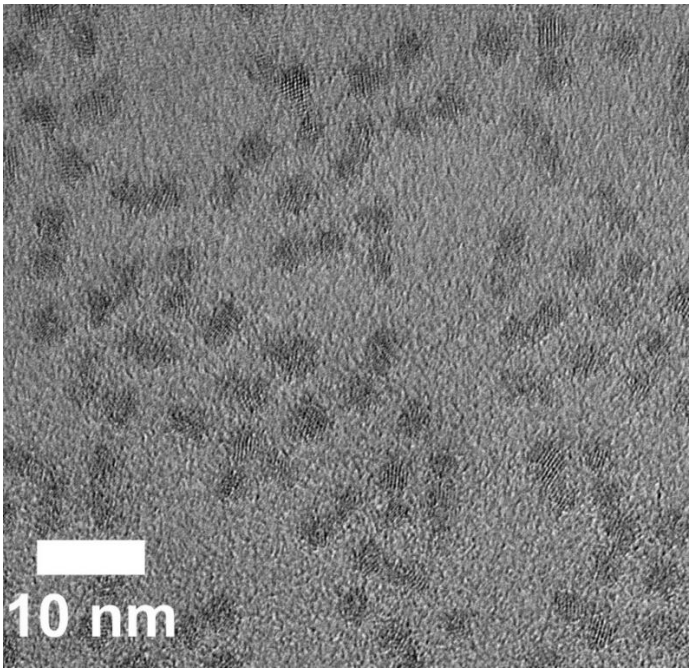

Figure 3.9. High-resolution TEM image of InAs QDs showing well resolved lattice fringes in multiple individual nanocrystals.

Sample	In (ppm)	As (ppm)	Al (ppm)	In:As molar ratio
InAs NCs	19.88	9.07	0.02	1.42

Table 3.1. Elemental composition of InAs NCs obtained from ICP-OES analysis.

We also used small-angle X-ray scattering (SAXS) measurements to calculate the size distribution of a representative sample. Figure 3.10a shows the experimental SAXS curve. A mean particle size of 3.4 nm with a standard deviation of 0.5 nm was extracted from the fit. This value is in agreement with TEM measurements and agrees well with the HWHM analysis of the absorption spectra. Figure 3.10b shows a large area TEM image of the InAs QDs corresponding to the SAXS curve.

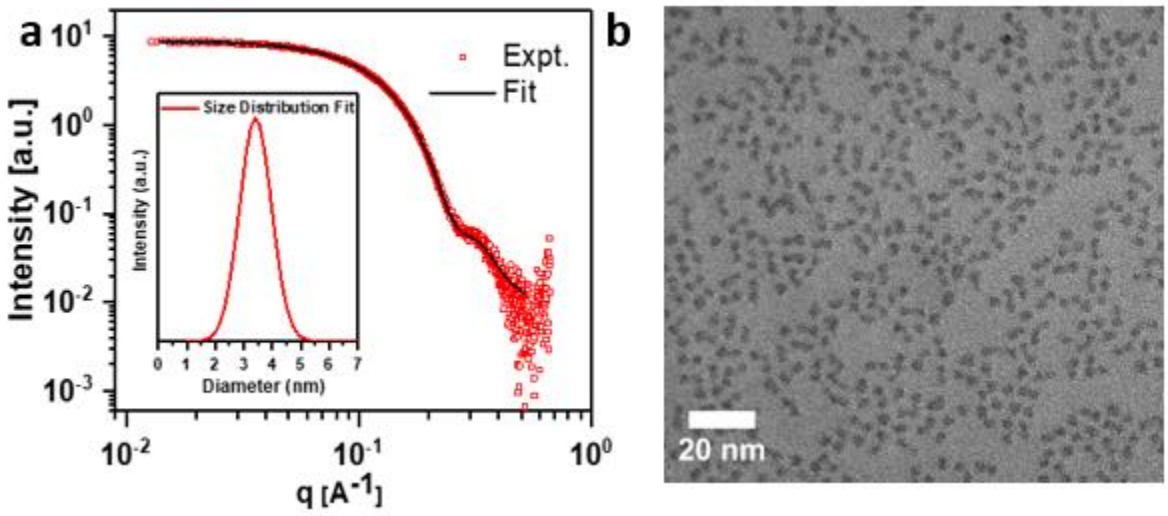

Figure 3.10 Estimation of InAs QDs size distribution. (a) SAXS curve (red squares) and fit (black line) for a colloidal solution of ~ 3.4 nm InAs QDs. Inset shows the size distribution extracted from the fit. (b) A large area TEM image showing the homogeneity of the InAs QD populations.

The half-width-at-half-maximum (HWHM) at the first excitonic peak ($1S_e$-$1S_h$) was also used as an estimate for the size distribution of InAs QDs. Figure 3.11 compares the HWHM of various sized InAs QDs prepared using different reducing agents. The HWHM of InAs QDs

synthesized using DMEA-AlH_3 was significantly lower than those of InAs QDs synthesized using DIBAL-H and $P(NEt_2)_3$ for all accessible sizes.

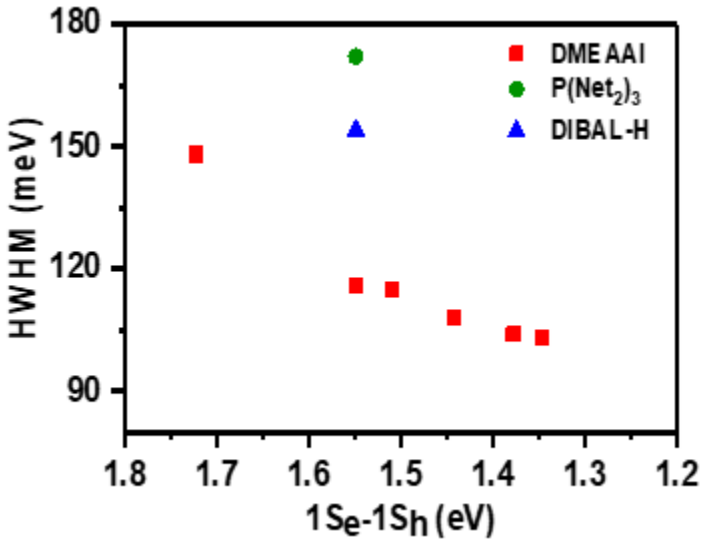

Figure 3.11. Comparison of HWHM of the first excitonic peak of InAs QDs synthesized by different approaches showing relative size dispersions.

3.5 Amorphous InAs clusters as growth precursors for InAs QDs

Another salient feature of this approach is the ability to perform a heat-up synthesis without compromising the size distribution of the resultant InAs QDs which lends it the ability to scale up the reaction. InAs "clusters" produced by the room temperature reduction using DMEA-AlH_3 could be converted into monodisperse InAs QDs upon heating to a desired temperature (Figure 3.12a). We were also able to extend the size range of InAs QDs by using the clusters formed at room temperature as the reactants for performing over-growth of pre-synthesized InAs QDs. Slow syringe pump injection of the InAs "clusters" to a solution of purified InAs QDs at 220°C led to an increase of InAs QD size without a significant increase in the size distribution (Figure 3.12b). A similar approach has been used by Tamang *et.al.* where they used clusters synthesized by the room temperature reaction of $In(oleate)_3$ and $(TMS)_3As$ as precursors for size focused growth of

pre-syntheszied InAs seeds. We believe that further optimization of the growth protocols can yield monodisperse InAs QDs in an extended size range.

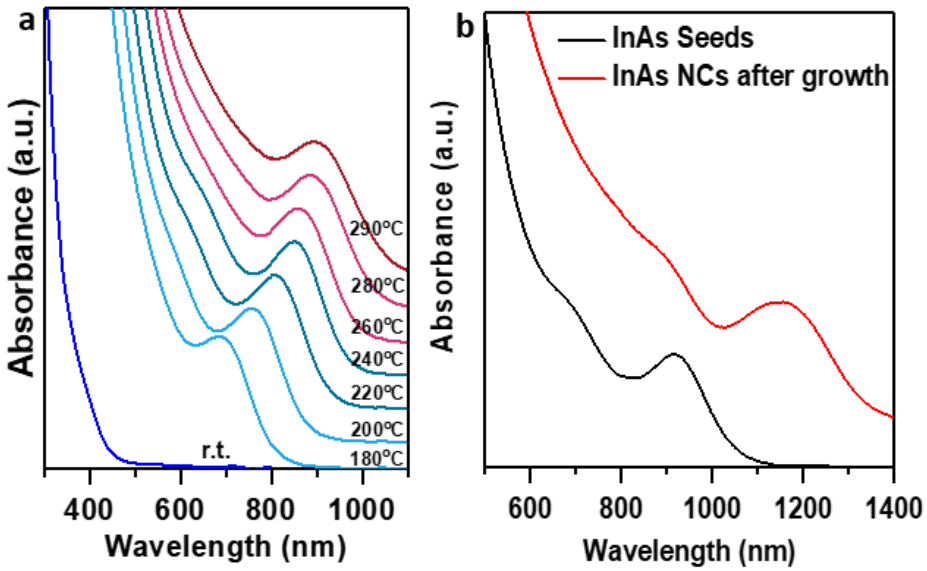

Figure 3.12. InAs clusters as growth precursors. (a)Transformation of InAs clusters formed at the room temperature (r.t.) into InAs NCs upon heating. (b) Absorption spectra of initial seeds and particles after seeded growth using InAs clusters formed at room temperature.

3.6 Tunable Near IR emission from InAs QDs

As-synthesized InAs QDs also showed band-edge emission for all synthesis batches. Figure 3.13 a shows an example PL spectrum along with the corresponding absorption spectrum. PL spectra of the different sized InAs QDs are shown in Figure 3.13b. A narrow emission linewidth of 130 meV (97 nm) was obtained for the InAs QDs emitting at 1.28 eV (~970 nm). These linewidths are comparable to the best reported InAs QDs of similar sizes.[16] Quantum yields of about ~1% were measured for as-synthesized InAs QDs using IR-125 dye (Indocyanine green, φ =13.6 %) as a reference which are comparable to those reported for InAs NCs synthesized using $(TMS)_3As$.[7] The emission intensities can be significantly enhanced by growing a shell of an

appropriate II-VI material (ZnSe or CdSe) as has been shown in the previous chapter and many other reports.[3, 29]

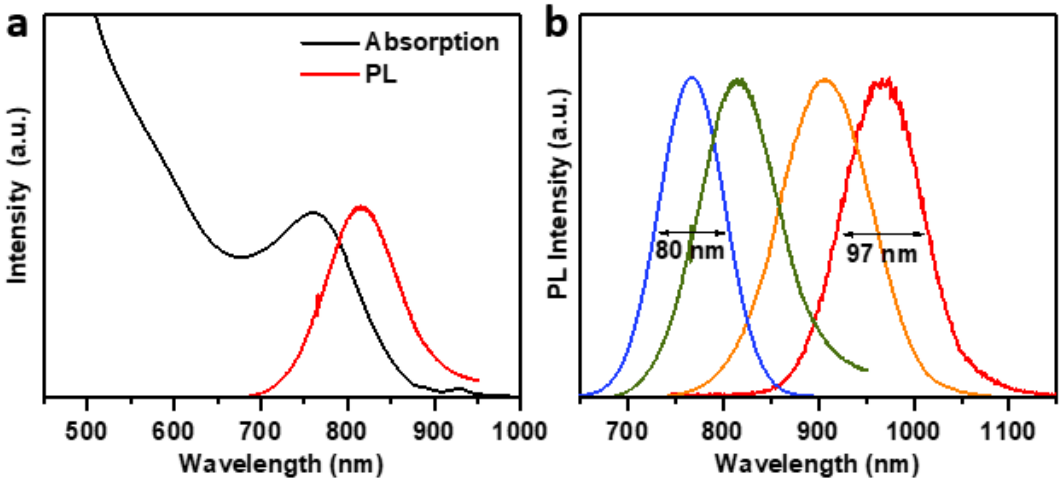

Figure 3.13 Emission characteristics of InAs QDs (a) Representative Absorption and PL spectrum of small InAs QDs. (b) PL spectra of different InAs QD sizes with emission centered between 760 nm and 970 nm.

3.7 Conclusions

In conclusion, it was demonstrated that careful selection of the reducing agent for activation of tris(dimethylamino)arsine precursor enables formation of high quality InAs QDs. Our work shows that the choice of reducing agent (hydride donor) plays an important role in determining the precursor conversion kinetics and hence the size distribution of the final QD population. InAs QDs synthesized using this approach are significantly more monodisperse as compared to InAs particles produced using other aminoarsine based approaches and comparable to those prepared using multistep procedures using $(TMS)_3As$. There is a broad selection of commercially available reducing agents whose hydride donor ability is tabulated through experimental and computational studies.[27] I believe that this concept can be extended to the synthesis of other III-V QDs using aminopnictide precursors. Although powerful, this approach was not able to lead to the formation of colloidal GaAs nanocrystals. It turned out that the reducing

ability of neither DIBAL-H nor DMEA-AlH3 was strong enough to balance the reaction kinetics and yield crystalline GaAs nanocrystals. This failure points to the fact that harsher approaches are required for the crystallization of GaAs NCs. In the next chapter, I will elaborate on a novel synthetic route to colloidal GaAs NCs.

3.8 References

1. Tessier, M. D.; De Nolf, K.; Dupont, D.; Sinnaeve, D.; De Roo, J.; Hens, Z., Aminophosphines: A Double Role in the Synthesis of Colloidal Indium Phosphide Quantum Dots. *J. Am. Chem. Soc.* **2016,** *138* (18), 5923-5929.
2. Srivastava, V.; Janke, E. M.; Diroll, B. T.; Schaller, R. D.; Talapin, D. V., Facile, Economic and Size-Tunable Synthesis of Metal Arsenide Nanocrystals. *Chem. Mater.* **2016,** *28* (18), 6797-6802.
3. Grigel, V.; Dupont, D.; De Nolf, K.; Hens, Z.; Tessier, M. D., InAs Colloidal Quantum Dots Synthesis via Aminopnictogen Precursor Chemistry. *J. Am. Chem. Soc.* **2016,** *138* (41), 13485-13488.
4. Liu, W.; Chang, A. Y.; Schaller, R. D.; Talapin, D. V., Colloidal InSb Nanocrystals. *Journal of the American Chemical Society* **2012,** *134* (50), 20258-20261.
5. Nozik, A. J.; Mićić, O. I., Colloidal quantum dots of III-V semiconductors. *MRs Bulletin* **1998,** *23* (02), 24-30.
6. Hines, M. A.; Scholes, G. D., Colloidal PbS Nanocrystals with Size-Tunable Near-Infrared Emission: Observation of Post-Synthesis Self-Narrowing of the Particle Size Distribution. *Advanced Materials* **2003,** *15* (21), 1844-1849.
7. Guzelian, A. A.; Banin, U.; Kadavanich, A. V.; Peng, X.; Alivisatos, A. P., Colloidal chemical synthesis and characterization of InAs nanocrystal quantum dots. *Appl. Phys. Lett.* **1996,** *69* (10), 1432-1434.
8. Ihly, R.; Tolentino, J.; Liu, Y.; Gibbs, M.; Law, M., The Photothermal Stability of PbS Quantum Dot Solids. *ACS Nano* **2011,** *5* (10), 8175-8186.
9. Soo Choi, H.; Liu, W.; Misra, P.; Tanaka, E.; Zimmer, J. P.; Itty Ipe, B.; Bawendi, M. G.; Frangioni, J. V., Renal clearance of quantum dots. *Nat. Biotech.* **2007,** *25*, 1165.
10. Hendricks, M. P.; Campos, M. P.; Cleveland, G. T.; Jen-La Plante, I.; Owen, J. S., A tunable library of substituted thiourea precursors to metal sulfide nanocrystals. *Science* **2015,** *348* (6240), 1226-1230.
11. Franke, D.; Harris, D. K.; Xie, L.; Jensen, K. F.; Bawendi, M. G., The Unexpected Influence of Precursor Conversion Rate in the Synthesis of III–V Quantum Dots. *Angewandte Chemie International Edition* **2015,** *54* (48), 14299-14303.
12. Owen, J.; Brus, L., Chemical Synthesis and Luminescence Applications of Colloidal Semiconductor Quantum Dots. *J. Am. Chem. Soc.* **2017,** *139* (32), 10939-10943.
13. Wells, R. L.; Pitt, C. G.; McPhail, A. T.; Purdy, A. P.; Shafieezad, S.; Hallock, R. B., The use of tris(trimethylsilyl)arsine to prepare gallium arsenide and indium arsenide. *Chemistry of Materials* **1989,** *1* (1), 4-6.

14. Xie, R.; Peng, X., Synthetic Scheme for High-Quality InAs Nanocrystals Based on Self-Focusing and One-Pot Synthesis of InAs-Based Core–Shell Nanocrystals. *Angew. Chem. Int. Ed.* **2008,** *47* (40), 7677-7680.
15. Allen, P. M.; Liu, W.; Chauhan, V. P.; Lee, J.; Ting, A. Y.; Fukumura, D.; Jain, R. K.; Bawendi, M. G., InAs(ZnCdS) Quantum Dots Optimized for Biological Imaging in the Near-Infrared. *Journal of the American Chemical Society* **2010,** *132* (2), 470-471.
16. Franke, D.; Harris, D. K.; Chen, O.; Bruns, O. T.; Carr, J. A.; Wilson, M. W. B.; Bawendi, M. G., Continuous injection synthesis of indium arsenide quantum dots emissive in the short-wavelength infrared. *Nat. Comm.* **2016,** *7*, 12749.
17. Harris, D. K.; Bawendi, M. G., Improved Precursor Chemistry for the Synthesis of III–V Quantum Dots. *J. Am. Chem. Soc.* **2012,** *134* (50), 20211-20213.
18. Peng, X.; Wickham, J.; Alivisatos, A. P., Kinetics of II-VI and III-V Colloidal Semiconductor Nanocrystal Growth: "Focusing" of Size Distributions. *J. Am. Chem. Soc.* **1998,** *120* (21), 5343-5344.
19. Green, M.; Norager, S.; Moriarty, P.; Motevalli, M.; O'Brien, P., On the synthesis and manipulation of InAs quantum dots. *Journal of Materials Chemistry* **2000,** *10* (8), 1939-1943.
20. Das, A.; Shamirian, A.; Snee, P. T., Arsenic Silylamide: An Effective Precursor for Arsenide Semiconductor Nanocrystal Synthesis. *Chemistry of Materials* **2016**.
21. Uesugi, H.; Kita, M.; Omata, T., Synthesis of size-controlled colloidal InAs quantum dots using triphenylarsine as a stable arsenic source. *Journal of Crystal Growth* **2015,** *416*, 134-141.
22. Cossairt, B. M., Shining Light on Indium Phosphide Quantum Dots: Understanding the Interplay among Precursor Conversion, Nucleation, and Growth. *Chem. Mater.* **2016,** *28* (20), 7181-7189.
23. Gary, D. C.; Terban, M. W.; Billinge, S. J. L.; Cossairt, B. M., Two-step nucleation and growth of InP quantum dots via magic-sized cluster intermediates. *Chemistry of Materials* **2015,** *27* (4), 1432-1441.
24. Tamang, S.; Lee, S.; Choi, H.; Jeong, S., Tuning Size and Size Distribution of Colloidal InAs Nanocrystals via Continuous Supply of Prenucleation Clusters on Nanocrystal Seeds. *Chem. Mater.* **2016,** *28* (22), 8119-8122.
25. LaMer, V. K.; Dinegar, R. H., Theory, Production and Mechanism of Formation of Monodispersed Hydrosols. *J. Am. Chem. Soc.* **1950,** *72* (11), 4847-4854.
26. Trentler, T. J.; Hickman, K. M.; Goel, S. C.; Viano, A. M.; Gibbons, P. C.; Buhro, W. E., Solution-Liquid-Solid Growth of Crystalline III-V Semiconductors: An Analogy to Vapor-Liquid-Solid Growth. *Science* **1995,** *270* (5243), 1791-1794.
27. Heiden, Z. M.; Lathem, A. P., Establishing the Hydride Donor Abilities of Main Group Hydrides. *Organometallics* **2015,** *34* (10), 1818-1827.
28. Private communication with the author of ref 40, Zachariah M. Heiden. 2018.
29. Aharoni, A.; Mokari, T.; Popov, I.; Banin, U., Synthesis of InAs/CdSe/ZnSe Core/Shell1/Shell2 Structures with Bright and Stable Near-Infrared Fluorescence. *Journal of the American Chemical Society* **2006,** *128* (1), 257-264.

Chapter 4.
Colloidal GaAs Nanocrystals

4.1 Introduction

GaAs is arguably the most important member of the III-V semiconductor family due to its excellent electronic and optical properties.[1] The direct band gap (1.42eV at 300K), high electron mobility and saturation electron velocity, reliable p-type and n-type doping make GaAs a material of choice for top performing solar cells,[2] transistors,[3] lasers and LEDs.[4] GaAs has a large Bohr exciton diameter of 19 nm[5] and strong quantum confinement is expected to develop in sub-10 nm GaAs crystals. However, synthetic difficulties have severely restricted the exploration of GaAs nanostructures synthesized by solution techniques. Colloidal synthesis of III-V nanocrystals (NCs) has made significant progress in the recent years.[6] Robust protocols now exist for the synthesis of indium pnictides InP,[7-10] InAs[10-12] and InSb[13-14]. However, the information on synthesis of GaAs NCs is relatively scarce and contradictory as explained in the section below.

4.1.1 Prior attempts on synthesis of colloidal GaAs

In the past two decades, there have been several attempts at making GaAs NCs.[15-23] Bryne *et al* first reported the conversion of a monomeric arsinogallane precursor into solution dispersed amorphous GaAs.[17] The Wells dehalosilylation reaction[24] that works well for InP and InAs NCs yields poorly crystalline GaAs along with various byproducts. The aminoarsine reduction based approaches are also insufficient for the crystallization of GaAs as mentioned in the previous chapter. Alternative approaches like transmetallation[19] and cation exchange[15] appear to introduce impurities to GaAs NCs. The highly covalent lattice of III-V compounds, especially GaAs, is prone to the incorporation of a variety of structural defects.[25] Moreover, most gallium precursors are

highly oxophilic and are well known polymerization catalysts.[26] Traditional solid state approaches including metal-organic chemical vapor deposition (MOCVD) or molecular beam epitaxy (MBE) that yield uniform and defect free GaAs crystals are typically carried out at high temperatures and in a highly reducing environment.[27] At the same time, low temperature (<500° C) MBE grown GaAs shows defects like As_{Ga} antisites and Ga vacancies which in turn negatively affect charge carrier dynamics.[28-31] Colloidal synthesis is typically done at temperatures well below those used for CVD and related approaches to high quality GaAs. It is interesting to see how low growth temperature affects the properties of GaAs nanostructures and what can be done to circumvent the problems of traditional colloidal approach for nanocrystal synthesis.

4.1.2 Unusual Optical Properties of GaAs NCs

Notably, NCs prepared by all these methods do not show excitonic features in the absorption spectra.[15, 17, 19, 32] On the other hand, several reports have assigned absorption peaks to GaAs NCs but the peak assignments do not mutually agree.[16, 20, 22] Very recently, Park *et.al.* reported the formation of ~1.8 nm GaAs NCs which, upon growth of a ZnSe shell, showed a weak band edge emission.[23] However, since the GaAs core was grown in the presence of a 3-fold excess of Zn precursor, the possibility of Zn intercalation into the lattice and subsequent alloy formation could not be neglected. Atomistic pseudopotential calculations by Luo *et.al.* predict that free-standing GaAs NCs switch from direct to indirect band gap at sizes below 3.2 nm, when the conduction band minimum changes from Γ-valley to the *X*-valley.[33] The indirect transitions may originate from the presence of energetically closely spaced valleys in the conduction band of GaAs where the bottom of the *L*-valley is only 0.29 eV above the bottom of the Γ-valley (Figure 2a, inset). Because the electron effective mass in the Γ-valley ($m_{\Gamma}^{*}=0.063m_0$) is more than an order of magnitude smaller than m^* in the *L*- and *X*-valleys, the electrons in the direct Γ-valley are expected

to be more sensitive to the quantum confinement than in the indirect *L*- and *X*-valleys. The energy difference between the lowest quantum confined states in direct and indirect valleys is expected to decrease with decreasing the NC size and, at a certain size, a transition from direct to indirect band structure of NCs may occur.

4.1.3. A novel synthetic approach to GaAs NCs

The synthetic scheme presented here is inspired by CVD (chemical vapor deposition) synthesis of GaAs, where alkylgallium and arsine are reacted in the presence of H_2 at temperatures above 600°C.[27] We explored solution phase reactions between triethylgallium and various arsenic precursors (arsine AsH_3; tris-trimethylsilylarsine $As(SiMe_3)_3$ or TMS_3As; and tris-dimethylaminoarsine $As(NMe_2)_3$) in the presence of a strong reducing agent sodium triethylborohydride ($NaEt_3BH$), an appropriate surfactant and a high boiling solvent at elevated temperatures. The three arsenic precursors chosen in this work are the best known arsenic precursors for synthesis of III-V compounds, in the bulk and nanoscale. It is demonstrated here that GaAs NCs can be prepared from a variety of arsenic precursors under a reducing environment. The details of the synthesis and the rationale behind the approach are detailed in the section below

4.2 Superhydride mediated synthesis of GaAs Nanocrystals

4.2.1 General Considerations

Alkylgalliums like triethylgallium are well known Ga precursors for the synthesis of GaAs by CVD based approaches. Other Ga precursors such as $GaCl_3$ and $Ga(acac)_3$ were also considered and explored. From bond dissociation energy considerations, the Ga-Cl bond dissociation energy is is 481kJ/mol as compared to the Ga-C bond dissociation energy of 253kJ/mol. This makes $Ga(C_2H_5)_3$ a more suitable Ga precursor for the synthesis of GaAs. For $Ga(acac)_3$, the presence of carboxylates, which are a possible source of oxygen make it an unfavorable choice of precursor.

In terms of the precursor choices for arsenic, AsH_3 was chosen as the cleanest source of As, which is widely used for the synthesis of GaAs in the solid state community. $(TMS)_3As$ is a well-known precursor for metal-arsenide nanocrystals like InAs[34] and Cd_3As_2.[35] We also recently reported $As(NMe_2)_3$ as a new precursor for the synthesis of InAs and Cd_3As_2 NCs.[12] $As(NMe_2)_3$ has previously been employed as a precursor for the synthesis of GaAs NCs, however the formed particles were poorly crystalline.[20] Among all three As precursors, $As(NMe_2)_3$ has the advantages of commercial availability, relatively low cost and reasonable stability in air. The reactions between $Ga(C_2H_5)_3$ and As precursors were attempted in various solvents (octadecene, squalane, n-trioctylphosphine) with a variety of the capping agents (oleic acid, oleylamine, trioctylphosphine oxide, stearonitrile, dodecanethiol). Squalane and Hexadecylamine (HDA) were preferred as the reaction solvent and surfactant to avoid Ga-catalyzed polymerization of unsaturated compounds like 1-octadecene or oleylamine.[36] $NaEt_3BH$ was preferred because of the larger size of Na^+ cation as compared to Li^+, which reduced the possibility for cation intercalation into GaAs lattice.

4.2.2 Optimized synthesis of GaAs nanocrystals

In a typical reaction, 6 mmol HDA and 12 mL Squalane were loaded into a 100 mL 3 neck flask and dried under vaccum at 100° C for 2 hrs. Then 1 mmol triethylgallium and excess AsH_3 were injected into the solution at 60° C. Arsine was prepared and purified as described in Appendix 1). *AsH_3 is a toxic gas and should be handled with extreme care*. The reaction mixture turned pale yellow upon addition. 3 mmol $NaEt_3BH$ was quickly injected to the reaction mixture at 60° C and temperature was ramped to 290° C in 20 mins. Upon $NaEt_3BH$ injection, the reaction turned from pale yellow to deep orange to deep red. Subsequently the color changed from deep red to brown-black as the temperature reached 200° C. The flask was maintained at 290° C for 4-6 hours for complete crystallization. The reaction mixture was cooled to room temperature and transferred to

the glove box and diluted with 15 mL toluene. The product was washed twice with ethanol as the non-solvent and redispersed in toluene. The particles tend to settle down over a day without surface treatment.

The protocol for synthesis of GaAs NCs with $As(SiMe_3)_3$ or $As(NMe_2)_3$ as the arsenic precursor was essentially similar to the protocol discussed above. Instead of excess AsH_3, 1 mmol TMS_3As or 1mmol $As(NMe_2)_3$ were used. Rest of the procedure was same. We found the reactivity of all three As precursors to be similar in the presence of $NaEt_3BH$. Similar reaction yields were obtained from all the three As precursors and no apparent difference in crystallinity was observed.

The particles are highly crystalline with the cubic zinc blende crystal structure confirmed by powder X-ray diffraction patterns shown for GaAs NCs obtained from different As precursors (Figure 4.1a). The concentration of superhydride in the reaction mixture plays an important role in balancing the reactivity of the precursors and intermediates and hence modulating size of GaAs NCs. Figure 4.1b shows a series of XRD patterns for GaAs NCs of different size (calculated using the Scherrer equation) obtained with the $GaEt_3$:AsH_3:$NaEt_3BH$ ratios of 1:1:x, where x=1.0, 2.0, 2.5 and 3.0 respectively. No crystalline GaAs phase formed at temperatures as high as 350°C in the absence of $NaEt_3BH$ (Figure 4.2).

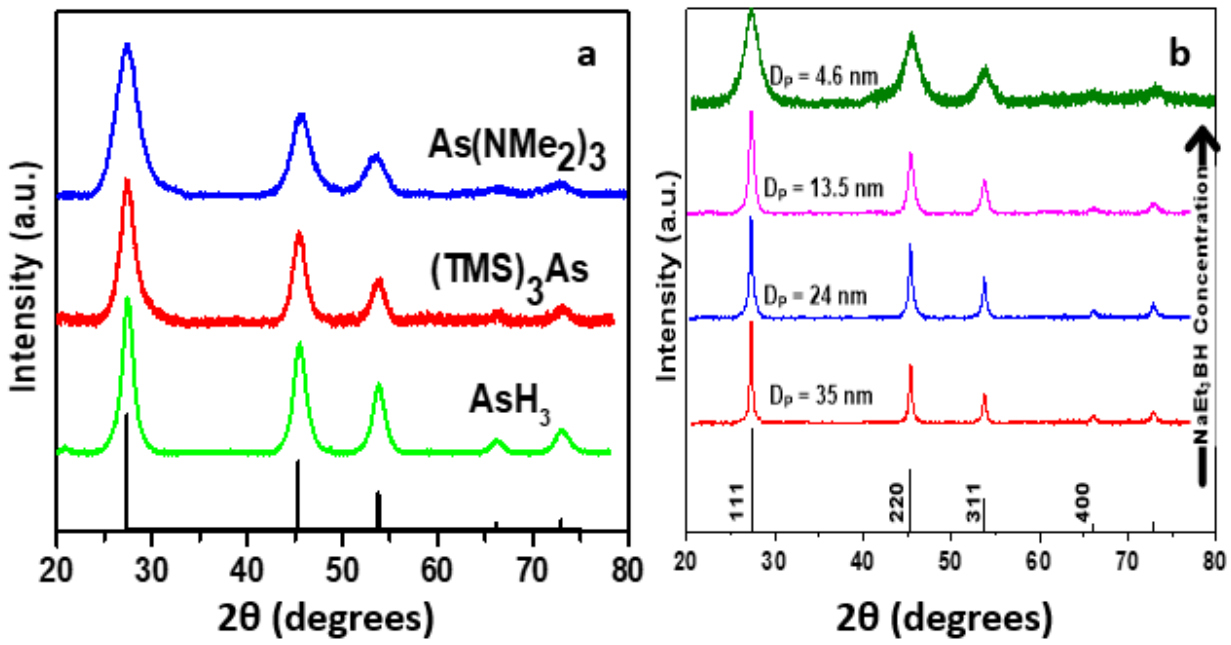

Figure 4.1. Synthesis of GaAs NCs from different arsenic precursors. (a) Representative X-ray diffraction patterns of GaAs NCs synthesized from different As precursors. The vertical lines show the corresponding positions and intensities of X-ray reflections for bulk GaAs (b) Powder X-ray diffraction patterns of GaAs NCs synthesized using AsH_3 and 1.0, 2.0, 2.5 and 3.0 molar equivalents of $NaEt_3BH$ (bottom to top).

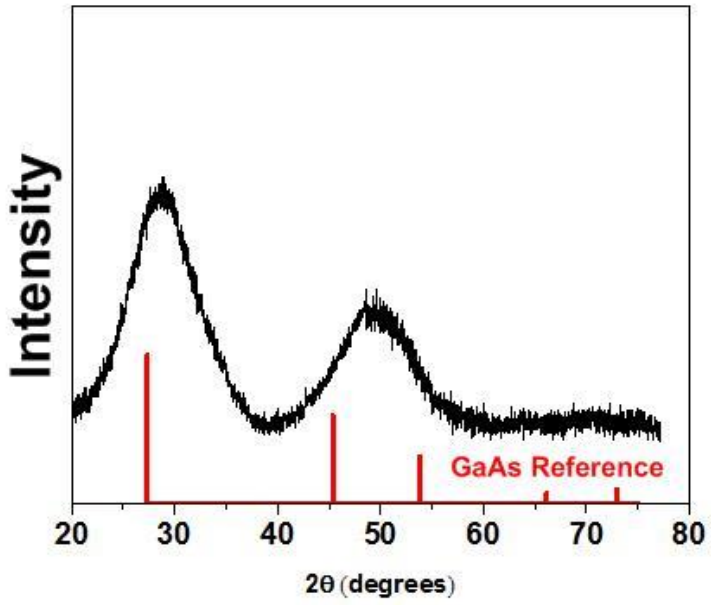

Figure 4.2. Powder X-ray diffraction pattern of the product of reaction between triethylgallium and arsine in the absence of $NaEt_3BH$ at 350° C.

4.3 Surface Treatment of GaAs Nanocrystals

As synthesized NCs showed poor colloidal stability and were encapsulated in a shell of amorphous byproducts (Figure 4.3). The amorphous shell likely consisted of organoboron polymers[37] and ICP-OES data showed the presence of boron in the isolated reaction products (Table S1). To purify as-synthesized GaAs NCs, we treated the reaction product with 1% ethanolic HCl solution which destroyed the boron containing polymeric aggregates and removed boron-containing contaminants (Table 4.1). The surface-treatment of large GaAs crystallites with aqueous HCl has previously been shown to leave excess As on the surface[38] which agreed with our ICP-OES studies. The purified GaAs NCs can be capped with ammonium sulfide forming stable colloids in formamide (FA). We attempted to stabilize GaAs NCs with traditional organic ligands (various combinations of oleylamine or hexadecylamine, oleic acid, dodecanethiol, trioctylphosphine, trioctylphosphine oxide, octadecylphosphonic acids) but were not successful. Ammonium sulfide is known to remove As_2O_3 from GaAs surface and install As-S bonds.[39] Sulfide ions are well known passivating agents for bulk GaAs surfaces[39-41] and have been previously used as ligands for various II-VI and III-V NCs.[42] ICP-OES elemental analysis of sulfide capped GaAs NCs showed a nearly stoichiometric Ga:As composition of 1:1.08 (Table 4.1). For TEM imaging and absorption measurements, the particles were transferred to toluene using didodecyldimethylammonium (DDA^+) as the counter-ion. The complete synthetic protocol is illustrated in Figure 4.4.

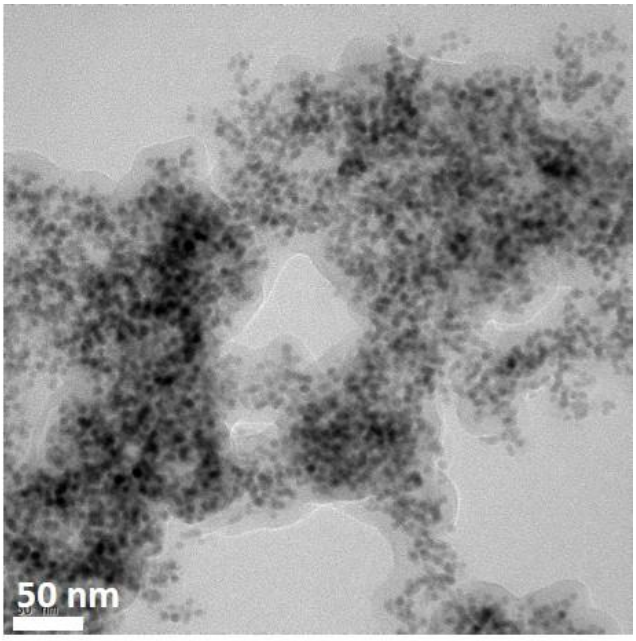

Figure 4.3.TEM image of as-synthesized GaAs nanocrystals. A polymeric coating seems to encapsulate the NCs and aggregate them.

Sample	Ga	As	B
GaAs (as-synthesized)	**1**	**1.03**	**1.33**
GaAs (HCl etch)	**1**	**1.34**	**0.02**
GaAs (Sulfide capped)	**1**	**1.08**	**0**

Table 4.1. ICP-OES analysis of GaAs nanocrystals at different stages of surface treatment. The values define the relative concentrations of different elements normalized to Ga.

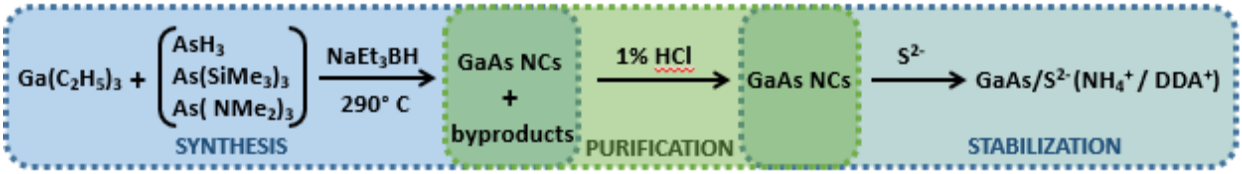

Figure 4.4. General synthetic scheme for the preparation of colloidal GaAs NCs.

4.4 Size selective precipitation to achieve monodisperse GaAs population

The surface treatment protocols yield colloidal GaAs nanocrystals in non-polar solvents like toluene. The size distribution of as-synthesized particles was rather polydisperse. A representative TEM image and absorption spectrum of as-synthesized GaAs NCs before size selection is shown in Figure 4.5 A photograph of colloidal GaAs NCs in toluene is also shown in Figure 4.5

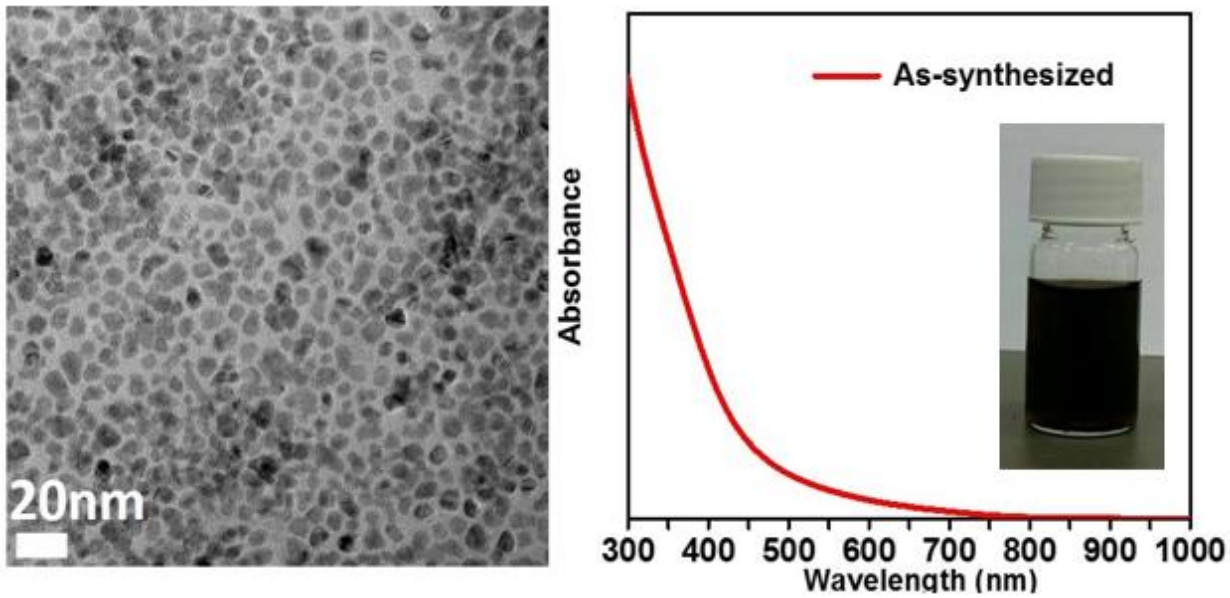

Figure 4.5. Representative TEM Image and Absorption spectrum of GaAs NCs before size selective precipitation.

The particles dispersed in toluene after the surface treatment were subjected to size selective precipitation after discarding the colloidally unstable portion. The NC population could be separated into several portions with tighter size distributions (Figures 4.6 and 4.7)

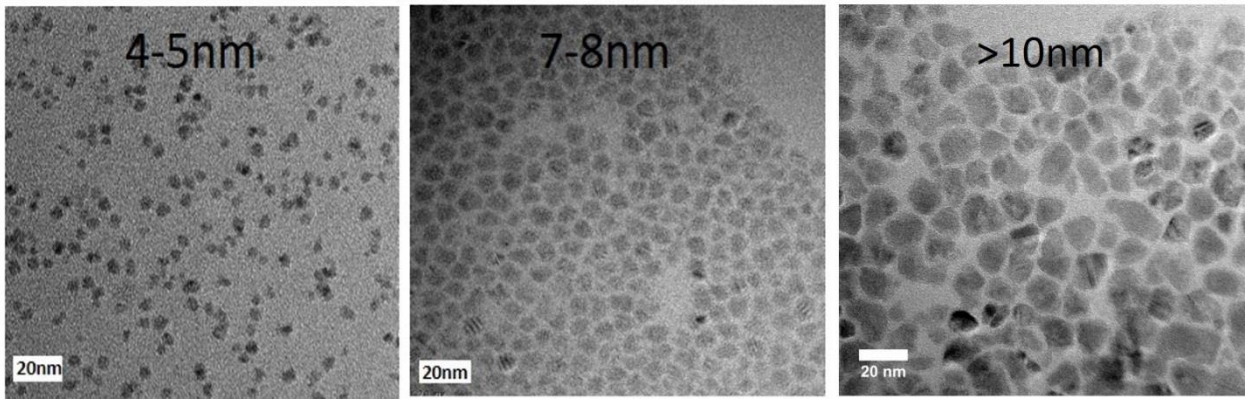

Figure 4.6. Representative TEM images of GaAs nanocrystals of various sizes obtained after size selective precipitation from a typical batch of synthesis.

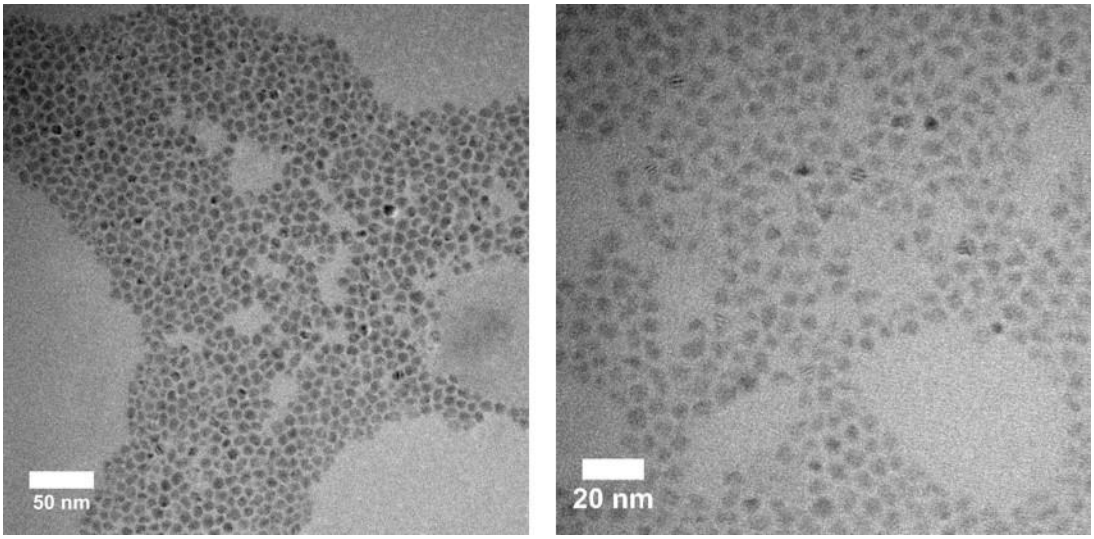

Figure 4.7. TEM Image of ~8nm and ~4nm GaAs NCs synthesized from AsH_3

Finally representative TEM images of size-selected, monodisperse poulations of GaAs NCs obtained from the three As precursors is shown in Figure 4.8. The particles are reasonably monodisperse and well separated from each other.

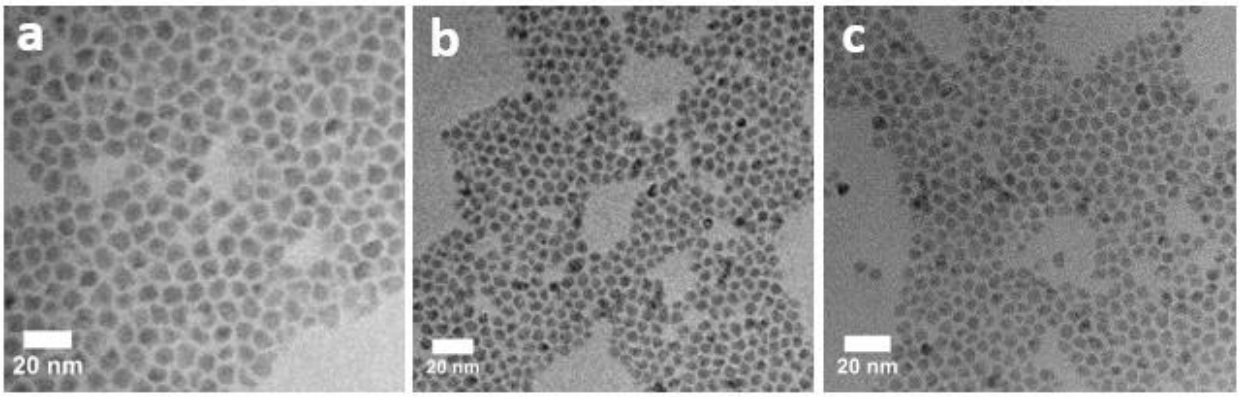

Figure 4.8. (a-c) TEM images of size-selected GaAs NCs synthesized using $Ga(C_2H_5)_3$ and AsH_3, TMS_3As and $As(NMe_2)_3$, respectively.

High resolution TEM images (Figure 4.9)of individual GaAs NCs and of a few GaAs NCs together show that the particles synthesized using this approach were highly crystalline. In certain cases typical nanocrystal defects like stacking faults could also be noticed.

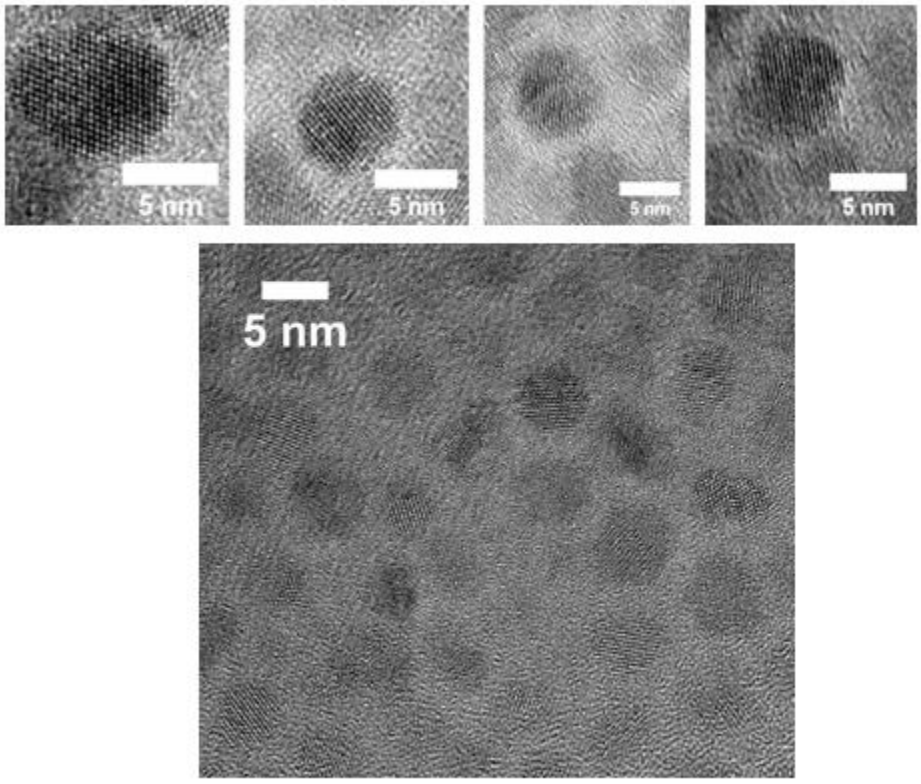

Figure 4.9. HRTEM images of GaAs NCs of various sizes synthesized from different As precursors.

Finally to quantitavely estimate the monodispersity of NC sizes in a size selected population of GaAs NCs, we employed small angle X-ray scattering (SAXS) measurements. Figure 4.10 a shows experimental SAXS curve. A mean particle size of 5.1 nm with a standard deviation of 0.8 nm was extracted from the fit (Schultz-Zimm intensity distribution function; inset in Figure 1i). SAXS scattering intensity levels off (i.e., approaches the Guinier region) below q ~ $5 \cdot 10^{-2}$ $Å^{-1}$, indicative of a good colloidal stability and absence of NC aggregates in the solution. Figure 4.10b shows the size distribution histogram determined from the TEM image of the particles used for SAXS measurements. Figure 4.11 shows TEM image and size distribution histogram of lager GaAs NCs (~8nm).

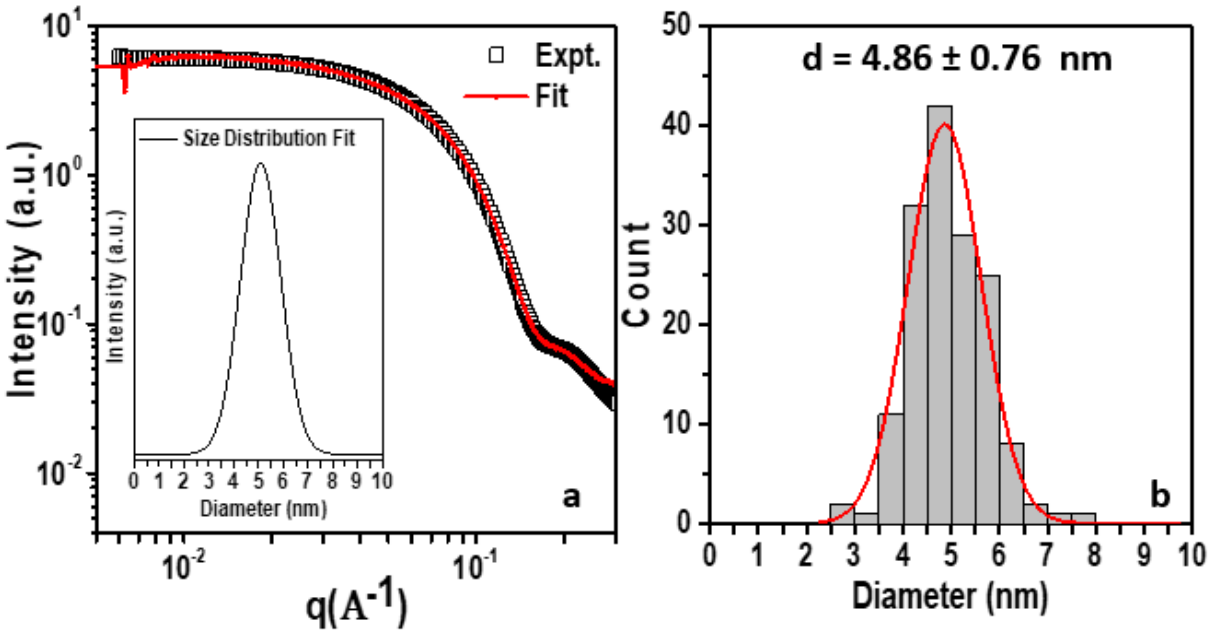

Figure 4.10. **Quantifying size distribution of GaAs NCs** (a) SAXS curve (black squares) and fit (red line) for a colloidal solution of ~5 nm GaAs NCs. The inset shows intensity distribution (Schultz-Zimm function) for the fit. (b) Histograms of particle size distribution as determined from TEM images of ~5 nm GaAs NCs prepared from $As(NMe_2)_3$. Corresponding TEM image is shown in Figure 4.8c.

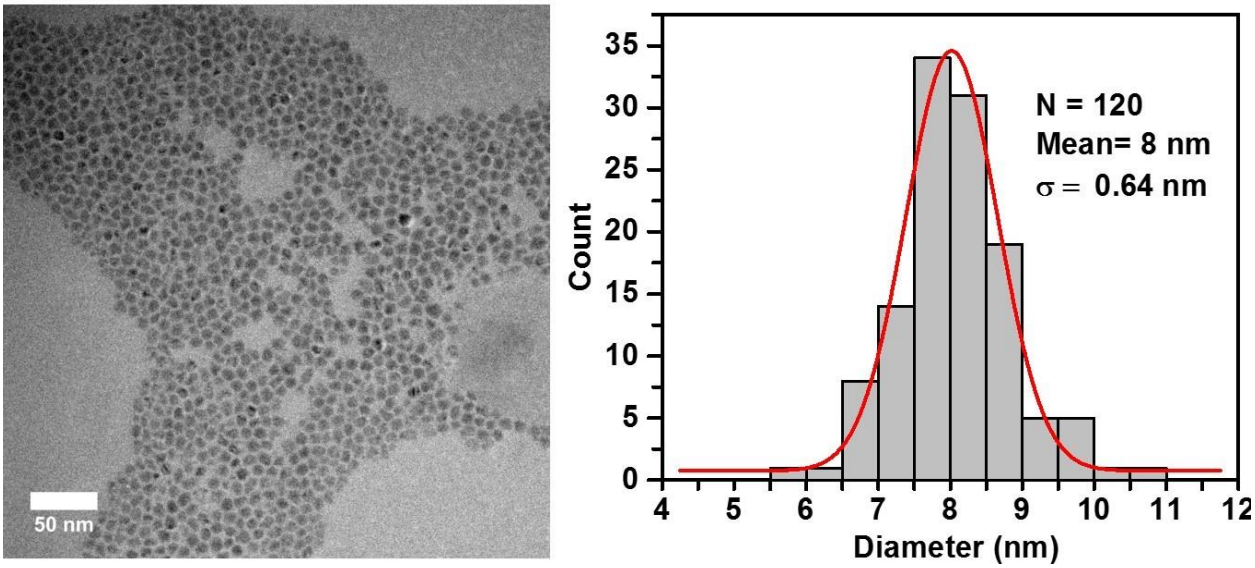

Figure 4.11. TEM image and Histogram of particle size distribution of larger GaAs NCs synthesized from AsH_3 after size-selective precipitation. The red curve shows a fit using a Gaussian distribution function. The mean particle size was found to be 8 nm with a standard deviation of 0.64 nm.

4.5 Absorption Spectroscopy of GaAs Nanocrystals

4.5.1 Steady State Absorption Spectra and Extinction Coefficients

The absorption spectra of direct-gap semiconductor NCs typically show size-dependent excitonic features.[43-44] The absence of a sharp blue shifted absorption edge in GaAs NCs compared to the bulk has generally been attributed to the lack of synthetic control over the purity of nanocrystals. The shallow absorption tail typically seen for colloidal GaAs NCs can also hint at possible indirect energy gap transitions getting activated at smaller sizes. However, the absorption spectra of size-selected fractions of GaAs NCs in the size range of 4 nm to 8 nm demonstrated only a steep rise of absorbance below 500 nm along with a structureless absorption tail at longer wavelengths (Figure 4.12). There was no measurable absorption below GaAs bulk band gap of 1.42 eV. There exists no information about the extinction coefficients of GaAs NCs in literature. In order to estimate the molar extinction coefficient of GaAs NCs, we first measured the absorption of thoroughly washed samples of GaAs NCs in toluene and subsequently determined their Ga

concentration using ICP-OES. The molar extinction coefficient for GaAs NCs at 350 nm was estimated as $5.7 \cdot 10^3$ $(M \cdot cm)^{-1}$ per GaAs unit or $2.1 \cdot 10^6$ $(M \cdot cm)^{-1}$ per 5 nm particle (Figure 4.13). These values are comparable to those reported for InP NCs.[45] We did not observe discrete excitonic transitions in GaAs NCs of any size despite reasonably narrow size distributions, which was also found in several previous reports.[15, 19] There are several publications reporting absorption peaks in the spectra of GaAs NCs,[16, 20-21] however, no size dependent spectral shifts have been observed and later studies have casted doubts on the relation of reported absorption features to GaAs NCs.[32]

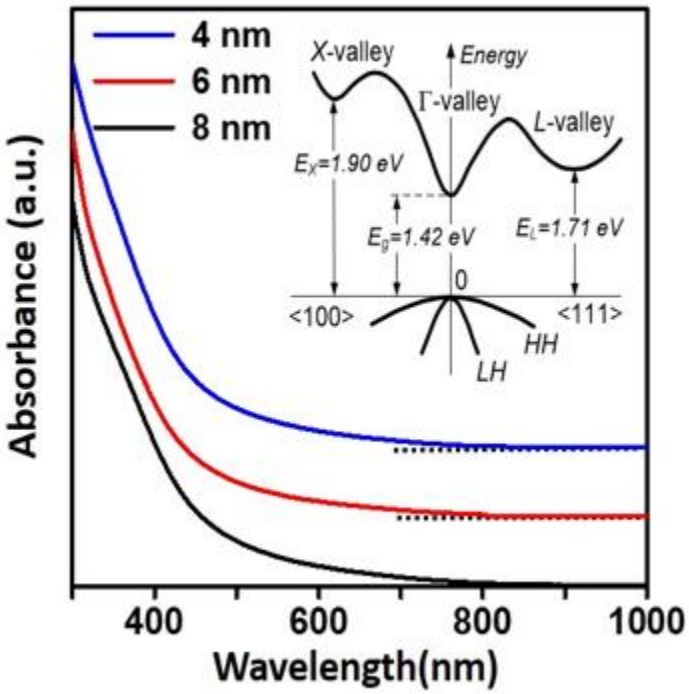

Figure 4.12. Steady state absorption of as-synthesized GaAs NCs. (a) Absorbance spectra of colloidal GaAs NCs with different average particle size synthesized using AsH_3 as the As precursor. GaAs NCs synthesized from other As precursors show similar features. The dotted horizontal lines show zero-absorbance baselines. The inset shows the band diagram of bulk GaAs at 300K. *HH* and *LH* are the notations for heavy and light holes, respectively.

4.5.2 Transient Absorption studies

A spectrally resolved picosecond transient absorption (TA) map of as-synthesized ~6 nm GaAs NCs is shown in Figures 4.13. TA signal is used to probe the exciton population dynamics in NCs by monitoring either an interband absorption bleach or an intra-band photoinduced absorption (PA).[46] Following 400 nm excitation, we observed a structureless PA signal across the entire visible spectrum for as-synthesized GaAs NCs. Similar behavior has been seen in Si[47] and other indirect-gap NCs with weak linear absorption at the band edge. Indirect gap NCs produce only a weak state-filling-induced bleach which is typically overwhelmed by strong intraband PA signal. TA data, as well as an structureless absorption tail in colloidal GaAs NCs could hint at possible indirect transitions in GaAs NCs. However in the light of predictions by Luo *et.al.*, it seems unlikely to observe an indirect bandgap effect in 8 nm GaAs NCs.[33]

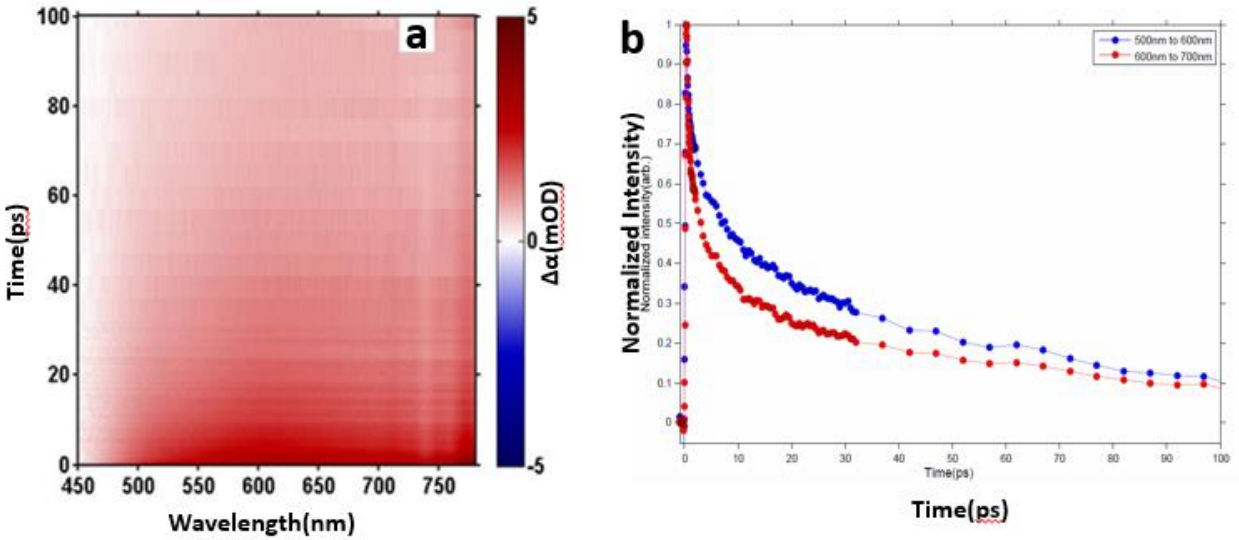

Figure 4.13. Transient absorption of as-synthesized GaAs NCs (a) Spectral color map of sub-100 ps transient absorption (TA) spectra for as synthesized ~5 nm GaAs NCs. (b) Photoinduced Absorption Decay Kinetics of GaAs NCs- as synthesized.

4.6 Characterization of disorder in GaAs Nanocrystals

The highly covalent lattice of GaAs requires temperatures upwards of 600° C for defect free crystallization.[27]. Stoichiometry related structural defects such as As_{Ga} antisites and Ga vacancies have been observed in GaAs films grown by MBE at low temperatures.[29] In light of the large molar extinction coefficient of colloidal GaAs NCs, it is unlikely that an indirect gap is the reason for the absence of excitonic features. However due to the low crystallization temperatures explored in the colloidal synthetic routes, it is likely that GaAs NCs accumulate a variety of structural defects in their lattice which may be responsible for the anomalous optical properties of colloidal GaAs NCs. We employed a multitude of characterization techniques such as Raman spectroscopy, Extended X-ray Absorption Fine Structure (EXAFS) analysis and Electron Paramagnetic Resonance spectroscopy (EPR) to better understand the nature of defects in these NCs. The sections below are dedicated to these measurements.

4.6.1 Raman Spectrum shows amorphous characteristics

Raman spectroscopy has been extensively used to characterize lattice defects in bulk GaAs.[29, 48-49] Raman scattering is a useful tool to study phonons at the centre of Brillioun zone and hence extract valuable information on the nature of structural defects and disorder in the lattice of nanocrystals.[50] The interaction between electrons and phonons in a semiconductor lattice plays a critical role in determining its optical properties.[51] The Raman spectra of as-synthesized GaAs NCs reveal a broad feature centered around 250 cm^{-1} and do not show characteristic LO and TO phonon modes at 267 cm^{-1} and 290 cm^{-1} present in the spectrum of single crystal GaAs (111) wafer used here as the reference sample (Figure 4.14). We noticed that our broad and shifted Raman spectra of as-synthesized GaAs NCs are very similar to those reported for ion-bombarded GaAs crystals where suppression of the phonon modes was attributed to a crystalline to amorphous transition.[49] Such Raman features point to a significant disorder in the lattice of GaAs NCs.

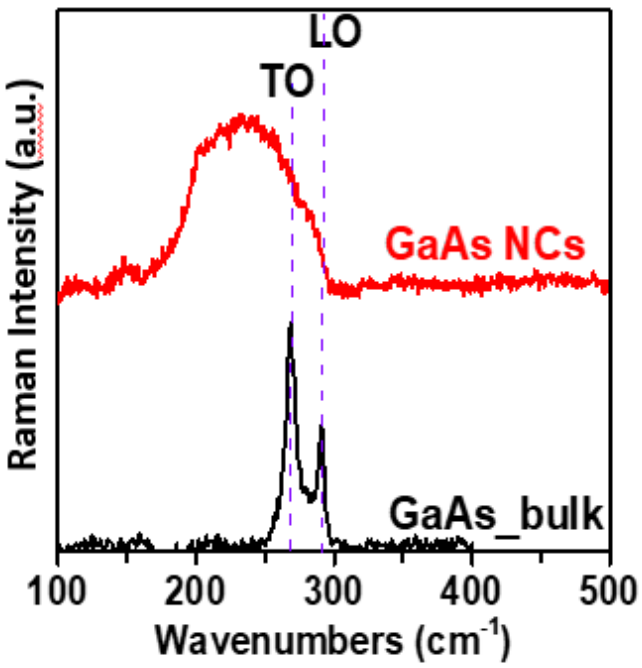

Figure 4.14. **Raman spectroscopy of GaAs NCs.** Raman spectra of bulk GaAs (black) and as-synthesized ~5 nm GaAs NCs (red).

4.6.2 EXAFS studies point to imbalanced Stoichiometry

X-ray absorption studies were also conducted on as-synthesized GaAs NCs and bulk GaAs powder to compare the local coordination environment of Ga and As atoms. Extended X-ray absorption fine structure (EXAFS) data were collected for as-synthesized GaAs NCs and bulk GaAs powder (99.999% , Aldrich) as standard to compare local geometry and coordination numbers of both Ga and As atoms in our GaAs NCs. The plots for the Fourier transformed absorption probability at the Ga and As K-edges for both GaAs NCs and bulk powder are shown in Figure S 4.15. The Ga K-edge spectra are identical for bulk GaAs powder and GaAs NCs indicating similar coordination environment for Ga atoms in the cubic GaAs lattice. For the As-K edge spectra, the reduced amplitude of Fourier transformed X-ray absorption for GaAs NCs as compared to bulk GaAs suggests that As atoms in GaAs NCs are undercoordinated relative to bulk GaAs. No signal corresponding to Ga-O or As-O bonds were evident in the EXAFS region. This

could be explained either by multiple Ga vacancies or As_{Ga}-antisite defects. These EXAFS results are in a qualitative agreement with the elemental analysis showing some As excess as compared to Ga (Table 4.1). The details for the first shell fit for GaAs NCs are shown in Figure 4.16 and the results of the fit are summarized in Table 4.2.

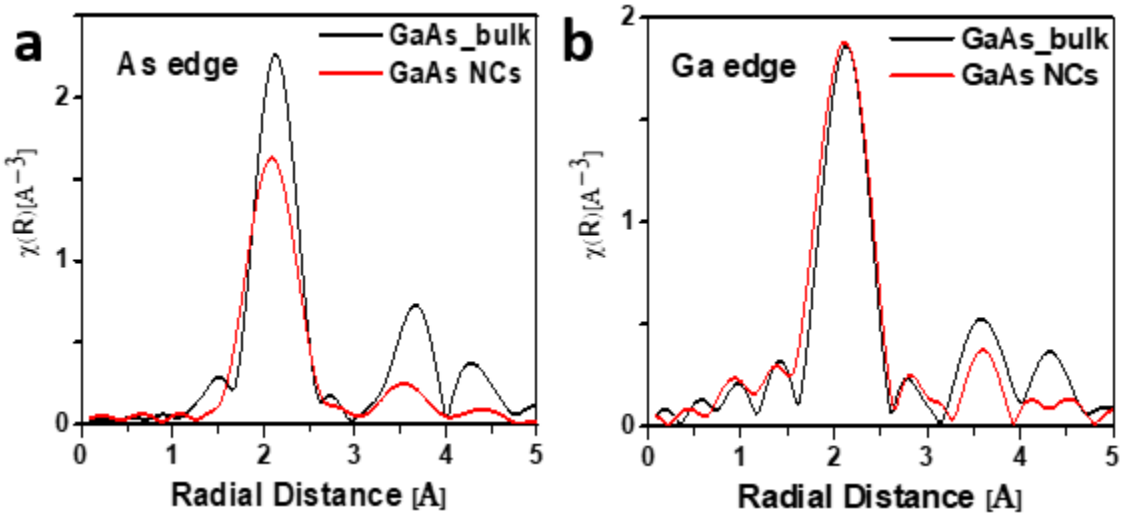

Figure 4.15 EXAFS studies on ~5 nm GaAs NCs. Comparison of Magnitude of Fourier transforms of k^2 -weighted (a) As K-edge EXAFS and (b) Ga K-edge EXAFS measured for GaAs powder (black) and NCs (red).

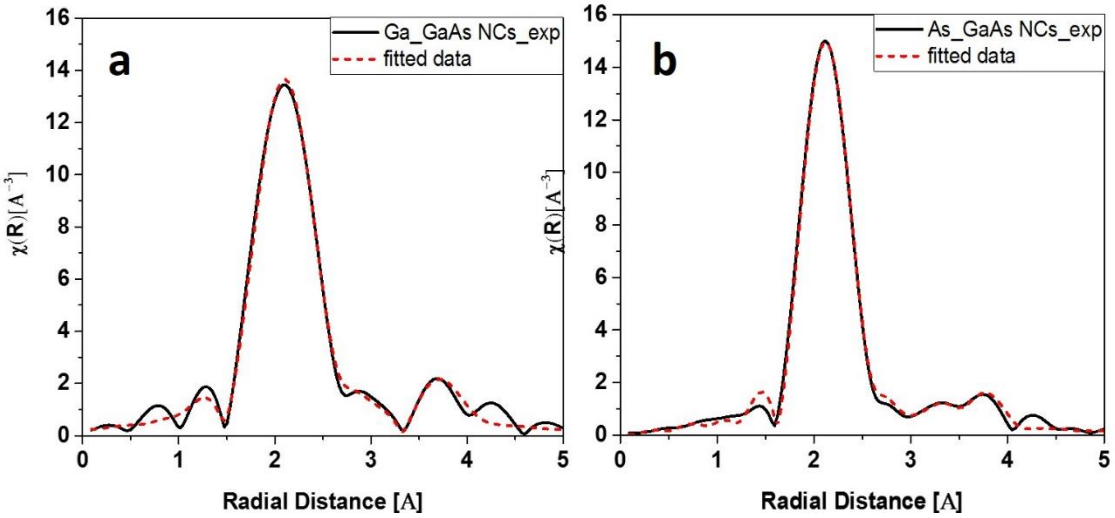

Figure 4.16 Fitting of EXAFS data used to determine coordination number and bond lengths for Ga- and As-edges. Magnitude of the Fourier transformed EXAFS and fits for (a) Ga edge and (b) As edge for GaAs NCs. Experimental data is shown in black and the corresponding fit is shown in red.

Edge	Sample Name	Paths	Bond length R (ang)	Coordination Number (n)	Debye Waller Factor	Energy Shift ΔE (eV)
As edge S_o^2=1.02	GaAs - tol R=1.0-4.0 Å k= 3.0-12.0 $Å^{-1}$	As-Ga	2.45 ± 0.02	3.6 ± 0.4	0.005 ± 0.001	1.3 ± 1.1
		As-As	4.00 ± 0.03	12	0.06 ± 0.01	
Ga edge S_o^2=1.1	GaAs - tol R=1.2-4.0 Å k= 3.0-10.5 $Å^{-1}$	Ga-As	2.45 ± 0.01	4.3 ± 0.5	0.007 ± 0.001	1.3 ± 1.2
		Ga-Ga	4.00 ± 0.03	12	0.01 ± 0.01	

Table 4.2: List of parameters obtained from the data modeling for As and Ga edges shown in Figure S12. The parameters with error bars are variables and the ones without error bars have been set to that obtained from the theoretical calculations using FEFF6

4.6.3 EPR Spectroscopy shows Ga vacancies

Electron paramagnetic resonance (EPR) has been employed as a sensitive probe for the identification of paramagnetic point defects in bulk semiconductors and NCs.[52-53] Low temperature (~4K) EPR signal from as-synthesized GaAs NCs consists of a quartet spectrum (g =2.094) with a hyperfine splitting of 190 G superimposed on an unresolved spectrum with the g tensor of 2.056 (Figure 4.17). The quartet signal indicates that the splitting comes from an atom with nuclear spin of 3/2. Both Ga and As have nuclear spin 3/2 and could lead to such spectrum, however, when the spin density is localized on either of these nuclei, much larger hyperfine splitting (interstitial Ga ~640G, As_{Ga} antisite ~860G) is expected. The relatively low hyperfine splitting of 190 G suggests that the spin density is localized on the vacancy. While As atoms contain one I=3/2 isotope, ^{75}As, with 100% natural abundancy, Ga atoms have two non-equivalent isotopes with I=3/2, ^{69}Ga and

^{71}Ga, with 60% and 40% natural abundancy, respectively, with different hyperfine and g tensors. Therefore, we would expect that the vacancy observed as defect in as-synthesized GaAs NCs is surrounded by equivalent As atoms that are equally contributing to the hyperfine splitting of 190G. Indeed, similar hyperfine splitting and g tensors were obtained previously in electron irradiated bulk GaAs and were attributed to Ga vacancy defects.[53]

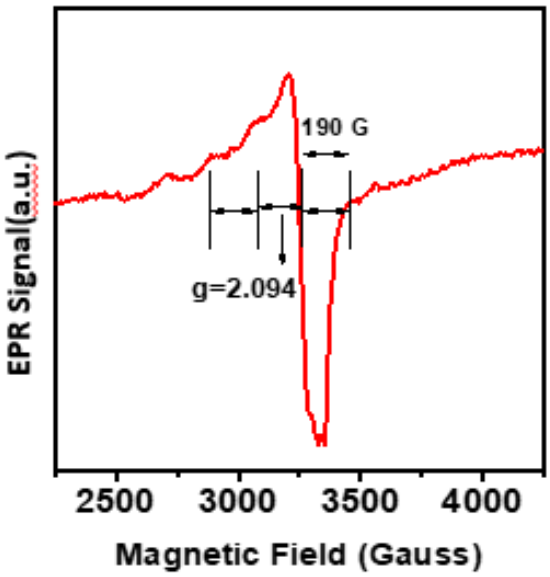

Figure 4.17 X-band EPR spectrum of ~ 5 nm GaAs NCs collected at 4K temperature. The microwave power was 0.1 mW and the modulation amplitude was 10 G.

4.7 Conclusions

In summary, we have shown that crystalline colloidal GaAs particles can be accessed by several colloidal routes. Somewhat unusual surface treatments are needed to obtain colloidal solutions of surface passivated and phase-pure GaAs NCs. Our EXAFS, Raman and EPR studies indicate that the covalent lattice of GaAs is prone to structural defects like Ga vacancies which are not usually found in more ionic semiconductor nanocrystals. Our results point out to a fundamental limitation of solvents and reactants used for traditional colloidal synthesis of GaAs NCs. It appears

that defects annealing in GaAs NCs requires higher temperatures than common solvents and ligands could allow. To address this fundamental issue, we need solvents which can be employed for colloidal chemistry at higher temperatures for the processing of strongly covalent nanomaterials. This issue is the subject matter of the next chapter.

4.8 References

1. Adachi, S., *Properties of semiconductor alloys: group-IV, III-V and II-VI semiconductors*. John Wiley & Sons: 2009; Vol. 28.
2. Yablonovitch, E.; Miller, O. D.; Kurtz, S. R. In *The opto-electronic physics that broke the efficiency limit in solar cells*, Photovoltaic Specialists Conference (PVSC), 2012 38th IEEE, 3-8 June 2012; 2012; pp 001556-001559.
3. DiLorenzo, J. V.; Khandelwal, D. D., GaAs FET principles and technology. *Dedham, MA, Artech House, Inc., 1982. 787 p* **1982,** *1*.
4. Hall, R. N.; Fenner, G. E.; Kingsley, J. D.; Soltys, T. J.; Carlson, R. O., Coherent Light Emission From GaAs Junctions. *Phys. Rev. Lett.* **1962,** *9* (9), 366-368.
5. Brus, L. E., Electron–electron and electron-hole interactions in small semiconductor crystallites: The size dependence of the lowest excited electronic state. *J. Chem. Phys.* **1984,** *80* (9), 4403-4409.
6. Nozik, A. J.; Mićić, O. I., Colloidal Quantum Dots of III-V Semiconductors. *MRS Bull.* **1998,** *23* (02), 24-30.
7. Micic, O. I.; Curtis, C. J.; Jones, K. M.; Sprague, J. R.; Nozik, A. J., Synthesis and Characterization of InP Quantum Dots. *J.Phys.Chem.* **1994,** *98* (19), 4966-4969.
8. Tessier, M. D.; Dupont, D.; De Nolf, K.; De Roo, J.; Hens, Z., Economic and Size-Tunable Synthesis of InP/ZnE (E = S, Se) Colloidal Quantum Dots. *Chemistry of Materials* **2015,** *27* (13), 4893-4898.
9. Song, W.-S.; Lee, H.-S.; Lee, J. C.; Jang, D. S.; Choi, Y.; Choi, M.; Yang, H., Amine-derived synthetic approach to color-tunable InP/ZnS quantum dots with high fluorescent qualities. *Journal of nanoparticle research* **2013,** *15* (6), 1-10.
10. Battaglia, D.; Peng, X., Formation of High Quality InP and InAs Nanocrystals in a Noncoordinating Solvent. *Nano. Lett.* **2002,** *2* (9), 1027-1030.
11. Guzelian, A.; Banin, U.; Kadavanich, A.; Peng, X.; Alivisatos, A., Colloidal chemical synthesis and characterization of InAs nanocrystal quantum dots. *Appl. Phys. Lett* **1996,** *69* (10), 1432-1434.
12. Srivastava, V.; Janke, E. M.; Diroll, B. T.; Schaller, R. D.; Talapin, D. V., Facile, Economic and Size-Tunable Synthesis of Metal Arsenide Nanocrystals. *Chem. Mater.* **2016,** *28* (18), 6797-6802.
13. Liu, W.; Chang, A. Y.; Schaller, R. D.; Talapin, D. V., Colloidal InSb Nanocrystals. *Journal of the American Chemical Society* **2012,** *134* (50), 20258-20261.
14. Yarema, M.; Kovalenko, M. V., Colloidal Synthesis of InSb Nanocrystals with Controlled Polymorphism Using Indium and Antimony Amides. *Chemistry of Materials* **2013,** *25* (9), 1788-1792.

15. Beberwyck, B. J.; Alivisatos, A. P., Ion Exchange Synthesis of III–V Nanocrystals. *J.Am.Chem.Soc.* **2012,** *134* (49), 19977-19980.
16. Butler, L.; Redmond, G.; Fitzmaurice, D., Preparation and spectroscopic characterization of highly confined nanocrystallites of gallium arsenide in decane. *J.Phys.Chem.* **1993,** *97* (41), 10750-10755.
17. BYRNE, E. K.; PARKANYI, L.; THEOPOLD, K. H., Design of a Monomeric Arsinogallane and Chemical Conversion to Gallium Arsenide. *Science* **1988,** *241* (4863), 332-334.
18. Kher, S. S.; Wells, R. L., Synthesis and characterization of colloidal nanocrystals of capped gallium arsenide. *Nanostruct Mater* **1996,** *7* (6), 591-603.
19. Lauth, J.; Strupeit, T.; Kornowski, A.; Weller, H., A Transmetalation Route for Colloidal GaAs Nanocrystals and Additional III–V Semiconductor Materials. *Chem. Mater.* **2013,** *25* (8), 1377-1383.
20. Malik, M. A.; O'Brien, P.; Norager, S.; Smith, J., Gallium arsenide nanoparticles: synthesis and characterisation. *J.Mater.Chem.* **2003,** *13* (10), 2591-2595.
21. Olshavsky, M. A.; Goldstein, A. N.; Alivisatos, A. P., Organometallic synthesis of gallium-arsenide crystallites, exhibiting quantum confinement. *J.Am.Chem.Soc.* **1990,** *112* (25), 9438-9439.
22. Uchida, H.; Curtis, C. J.; Kamat, P. V.; Jones, K. M.; Nozik, A. J., Optical properties of gallium arsenide nanocrystals. *J.Phys.Chem.* **1992,** *96* (3), 1156-1160.
23. Park, J. P.; Lee, J. J.; Kim, S. W., Fabrication of GaAs, InxGa1-xAs and Their ZnSe Core/Shell Colloidal Quantum Dots. *J Am Chem Soc* **2016,** *138* (51), 16568-16571.
24. Wells, R. L.; Pitt, C. G.; McPhail, A. T.; Purdy, A. P.; Shafieezad, S.; Hallock, R. B., The use of tris(trimethylsilyl)arsine to prepare gallium arsenide and indium arsenide. *Chemistry of Materials* **1989,** *1* (1), 4-6.
25. R. Heath, J., Covalency in semiconductor quantum dots. *Chem. Soc. Rev* **1998,** *27* (1), 65-71.
26. Eisch, J. J., Organometallic Compounds of Group III. II. the Reaction of Gallium Alkyls and Alkyl Hydrides with Unsaturated Hydrocarbons. *J.Am.Chem.Soc.* **1962,** *84* (20), 3830-3836.
27. Jones, A. C., Developments in metalorganic precursors for semiconductor growth from the vapour phase. *Chem. Soc. Rev* **1997,** *26* (2), 101-110.
28. Gupta, S.; Whitaker, J. F.; Mourou, G. A., Ultrafast carrier dynamics in III-V semiconductors grown by molecular-beam epitaxy at very low substrate temperatures. *Quantum Electronics, IEEE Journal of* **1992,** *28* (10), 2464-2472.
29. Gant, T. A.; Shen, H.; Flemish, J. R.; Fotiadis, L.; Dutta, M., Raman study of low growth temperature GaAs. *Appl. Phys. Lett* **1992,** *60* (12), 1453-1455.
30. Harmon, E.; Melloch, M.; Woodall, J.; Nolte, D.; Otsuka, N.; Chang, C., Carrier lifetime versus anneal in low temperature growth GaAs. *Appl. Phys. Lett* **1993,** *63* (16), 2248-2250.
31. Kaminska, M.; Weber, E.; Liliental-Weber, Z.; Leon, R.; Rek, Z., Stoichiometry-related defects in GaAs grown by molecular-beam epitaxy at low temperatures. *J. Vac. Sci. Tech.* **1989,** *7* (4), 710-713.
32. Uchida, H.; Curtis, C. J.; Nozik, A. J., Gallium arsenide nanocrystals prepared in quinoline. *J.Phys.Chem.* **1991,** *95* (14), 5382-5384.
33. Luo, J.-W.; Franceschetti, A.; Zunger, A., Quantum-size-induced electronic transitions in quantum dots: Indirect band-gap GaAs. *Phys. Rev. B* **2008,** *78* (3), 035306.

34. Cao; Banin, U., Growth and Properties of Semiconductor Core/Shell Nanocrystals with InAs Cores. *J.Am.Chem.Soc.* **2000,** *122* (40), 9692-9702.
35. Harris, D. K.; Allen, P. M.; Han, H.-S.; Walker, B. J.; Lee, J.; Bawendi, M. G., Synthesis of cadmium arsenide quantum dots luminescent in the infrared. *J.Am.Chem.Soc.* **2011,** *133* (13), 4676-4679.
36. Downs, A. J., *Chemistry of aluminium, gallium, indium and thallium*. Springer Science & Business Media: 1993.
37. Jäkle, F., Lewis acidic organoboron polymers. *Coord. Chem.Rev.* **2006,** *250* (9), 1107-1121.
38. Traub, M. C.; Biteen, J. S.; Brunschwig, B. S.; Lewis, N. S., Passivation of GaAs Nanocrystals by Chemical Functionalization. *J.Am.Chem.Soc.* **2008,** *130* (3), 955-964.
39. Sandroff, C. J.; Hegde, M. S.; Farrow, L. A.; Chang, C. C.; Harbison, J. P., Electronic passivation of GaAs surfaces through the formation of arsenic—sulfur bonds. *Appl. Phys. Lett* **1989,** *54* (4), 362-364.
40. Jia-Fa, F.; Haruhiro, O.; Yasuo, N., The Effect of (NH 4) 2 S Treatment on the Interface Characteristics of GaAs MIS Structures. *Jap. J. App. Phys* **1988,** *27* (7A), L1331.
41. Mariani, G.; Laghumavarapu, R. B.; Tremolet de Villers, B.; Shapiro, J.; Senanayake, P.; Lin, A.; Schwartz, B. J.; Huffaker, D. L., Hybrid conjugated polymer solar cells using patterned GaAs nanopillars. *Appl. Phys. Lett* **2010,** *97* (1), 013107.
42. Nag, A.; Kovalenko, M. V.; Lee, J.-S.; Liu, W.; Spokoyny, B.; Talapin, D. V., Metal-free Inorganic Ligands for Colloidal Nanocrystals: S2–, HS–, Se2–, HSe–, Te2–, HTe–, TeS32–, OH–, and NH2– as Surface Ligands. *J.Am.Chem.Soc.* **2011,** *133* (27), 10612-10620.
43. Rossetti, R.; Nakahara, S.; Brus, L. E., Quantum size effects in the redox potentials, resonance Raman spectra, and electronic spectra of CdS crystallites in aqueous solution. *J. Chem. Phys.* **1983,** *79* (2), 1086-1088.
44. Alivisatos, A. P., Perspectives on the Physical Chemistry of Semiconductor Nanocrystals. *J.Phys.Chem.* **1996,** *100* (31), 13226-13239.
45. Adam, S.; Talapin, D. V.; Borchert, H.; Lobo, A.; McGinley, C.; de Castro, A. R. B.; Haase, M.; Weller, H.; Möller, T., The effect of nanocrystal surface structure on the luminescence properties: Photoemission study of HF-etched InP nanocrystals. *J. Chem. Phys.* **2005,** *123* (8), 084706.
46. Klimov, V. I., Optical Nonlinearities and Ultrafast Carrier Dynamics in Semiconductor Nanocrystals. *J. Phys. Chem. B* **2000,** *104* (26), 6112-6123.
47. Beard, M. C.; Knutsen, K. P.; Yu, P.; Luther, J. M.; Song, Q.; Metzger, W. K.; Ellingson, R. J.; Nozik, A. J., Multiple Exciton Generation in Colloidal Silicon Nanocrystals. *Nano. Lett.* **2007,** *7* (8), 2506-2512.
48. Zardo, I.; Conesa-Boj, S.; Peiro, F.; Morante, J. R.; Arbiol, J.; Uccelli, E.; Abstreiter, G.; Fontcuberta i Morral, A., Raman spectroscopy of wurtzite and zinc-blende GaAs nanowires: Polarization dependence, selection rules, and strain effects. *Phys. Rev. B* **2009,** *80* (24), 245324.
49. Sharma, R. P.; Bhadra, R.; Rehn, L. E.; Baldo, P. M.; Grimsditch, M., Crystalline to amorphous transformation in GaAs during Kr ion bombardment: A study of elastic behavior. *J. Appl. Phys.* **1989,** *66* (1), 152-155.
50. Seong, M.; Mićić, O. I.; Nozik, A.; Mascarenhas, A.; Cheong, H. M., Size-dependent Raman study of InP quantum dots. *Appl. Phys. Lett* **2003,** *82* (2), 185-187.
51. Takagahara, T., Electron-phonon interactions in semiconductor quantum dots. *Semiconductor quantum dots. Springer, Berlin* **2002**, 115-147.

52. Mićić, O. I.; Nozik, A. J.; Lifshitz, E.; Rajh, T.; Poluektov, O. G.; Thurnauer, M. C., Electron and Hole Adducts Formed in Illuminated InP Colloidal Quantum Dots Studied by Electron Paramagnetic Resonance. *J. Phys. Chem. B* **2002,** *106* (17), 4390-4395.
53. Jia, Y.; Von Bardeleben, H.; Stievenard, D.; Delerue, C., Electron-paramagnetic-resonance observation of gallium vacancy in electron-irradiated p-type GaAs. *Phys. Rev. B* **1992,** *45* (4), 1645.

Chapter 5.

Molten salts as solvents for the processing of Colloidal Nanomaterials.

5.1 Introduction

Molten salts have recently emerged as an attractive class of solvents for the synthesis and processing of nanomaterials due to their unique properties such as high temperature stability, wide electrochemical window and transparency in a large part of the electromagnetic spectrum.[1-2] Traditionally, synthesis of colloidal nanomaterials has been carried out in either aqueous solution or organic media. The field has matured in the past two decades and a variety of nanomaterials such as II-VI quantum dots[3], oxides[4] and metal NPs[5] can be routinely synthesized in a very precise manner. However, synthesis in organic media is ultimately limited to temperatures below 400°C at which most organic solvents either evaporate or decompose. In this regard further development of synthetic approaches of NCs with strong covalent bonds requires solvents with boiling temperatures well above 400°C. Inorganic salts have long been explored as matrices for dispersion of nanocrystals for their high temperature processing.[2] There have been several reports on the synthesis of nanomaterials with a very strong covalent bonding framework in molten halide eutectics.[6-8] However such processes typically have no control over the phase, shape and size homogeneity of the resulting nanostructure. One important factor to be considered in this regard is the colloidal state of nanomaterials in these non-traditional solvents. A colloidal state of nanoparticles in polar media is achieved through the electrostatic stabilization of the nanoparticle surface using charged surface groups which repel the nanoparticles away from each other (Figure 5.1a). Similarly in a non-polar media the van der Waals attraction is overcome by decorating the nanoparticles with hairy long chain surfactant molecules that impart them colloidal stability (Figure 5.1a). Talapin Group recently reported that a wide range of nanomaterials can be dispersed

in inorganic molten salts and ionic liquids where neither of these traditional mechanisms of colloidal stabilization apply.[1] A correlation between colloidal stability and chemical interaction between the NC surface and molten salt ions could be established by screening a variety of molten salt and NC combinations. It was predicted theoretically that these chemical interactions in turn lead to overall repulsive solvation interactions which allow the NPs to stay separated from each other despite electrostatic repulsion being screened at a distance of 1-2 Å (Figure 5.1b). Similar arguments could also be applied to explain the stability of surfactant free inorganic nanoparticles in hydrophilic ionic liquids such as BMIM+X-. However, other mechanisms have also been proposed to explain the stability of nanoparticles in organic ionic liquids. The Debye screening length can be on the order of 10 nm in ionic liquids due to their low dissociation ability, hence, electrical double layer interaction can still be the dominant factor responsible for the overall repulsive potential. [9-10]

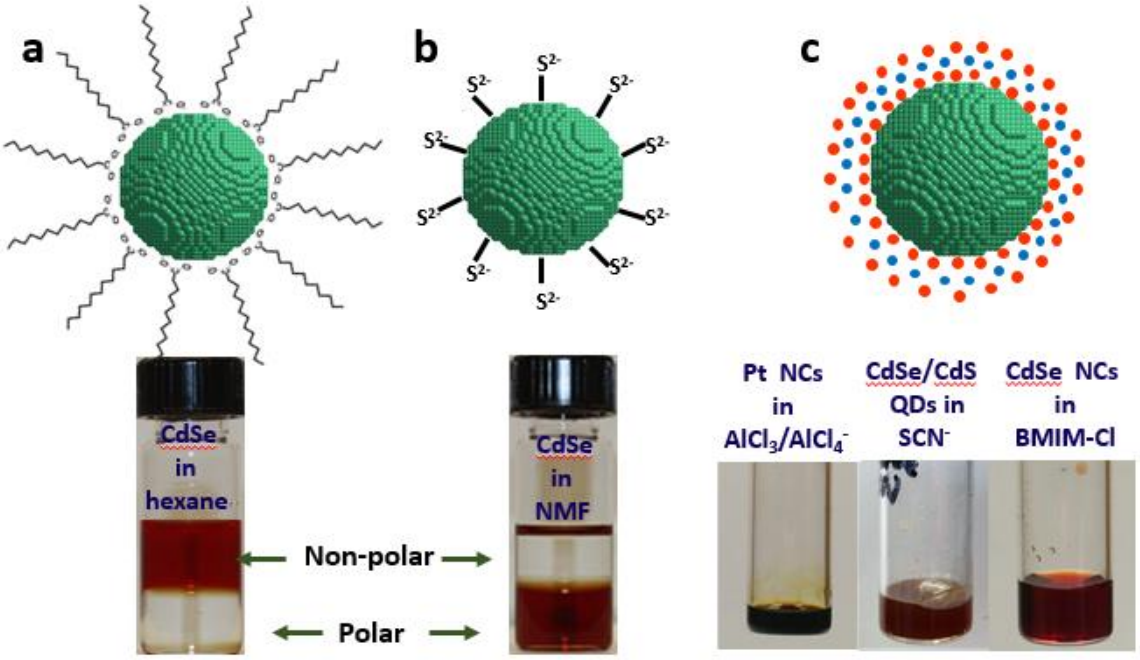

Figure 5.1. Mechanisms responsible for colloidal stability (a) steric, (b) electrostatic and (c) solvent restructuring. Colloidal dispersions of Pt NCs in $AlCl_3$:NaCl:KCl molten salt eutectic, CdSe/CdS core shell QDs in KSCN:NaSCN molten salt eutectic and CdSe NCs in BMIM-Cl are shown in panel (c).

The solvation interactions between macroscopic surfaces have been investigated with surface forces apparatus for simple non-polar liquids[11] and ionic liquids.[10, 12-13] The oscillatory forces observed at distances on the order of the ionic sizes were linked to the re-structuring of the bulk liquids. Experimentally, structural changes of ionic solvents next to flat surfaces have been verified by techniques like X-ray reflectivity[14], angle-resolved XPS[15] and sum-frequency generation spectroscopy.[16] However, such surface sensitive techniques are not appropriate for studying colloidal solutions of NCs. Recently X-ray pair distribution function (PDF) analysis has been successfully applied to study re-organization of molecular solvents around colloidal particles and ionic liquids confined inside carbon nanopores.[17-18]

In this chapter, I will present detailed studies on the phenomenology, mechanism and application of nanocrystal colloids in molten salt eutectics. Small Angle X-ray scattering results describe the state of NC dispersions in molten salts. I will also present the case of III-V NCs in different molten salt and ionic liquid media. FTIR, XPS and PDF studies are carried out to gain a deeper understanding about the mechanisms underlying the stability of NCs in molten salts and Ionic liquids. And finally a few examples about the potential unique applications of these systems are discussed.

5.2 Choice of Molten salts and Ionic liquids and their NC dispersions

As described in Reference 1, a molten salt formulation with a pronounced Lewis acidic or Lewis basic character can be used to stabilize nanocrystals of metals, oxides and semiconductors. A complete list of nanocrystals and molten salt (and ionic liquids) combinations shown in this work are given in Table 5.1. The general experimental details of preparation of these are left out here for sake of brevity. Specific details will be provided in Chapter 6 and Chapter 7. Interested reader is referred to Reference 1 for general details.

Eutectic Composition (% mol)	Melting Temperature	QDs dispersed
$AlCl_3$:NaCl:KCl 63.5:20:16.5	90°C	Pt, InP, CdSe/CdS
BMIM+X^- ($X=Cl^-/Br^-/I^-$)	73°C/65°C/r.t.	CdSe,InAs
CsBr:LiBr:KBr = 25:56.1:18.9	236°C	InP,InAs
KSCN:NaSCN = 73.7:26.3	140°C	Pt, CdSe/CdS, InP, InAs
$ZnCl_2$:NaCl:KCl = 60:20:20	203°C	InP

Table 5.1. Molten Salt and NC combinations discussed in this chapter

For SAXS and PDF studies shown in this chapter, molten eutectics of $AlCl_3$/NaCl/KCl ($AlCl_3/AlCl_4^-$) and NaSCN/KSCN (SCN^-) were chosen as representatives of salts with Lewis acidic and Lewis basic character respectively. We also studied NC dispersions in $BMIM^+X^-$ ionic liquids which represent the organic analog of inorganic molten salts. These choices were motivated due to multiple reasons including (1) The melting points of these salts are low (97°C for $AlCl_3/AlCl_4^-$ and 140°C for SCN^- and ~ 60°C for BMIM-Cl) which permit easy handling and less demanding experimental conditions; (2) these salts do not contain heavy elements which permit sufficient transmission of X-rays for simultaneous SAXS and PDF experiments; and (3) halides, halometallates and SCN ions are all known to bind to NCs' surfaces[19-21]. Representative photographs of NC dispersions in these solvents is shown in Figure 5.1c.

III-V NCs could also be dispersed in a variety of molten salts and ionic liquids as shown in Table 5.1. NCs were stable in all the molten salt eutectics except $AlCl_3$:KCl:NaCl where etching of the nanocrystals was observed. For the chemical manipulation of III-V NCs at high temperature, the

CsBr:LiBr:KBr eutectic was chosen due to its high temperature stability, low vapor pressure, high solubility of group III halides and inertness to side reactions. Chapters 6 and & 7 show examples of chemical transformations possible in III-V QDs at high temperatures. Pictures of InP and InAs QDs in different molten salts are shown in Figure 5.2

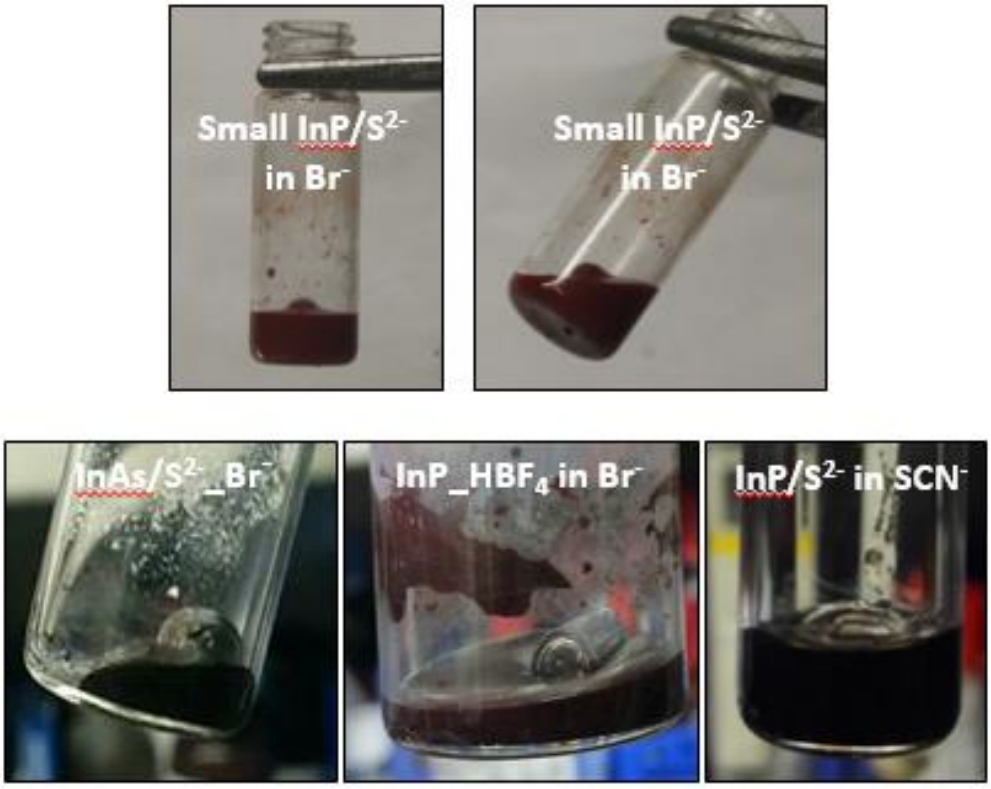

Figure 5.2. Photographs of InP and InAs QDs in different molten salts.

5.3 SAXS studies on NCs in molten salts and Ionic liquids.

We first characterized the NC dispersions in molten salts using SAXS to gain more information about the stability of these dispersions. Representative SAXS curves of Pt NCs in molten $AlCl_3/AlCl_4$ are shown in Figure 5.3. The SAXS curves for the same Pt NCs in toluene is shown for comparison. For spherical particles the SAXS scattering intensity (I(q)) is a product of

two terms, the form factor (F(q)) and structure factor, S(q), $I(q) = |F(q)|^2 S(q)$. S(q)=1 for Pt NCs in molten $AlCl_3/AlCl_4^-$ meaning that the scattering is due to the form factor only (dilute limit) and particles do not interact with each other. The volume size distributions extracted for the two curves nearly coincide meaning that there was no ripening of Pt NCs (Figure 5.3). In contrast the same sample in solid $AlCl_3/AlCl_4^-$ matrix has S(q)≠1 meaning that particles are pushed by the solidification fronts close enough for them to interfere (Figure 5.4).

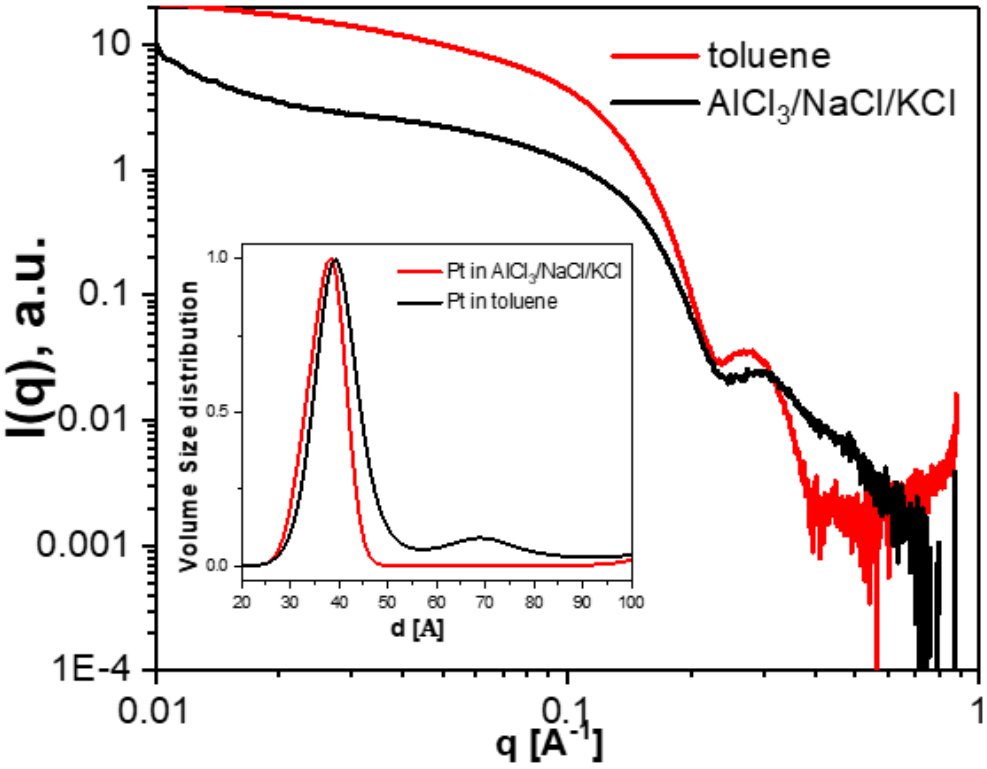

Figure 5.3. SAXS curves for Pt NCs in $AlCl_3/AlCl_4^-$ eutectic and comparison to the same NCs dispersed in toluene. Inset shows the comparison of the size distributions of Pt NCs dispersed in toluene and $AlCl_3/AlCl_4^-$ extracted from the respective fits.

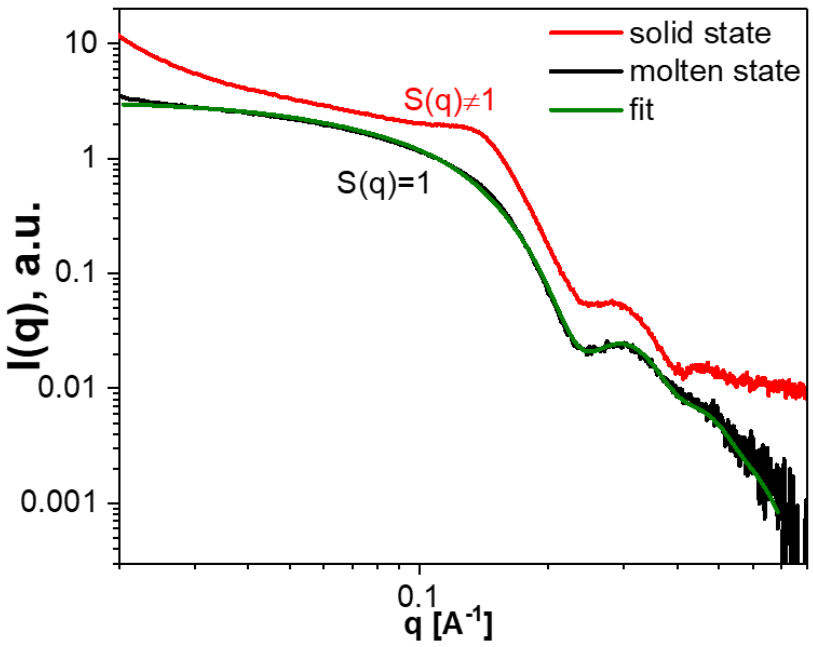

Figure 5.4. SAXS curves for Pt NCs in solid and molten $AlCl_3/AlCl_4^-$. Particles in the solid matrix are close to each other resulting in S(q)≠1 whereas particles in the molten matrix form a non-interacting colloidal solution with S(q)=1.

Qualitatively similar behaviour was seen for bare CdSe/CdS QDs dispersed in SCN^- eutectic. NCs can also form non-precipitating colloidal solutions in SCN^- eutectic. CdSe/CdS core shells were chosen for these experiments due to their higher stability at temperatures above 200 C and also due to their strong affinity to SCN^- ions. Figure 5.5 shows a representative SAXS curve of bare QDs in SCN^- molten salt. In this case the primary particles of QDs interact with each other resulting in S(q)≠1. Also I(q) for $q<4*10^{-2}$ $Å^{-1}$ rises with the slope of -1.5. This suggests that QDs are clustered into fractal like aggregates whose dimension can be inferred from the Porod slope.[22] The slope of -1.5 corresponds to the fractal dimension of 1.5 which is below 2 thus suggesting diffusion limited cluster aggregation of QDs with the formation of open chain-like secondary structures.[23] Although in this case QDs do interact in SCN^- melt, I(q) for $q>4*10^{-2}$ $Å^{-1}$ still has similar Bessel function oscillations with the Porod slope of -4 as QDs dispersed in toluene

suggesting preservation of the average size and spherical shape (Figure 5.5). This observation suggests that NCs are not touching directly and there is a kinetic barrier preventing further approach of QDs. Similar behavior has been observed for uniformly dispersed Iron Oxide nanoparticles in polymer nanocomposites.[24] NCs processed at high temperature in molten salts show markedly different behavior as compared to ligand free NCs heated up in the absence of molten salts. NCs dispersed in SCN melt and heated to 250 C could be recovered and re-dispersed in non-polar solvents such as hexane with the help of organic ligands while the same was not possible when bare NCs were heated at the same temperature without molten salts. This observation confirms that molten salts present a physical barrier for nanoparticles to interact with each other.

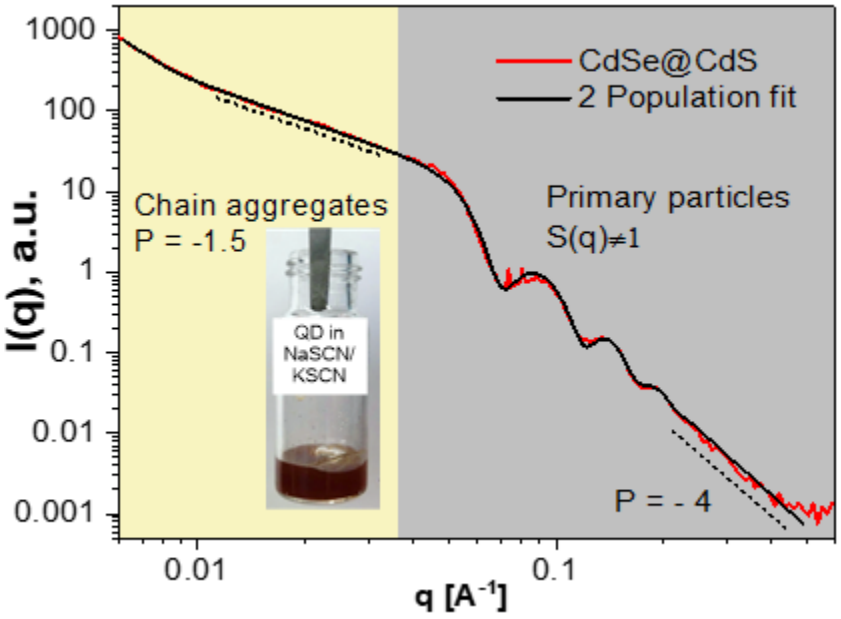

Figure 5.5. SAXS curves for CdSe/CdS in SCN^- eutectic. The inset shows a picture of CdSe/CdS QDs in the molten eutectic.

To further demonstrate this we heated a thin film of CdSe/CdS QDs at 250°C for 3h. The annealed film had markedly reduced Bessel function oscillations (Figure 5.6 a) due to

polydispersity of QDs with the standard deviation increasing from 8.3 % to 14 % after in-film annealing (Figure 5.6b). Moreover TEM image of these particles shows clear evidence of necking (particles fused with each other) while no such necking is observed for QDs recovered from molten SCN (See Figure 5.7). Metal nanoparticles such as Pt and Pd were also colloidally stable in SCN molten salt, however we observed some ripening of the particle size in these cases due to the corrosive effect of SCN^- ions at high processing temperatures (Figure 5.8). Interestingly, in the case of metal NPs in SCN^- melt NCs formed colloidal solutions with S(q) approaching unity whenever particles were capped with S^{2-} ligands rather than treated with $NOBF_4$ stripping agent (Figure 5.9). That could be related to S^{2-} acting as a buffer layer between noble metal surface and ions in the melt thus reducing the interfacial energy and increasing NCs' solubility.

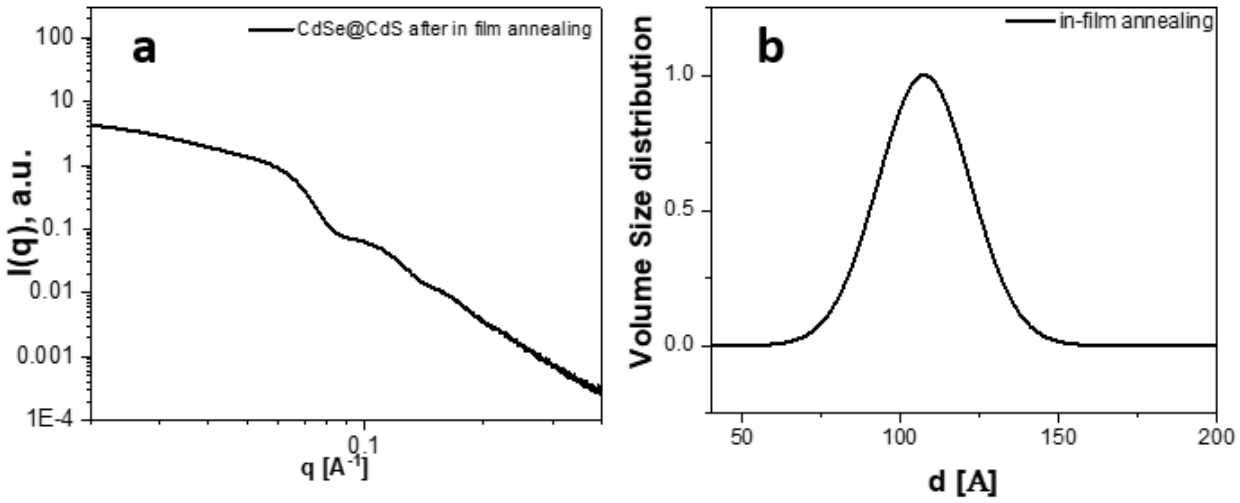

Figure 5.6. SAXS studies of QD films (a) SAXS curves of CdSe/CdS after in-film annealing. (b) the size distributions of CdSe/CdS after in-film annealing at 250°C for 24 h. The modelled polydispersity (assuming spherical shape with the aspect ratio of 1) is 14 % for in-film annealed sample as compared to 8.3% in molten SCN^- matrix.

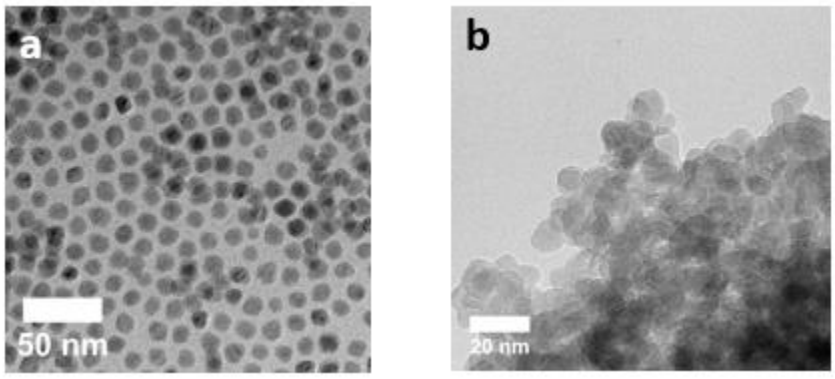

Figure 5.7. Change in morphology upon in-film annealing (a) TEM image of the initial CdSe/CdS NCs capped with organic ligands; (b) TEM image of CdSe/CdS NCs recovered after in-film annealing of bare NCs at 250°C for 24h.

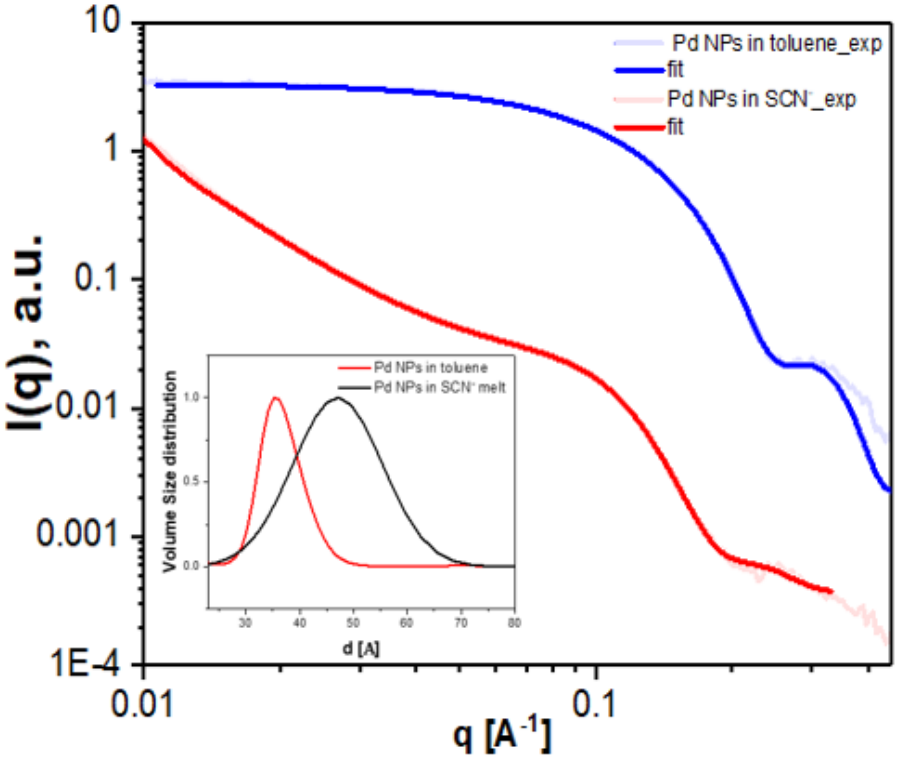

Figure 5.8. SAXS curves for the initial Pd NCs and the same Pd NCs dispersed in SCN^- melt; (inset) Comparison between the size distributions of the initial Pd NCs and Pd NCs in SCN^- melt showing significant broadening of the size distribution due to the ripening process.

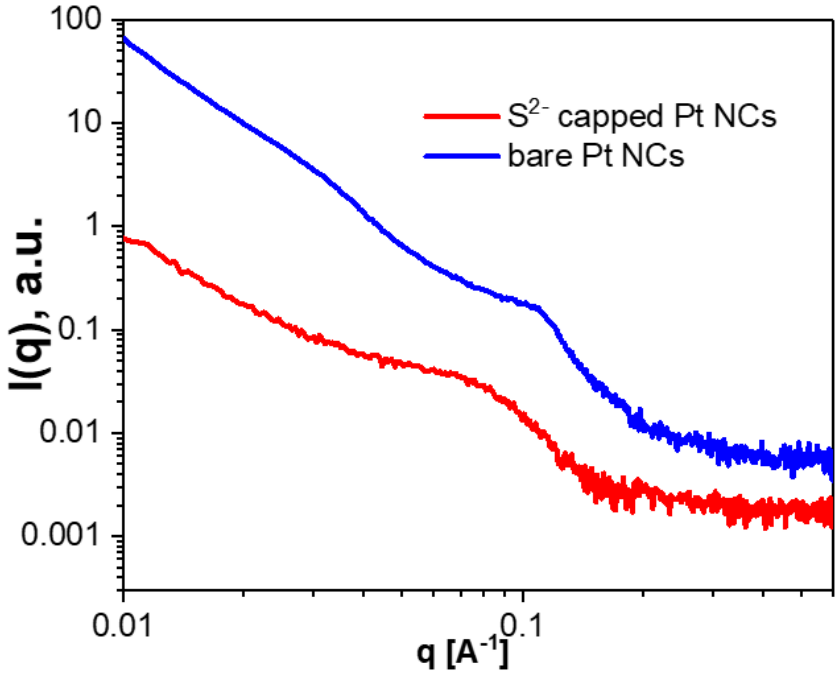

Figure 5.9. Comparison between S^{2-} capped and $NOBF_4$ treated (bare) Pt NCs in SCN^- where bare NCs exhibit a more pronounced structure factor with an evident peak at 0.11 $Å^{-1}$.

In addition to molten inorganic salts, SAXS measurements were carried out on NC dispesrsions in BMIM-X ionic liquids. SAXS spectrum of non-interacting InAs NCs in BMIM-Cl ILs is shown in Figure 5.10. The InAs NCs form stable non-interacting colloids in all three ionic liquids meaning that all three halide anions were capable of displacing native organic ligands with minimal damage to NC size and shape. The size distribution of NCs in the ILs is shown in the inset of Figure 5.10.

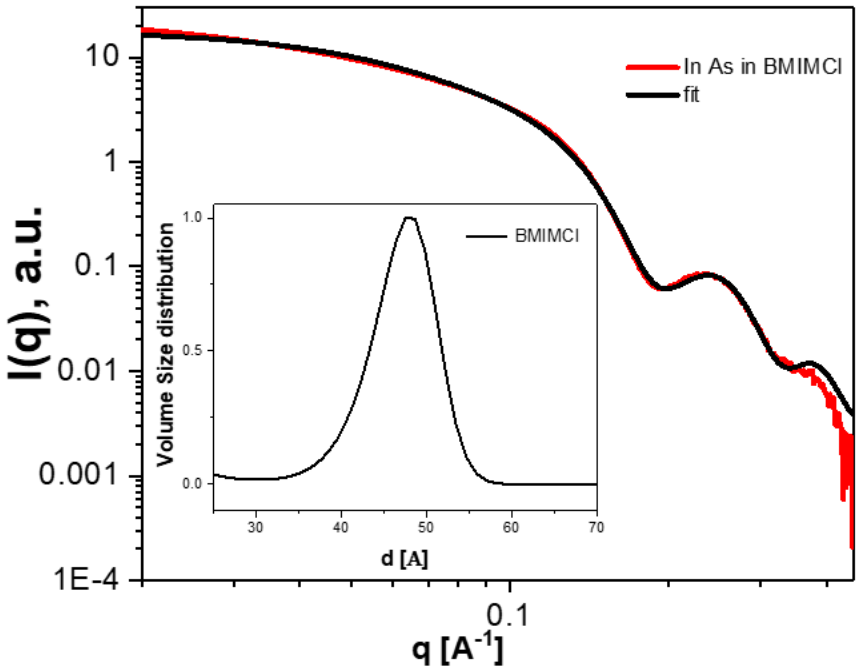

Figure 5.10. SAXS curve for InAs NCs in BMIM-Cl IL showing that particles form non-interacting colloids. Inset: size distribution extracted for InAs NCs in BMIM-Cl IL.

5.4 Chemical binding between nanocrystals and molten salts

Next, we sought to characterize the chemical nature of the interaction between the salts and the nanocrystals. The unique vibrational fingerprint of the SCN ion was used as an indicator for the nature of chemical bonding the SCN salt and the NC surface.[21] The NCs could be recovered from the salts by dissolving the salts in water or formamide repeatedly and centrifuging the NCs out. We measured FTIR spectra of NCs recovered from molten SCN eutectic and compared them to free SCN ions (Figure 5.11a). Free SCN ion shows a distinct feature corresponding to the CN stretch near ~ 2060 cm^{-1} while CdSe/CdS NCs recovered from the molten SCN showed a distinct feature at ~ 2090 cm^{-1}. This shift in the CN stretching frequency can be attributed to the binding of the SCN ion to the surface Cd atoms through sulfur. A larger shift to 2110 cm^{-1} was observed for SCN ions bound to Pt NCs showing the chemical specificity of the bonds.

Similar evidence of chemical bonding could also be observed for NCs dispersed in Ionic liquids, using XPS as the analytical tool. For these measurements we chose InAs NCs dispersed in BMIM-I as our sample of choice due to the substantial difference in the binding energy of In-I and In-As bonds. We compared the In 3d high resolution XPS spectra of organically capped InAs NCs with InAs NCs recovered from BMIM-I ionic liquids. InAs NCs recovered from BMIM-I showed a distinct contribution from In-I bonds whose peak is shifted by 1.1 eV indicating higher effective oxidation state of In bound with I than with As (Figure 5.11b).[25] These results unequivocally prove that highly specific chemical interactions exist between the nanocrystals surface and the molten salts which may be critical for the stability of these colloids.

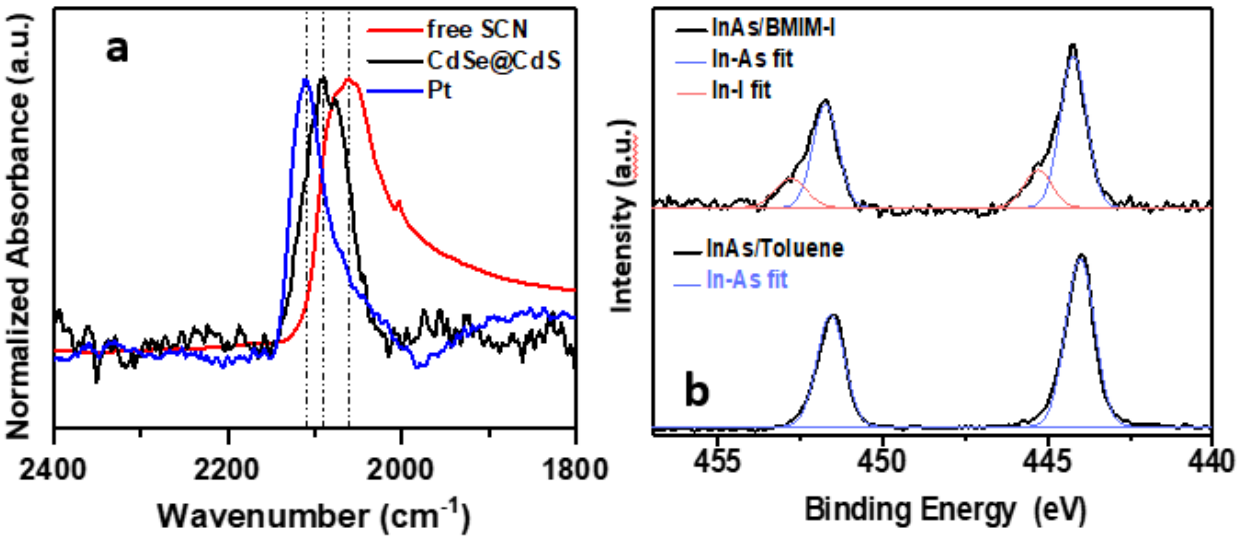

Figure 5.11. Chemical binding between NC surface and molten salts (a) FTIR spectra of Pt, CdSe/CdS NCs recovered from SCN^- melt in comparison with pure KSCN/NaSCN salt; (b) High resolution XPS spectra of In 3d region for the original InAs NCs and InAs NCs recovered from BMIM-I IL.

5.5 PDF Studies on Nanocrystals/Molten Salt dispersions

To better understand the effect of these chemical interactions on the local structure of the salts around the nanocrystals, we resorted to synchrotron based high energy X-ray Pair Distribution

Function (PDF) measurements. Pair distribution functions are extracted by the Fourier transform of the total scattering curves which give us information about both short range order (arrangement of atoms within molecules) and long range order (intermolecular arrangements) in a sample. Previously, re-structuring of molecular solvents such as propanol and water was measured experimentally around NPs using PDF analysis.[17] The compositional diversity in the $AlCl_3/AlCl_4^-$ eutectic due to the high vapor pressure of $AlCl_3$ and the presence of small amounts of $Al_2Cl_7^-$ and $Al_3Cl_{10}^-$ ions presented a hurdle in the interpretation of PDF data in these salts.[26] A variety of NCs dispersed in molten SCN^- eutectic and BMIM-X ionic liquids were studied with PDF analysis. In this chapter, we will focus on InP NCs dispersed in SCN eutectic as an example. A full research article based on these analyses is currently under preparation and interested readers are referred to it.

We obtained X-ray scattering data on the pure salt melt, QD powders without any solvent and finally on the QD/salt dispersions. To extract information about the solvent (restructured melt) around the nanocrystal surface, we first subtracted the total scattering of the pure melt from the QD/salt dispersions. The difference curve was further normalized by atomic form factors of the elements in the melt rendering the reduced structure factor (RSF) which contains element-independent structural information (Figure 5.12). The Fourier transform of the RSF curve (difference curve after subtracting the contribution from pure salt) gives us the difference-PDF (d-PDF). Further subtraction of the contribution from QD powders resulted in a double differential PDF (dd-PDF). Figure 5.13 shows PDF, d-PDF and dd-PDF results obtained for the case of InP QDs in SCN melt. The differential PDF of InP NPs in NaSCN/KSCN melt contains peaks corresponding to distances within InP QDs superimposed over long range damped sinusoidal oscillations (blue curve). The double differential PDF (dd-PDF) obtained from subtracting the PDF

of Pt NCs (blue curve) showed oscillations with distinct phase, amplitude and decay length than the original NaSCN/KSCN melt. These results clearly demonstrate the presence of a restructured solvent layer around the QD surface which prevents them from aggregating together at high temperatures.

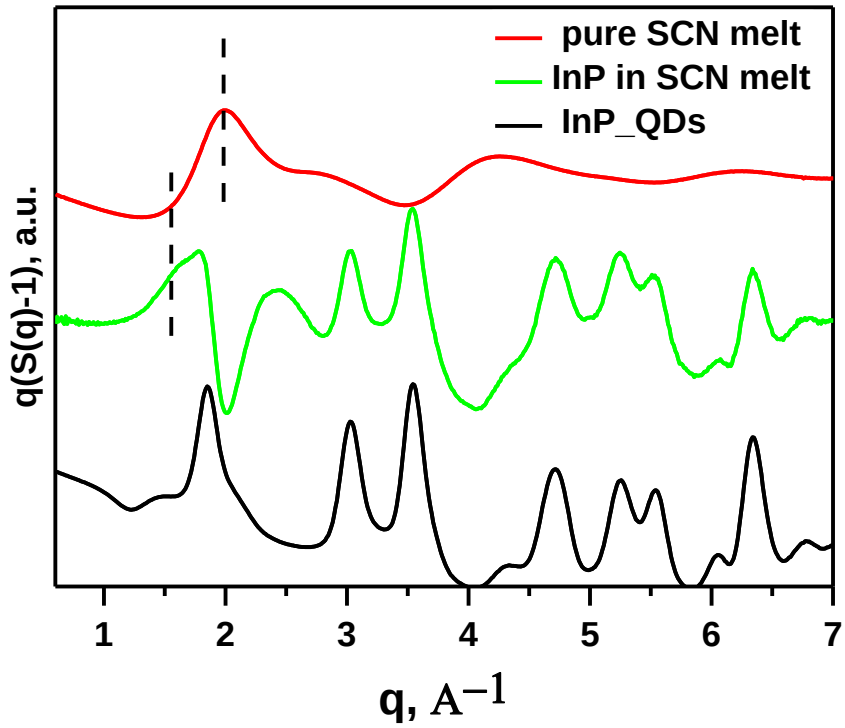

Figure 5.12. Comparison of reduced structure factors (RSF) of InP QDs in toluene and in SCN^- melt with RSF of the SCN^- (BMIM-Cl) without QDs. The RSF contains element-independent structural information. The first sharp diffraction peak (FSDP), pointed by black dashed lines, in the RSF curve is particularly informative in determining the changes in the local structure. We observed a significant shift in the FSDP in the RSF curves of QD/Salt composites as compared to pure salt.

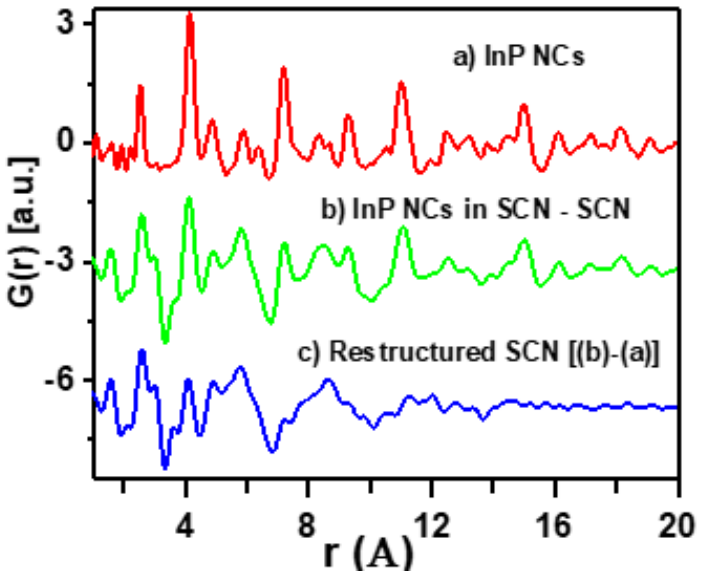

Figure 5.13. PDF studies on InP QDs in molten SCN^- melt. PDF [G(r)] extracted for InP QDs (red), dPDF calculated by subtracting the contribution of pure SCN melt from the InP QDs in SCN^- melt (green) and ddPDF generated by removing the contribution from InP QDs showing the G(r) corresponding to the restructured solvent (blue).

5.6 Conclusions and potential applications of NC dispersions in Molten Salts.

In conclusion, we present evidence of re-structuring of the solvent (salt ions) around the NCs through X-ray PDF analysis and show that this restructuring leads to the formation of non-aggregating colloidal dispersions of NCs in molten salts and ionic liquids as evidenced by SAXS measurements. The ability of salt ions to form chemical bonds with the surface of NCs results in the templating of salt ions around the NC surface preventing them from aggregating together. We believe that this new understanding about the colloidal stability of nanocrystals in completely ionized media of inorganic melts is unprecedented and opens up the possibility of the rational design of colloidal systems in these novel media.

The ability of sulfide ligands to impart colloidal stability to metal NPs in SCN eutectic is of huge significance in this new domain of NC/molten salt composites and introduces the concept of ligands for NC surfaces in molten salts. The ability to form stable colloidal solutions in molten salts with the help of ligands in an otherwise non-interacting system opens as up to an unlimited selection of molten salts which may not have the required lewis acidity or basicity such as nitrates but may be important for certain processes. This is an important direction of research in my belief.

Rational design of the colloidal state in these high temperature solvents can pave the way for the development of a variety of highly covalent structures in the nanocrystalline form. In the subsequent chapters, I will show examples of how molten salts can be used for the chemical manipulation of covalent III-V semiconductors and synthesis of new III-V compounds as well. These examples are the first ever efforts on processing of nanomaterials in molten salts without altering their morphology. We envision that with the development and deeper understanding of stability in molten salts and the concept of ligands, we can move towards complete synthesis of nanomaterials in molten salts at high pressures and temperatures which are otherwise inaccessible through traditional colloidal routes. This will be an active direction of research in the Talapin lab in the coming years.

5.7 References

1. Zhang, H.; Dasbiswas, K.; Ludwig, N. B.; Han, G.; Lee, B.; Vaikuntanathan, S.; Talapin, D. V., Stable colloids in molten inorganic salts. *Nature* **2017,** *542*, 328.
2. Liu, X.; Fechler, N.; Antonietti, M., Salt melt synthesis of ceramics, semiconductors and carbon nanostructures. *Chemical Society Reviews* **2013,** *42* (21), 8237-8265.
3. Murray, C. B.; Norris, D. J.; Bawendi, M. G., Synthesis and characterization of nearly monodisperse CdE (E = sulfur, selenium, tellurium) semiconductor nanocrystallites. *Journal of the American Chemical Society* **1993,** *115* (19), 8706-8715.
4. Park, J.; An, K.; Hwang, Y.; Park, J.-G.; Noh, H.-J.; Kim, J.-Y.; Park, J.-H.; Hwang, N.-M.; Hyeon, T., Ultra-large-scale syntheses of monodisperse nanocrystals. *Nature Materials* **2004,** *3*, 891.

5. Sun, S.; Murray, C. B.; Weller, D.; Folks, L.; Moser, A., Monodisperse FePt Nanoparticles and Ferromagnetic FePt Nanocrystal Superlattices. *Science* **2000,** *287* (5460), 1989-1992.
6. Liu, X.; Antonietti, M.; Giordano, C., Manipulation of Phase and Microstructure at Nanoscale for SiC in Molten Salt Synthesis. *Chemistry of Materials* **2013,** *25* (10), 2021-2027.
7. Portehault, D.; Devi, S.; Beaunier, P.; Gervais, C.; Giordano, C.; Sanchez, C.; Antonietti, M., A General Solution Route toward Metal Boride Nanocrystals. *Angewandte Chemie International Edition* **2011,** *50* (14), 3262-3265.
8. Estruga, M.; Girard, S. N.; Ding, Q.; Chen, L.; Li, X.; Jin, S., Facile and scalable synthesis of Ti5Si3 nanoparticles in molten salts for metal-matrix nanocomposites. *Chemical Communications* **2014,** *50* (12), 1454-1457.
9. Lee, A. A.; Perez-Martinez, C. S.; Smith, A. M.; Perkin, S., Scaling Analysis of the Screening Length in Concentrated Electrolytes. *Physical Review Letters* **2017,** *119* (2), 026002.
10. Gebbie, M. A.; Dobbs, H. A.; Valtiner, M.; Israelachvili, J. N., Long-range electrostatic screening in ionic liquids. *Proceedings of the National Academy of Sciences* **2015,** *112* (24), 7432-7437.
11. Horn, R. G.; Israelachvili, J. N., Direct measurement of structural forces between two surfaces in a nonpolar liquid. *The Journal of Chemical Physics* **1981,** *75* (3), 1400-1411.
12. Smith, A. M.; Lee, A. A.; Perkin, S., The Electrostatic Screening Length in Concentrated Electrolytes Increases with Concentration. *The Journal of Physical Chemistry Letters* **2016,** *7* (12), 2157-2163.
13. Gebbie, M. A.; Smith, A. M.; Dobbs, H. A.; Lee, A. A.; Warr, G. G.; Banquy, X.; Valtiner, M.; Rutland, M. W.; Israelachvili, J. N.; Perkin, S.; Atkin, R., Long range electrostatic forces in ionic liquids. *Chemical Communications* **2017,** *53* (7), 1214-1224.
14. Mezger, M.; Schröder, H.; Reichert, H.; Schramm, S.; Okasinski, J. S.; Schöder, S.; Honkimäki, V.; Deutsch, M.; Ocko, B. M.; Ralston, J.; Rohwerder, M.; Stratmann, M.; Dosch, H., Molecular Layering of Fluorinated Ionic Liquids at a Charged Sapphire (0001) Surface. *Science* **2008,** *322* (5900), 424-428.
15. Cremer, T.; Stark, M.; Deyko, A.; Steinrück, H. P.; Maier, F., Liquid/Solid Interface of Ultrathin Ionic Liquid Films: [C1C1Im][Tf2N] and [C8C1Im][Tf2N] on Au(111). *Langmuir* **2011,** *27* (7), 3662-3671.
16. Jeon, Y.; Sung, J.; Bu, W.; Vaknin, D.; Ouchi, Y.; Kim, D., Interfacial Restructuring of Ionic Liquids Determined by Sum-Frequency Generation Spectroscopy and X-Ray Reflectivity. *The Journal of Physical Chemistry C* **2008,** *112* (49), 19649-19654.
17. Zobel, M.; Neder, R. B.; Kimber, S. A. J., Universal solvent restructuring induced by colloidal nanoparticles. *Science* **2015,** *347* (6219), 292-294.
18. Futamura, R.; Iiyama, T.; Takasaki, Y.; Gogotsi, Y.; Biggs, M. J.; Salanne, M.; Ségalini, J.; Simon, P.; Kaneko, K., Partial breaking of the Coulombic ordering of ionic liquids confined in carbon nanopores. *Nature Materials* **2017,** *16*, 1225.
19. Zhang, H.; Jang, J.; Liu, W.; Talapin, D. V., Colloidal Nanocrystals with Inorganic Halide, Pseudohalide, and Halometallate Ligands. *ACS Nano* **2014,** *8* (7), 7359-7369.
20. Dirin, D. N.; Dreyfuss, S.; Bodnarchuk, M. I.; Nedelcu, G.; Papagiorgis, P.; Itskos, G.; Kovalenko, M. V., Lead Halide Perovskites and Other Metal Halide Complexes As Inorganic Capping Ligands for Colloidal Nanocrystals. *Journal of the American Chemical Society* **2014,** *136* (18), 6550-6553.

21. Fafarman, A. T.; Koh, W.-k.; Diroll, B. T.; Kim, D. K.; Ko, D.-K.; Oh, S. J.; Ye, X.; Doan-Nguyen, V.; Crump, M. R.; Reifsnyder, D. C.; Murray, C. B.; Kagan, C. R., Thiocyanate-Capped Nanocrystal Colloids: Vibrational Reporter of Surface Chemistry and Solution-Based Route to Enhanced Coupling in Nanocrystal Solids. *Journal of the American Chemical Society* **2011,** *133* (39), 15753-15761.
22. Beaucage, G., Small-angle scattering from polymeric mass fractals of arbitrary mass-fractal dimension. *Journal of Applied Crystallography* **1996,** *29* (2), 134-146.
23. Lin, M. Y.; Lindsay, H. M.; Weitz, D. A.; Ball, R. C.; Klein, R.; Meakin, P., Universality in colloid aggregation. *Nature* **1989,** *339*, 360.
24. Feld, A.; Koll, R.; Fruhner, L. S.; Krutyeva, M.; Pyckhout-Hintzen, W.; Weiß, C.; Heller, H.; Weimer, A.; Schmidtke, C.; Appavou, M.-S.; Kentzinger, E.; Allgaier, J.; Weller, H., Nanocomposites of Highly Monodisperse Encapsulated Superparamagnetic Iron Oxide Nanocrystals Homogeneously Dispersed in a Poly(ethylene Oxide) Melt. *ACS Nano* **2017,** *11* (4), 3767-3775.
25. Freeland, B. H.; Habeeb, J. J.; Tuck, D. G., Coordination compounds of indium. Part XXXIII. X-Ray photoelectron spectroscopy of neutral and anionic indium halide species. *Canadian Journal of Chemistry* **1977,** *55* (9), 1527-1532.
26. Fannin, A. A.; King, L. A.; Seegmiller, D. W., Chloroaluminate Equilibria in AlCl3 - NaCl Melts. *Journal of The Electrochemical Society* **1972,** *119* (7), 801-807.

Chapter 6.

Curing structural defects in colloidal GaAs nanocrystals via molten salt annealing

6.1 Introduction

The difficulties with the synthesis of colloidal GaAs NCs have been discussed in detail in Chapter 4. In chapter 4, I also presented in detail the synthesis of colloidal GaAs NCs through a superhydride mediated approach. The particles synthesized were highly crystalline and monodisperse and were a significant improvement over synthetic protocols that existed prior to this work. Through our detailed investigation of the structural aspects of colloidal GaAs NCs we were able to directly correlate its anomalous optical properties to structural defects that are frozen into the lattice when synthesis is done at low temperatures. These structural defects, in turn, manifest themselves in the lack of size dependent excitonic features expected for quantum confined nanostructures.

This structural deficiency seen in colloidal GaAs nanocrystals can be contrasted to the success of gas-phase techniques including metal-organic chemical vapor deposition (MOCVD) and molecular beam epitaxy (MBE) that reliably yield high quality GaAs. These processes are carried out at high temperatures (>600° C) combined with a highly reducing environment.[1] Colloidal syntheses are typically performed at temperatures well below those used for CVD and MBE, which may be responsible for the limited quality of colloidally synthesized GaAs NCs. In fact, MBE GaAs films grown at a low temperature (<500° C) accumulate defects like As_{Ga} antisites and Ga vacancies which negatively affect charge carrier dynamics (Figure 6.1).[2-5] In bulk GaAs, these defects can be annealed out by heating at sufficiently high temperatures.[4-5] This points out

that synthesis of covalent materials require higher temperatures that traditional solvents used for colloidal chemistry can be used.

It has recently been demonstrated that stable colloids of inorganic nanoparticles can be formed in molten inorganic salts that are able to form chemical bonds with the surface of the nanocrystals.[6] Certain molten salt eutectics can not only be stable up to very high temperatures (upto 1000°C), they also offer extremely inert environment for air sensitive reactions.[7] Traditional organic solvents in which colloidal chemistry is performed (such as octadecene or trioctyl phosphine or octadecylphosphonic acids) either boil or decompose at temperatures above ~350°C. Moreover side reactions such as decomposition of organic surface ligands necessary for colloidal stability cannot be avoided at such temperatures.[8] Molten salt fluxes have been previously employed for the synthesis of a variety of nanostructured semiconductors and strongly covalent compounds.[7, 9-11] The ability to disperse colloidal nanocrystals in molten salts offers us the unique possibility of performing precise chemical manipulations on them at high temperatures which can be very useful for defect annealing of covalent semiconductors like GaAs.

In this chapter, I will discuss the effects of high temperature annealing on colloidal GaAs NCs synthesized via the superhydride mediated approach. Further, I will show that colloidal GaAs NCs can be dispersed in molten salts and the molten salts can be used as a medium for the high temperature annealing of colloidal nanomaterials without losing their colloidal stability or a change in morphology.

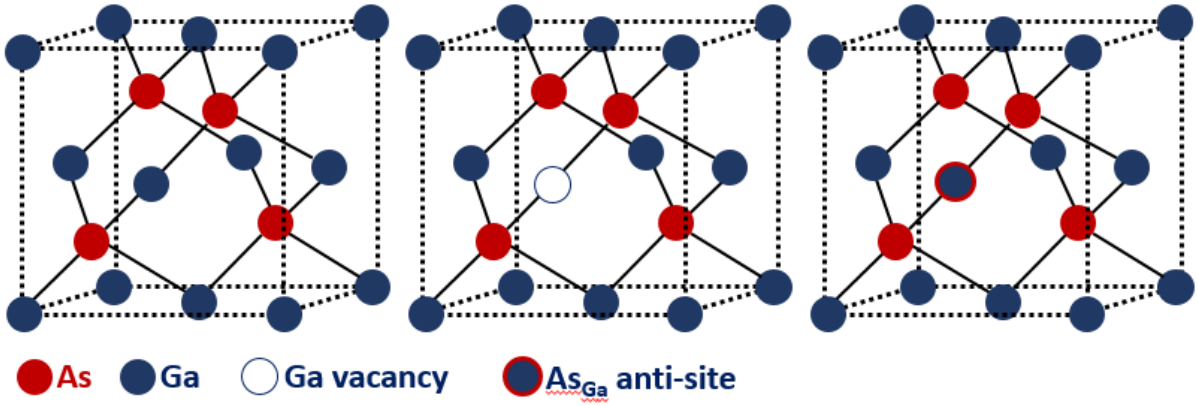

Figure 6.1 Unit cell of cubic zinc blende GaAs and representation of two kinds of structural defects (1) Vacancy defects and (2) Antisite defects.

6.2 High temperature annealing of GaAs films

In order to assess the effects of annealing on GaAs, we first annealed dropcasted thin films of GaAs NCs at 500°C. Annealing as-synthesized GaAs NC films at 500° C for one hour led to the appearance of characteristic GaAs TO and LO phonon modes and complete disappearance of the disorder-related broad feature (Figure 6.2). In order to assess the effect of annealing on the optical properties of GaAs NCs, transient absorption measurements were carried out on annealed GaAs NC films and significant changes were observed (Figure 6.3). TA maps for annealed films of ~6 nm and ~9 nm GaAs NCs are shown in Figures 6.3b and 6.3c respectively. Figure 6.3a shows the TA map for an un-annealed film of ~ 6 nm GaAs NCs for comparison. Following the excitation of GaAs NCs films with 400 nm 35 fs pulse, we observed a ground state bleach typical for NCs of direct gap semiconductors. The ground state bleach was size dependent; centered at around 675 nm for ~6 nm NCs and at 750 nm for larger (~9 nm) GaAs NCs. The bleach feature rapidly shifted to the red at very early times, which can be associated to the hot carrier cooling, before being overshadowed by PA signal.

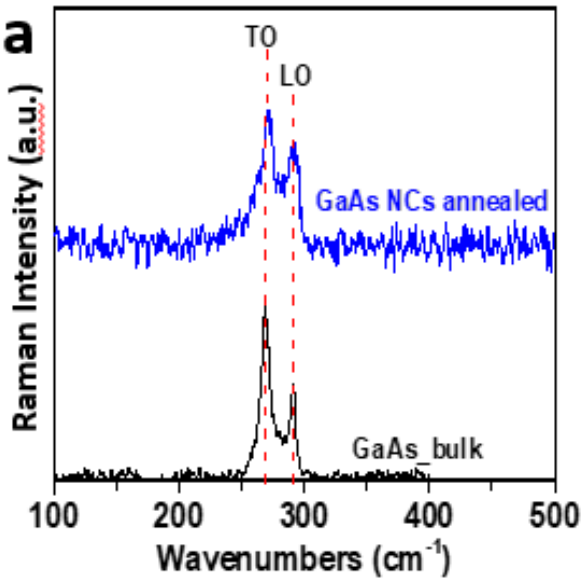

Figure 6.2. **Annealed GaAs films.** Raman spectra of bulk GaAs (black), and GaAs NC film annealed at 500°C (blue).

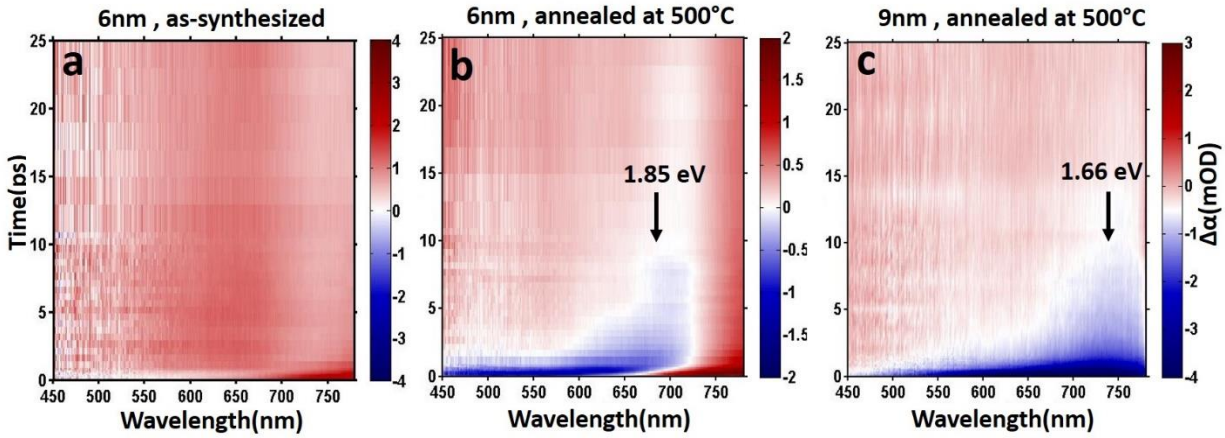

Figure 6.3. **Effect of Annealing on Optical Properties of GaAs NCs.** (a) TA map of as-synthesized ~6 nm GaAs NC film before annealing. (b,c) TA maps showing ground state bleach (blue) and excited state absorption (red) for annealed films of ~6 nm and ~9 nm GaAs NCs, respectively. Same batch of GaAs NCs was used for data shown in panels (a) and (b).

The observation of TA bleach signal after NC annealing suggests that the absence of absorption features in as-synthesized GaAs NCs was not due to indirect transitions, but due to a rather unusual type of lattice disorder. Lattice defects like anti-site defects and vacancy defects are not commonly seen in ionic II-VI semiconductors (e.g., CdSe) where the high diffusivity of ions

allows efficient lattice recrystallization at temperatures typically used for their colloidal synthesis. The short-lived nature of the bleach suggests fast trapping of electrons which should be addressable by proper passivation of surface dangling bonds, e.g., by growing a wide band-gap shell (ZnSe).[12] A serious limitation of this approach is that film-annealed GaAs NCs cannot be redispered and used as colloidal solutions.

6.3 Dispersion of colloidal GaAs NCs in molten Salts

The results shown in the previous section point out to a fundamental limitation of solvents and reactants used for traditional colloidal synthesis of GaAs NCs. It appears that defects annealing in GaAs NCs requires higher temperatures than common solvents and ligands could allow. To address this fundamental issue, we developed new high temperature solvent system utilizing molten inorganic salts. We recently found that various inorganic NCs can be colloidally stabilized in molten inorganic salts.[13] Chapter 5 contains detailed descriptions and in-depth studies of NC dispersions in molten salts. Here, we employed eutectic mixtures of inorganic salts with suitable melting temperatures as a solvent medium for annealing colloidal GaAs NCs. GaAs NCs could be dispersed in a variety of eutectic mixtures, e.g., CsBr:KBr:NaBr (T_m 236°C) or $ZnCl_2$:KCl:NaCl (T_m 203°C) or LiCl:LiI:KCl (T_m 270°C). We chose a eutectic mixture of CsBr:KBr:LiBr (25:56.1:18.9 mol%, T_m 236° C) as a solvent due to its high decomposition temperature and inertness to GaAs. GaAs NCs, bare or capped with inorganic sulfide ligands, could be easily dispersed in this salt matrix at 250° C (inset in Figure 6.4a). Since our spectroscopic studies indicate the presence of Ga vacancies in as-synthesized GaAs NCs (See Chapter 4), we intentionally added GaI_3 to the colloidal solution of GaAs NCs in the molten eutectic to provide a source of Ga^{3+} ions.

In a typical experiment, a eutectic mixture (melting point 236° C) of CsBr:LiBr:KBr (25:56.1:18.9 mol %) was taken in a vial and heated to 250° C under inert atmosphere until a complete liquid phase was formed . 500uL GaAs NCs dispersed in toluene (20mg/mL) were added dropwise to this molten salt mixture while stirring rapidly. ~20mg GaI_3 powder was added to this mixture as a source of Ga^{3+} cations. The mixture was then further heated at 300° C for 1 hr to completely stabilize NCs in the molten salt. The mixture was cooled to room temperature and then transferred to a furnace where it was further heated at 500° C for 1 hr in N_2 atmosphere. The mixture was cooled to room temperature and salt matrix was dissolved using excess water. The GaAs NCs were centrifuged out. The NCs were washed twice with water to completely remove the salt matrix and dried. Finally, the NCs were precipitated by centrifugation and redispersed in FA using $NH4_2S$ (or toluene using DDA^+ as the counter-ion) and used for further characterization. The sulfide capping procedure was as described in chapter 4.

6.4 Molten salt annealed GaAs NCs: Structural Properties

The NC size and morphology were preserved after annealing as seen in TEM images (Figures 6.4a and 6.4b) and powder X-ray diffraction patterns (Figure 6.4c). Characteristic TO and LO phonon modes of pure GaAs phase could be also seen in Raman spectrum (Figure 6.4d). This change in the Raman features while retaining the NC morphology is a clear evidence of lattice reorganization occurring at high temperatures.

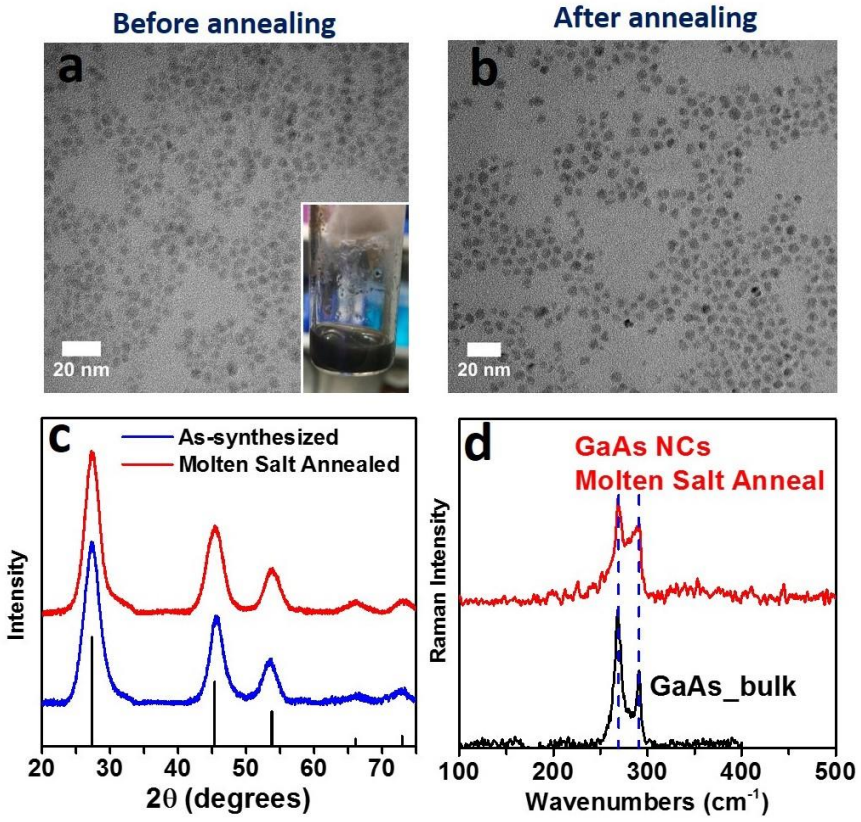

Figure 6.4 GaAs NCs annealed in molten salt. (a) TEM image of GaAs NCs used for dispersion in the eutectic mixture CsBr, KBr and LiBr salts. Inset shows a photograph of GaAs NCs dispersed in the molten salt. (b) TEM image of GaAs NCs recovered from the eutectic CsBr-KBr-LiBr molten salt after annealing at 500°C for one hour. (c) X-ray diffraction patterns of GaAs NCs before (blue) and after (red) annealing in the eutectic mixture at 500°C. (d) Raman spectrum of GaAs NCs recovered after annealing in the molten salt eutectic. The Raman spectrum of bulk GaAs is added as a reference.

Annealing of GaAs NCs in the presence of GaI_3 in molten salts also led to a significant change in the EXAFS spectra of GaAs NCs. As described in chapter 4, the reduced amplitude of Fourier transformed X-ray absorption for the As k edge in as-synthesized GaAs NCs as compared to bulk GaAs suggested that As atoms in GaAs NCs were undercoordinated relative to bulk GaAs.

The EXAFS results of annealed GaAs NCs are shown in Figure 6.5. There was a clear edge in the EXAFS region of the As- k edge. Now the amplitude of X-ray absorption was similar for both

bulk GaAs and colloidal GaAs NCs indicating that the coordination number in both cases was similar. No changes for observed for the Ga edge before and after annealing. This results proves convincingly that indeed there were Ga vacancies present in the as-synthesized GaAs NCs which can be removed by annealing at high temperatures in the presence of excess Ga^{3+} ions. Annealing in molten salts allows us to maintain the size and shape of NCs during this process.

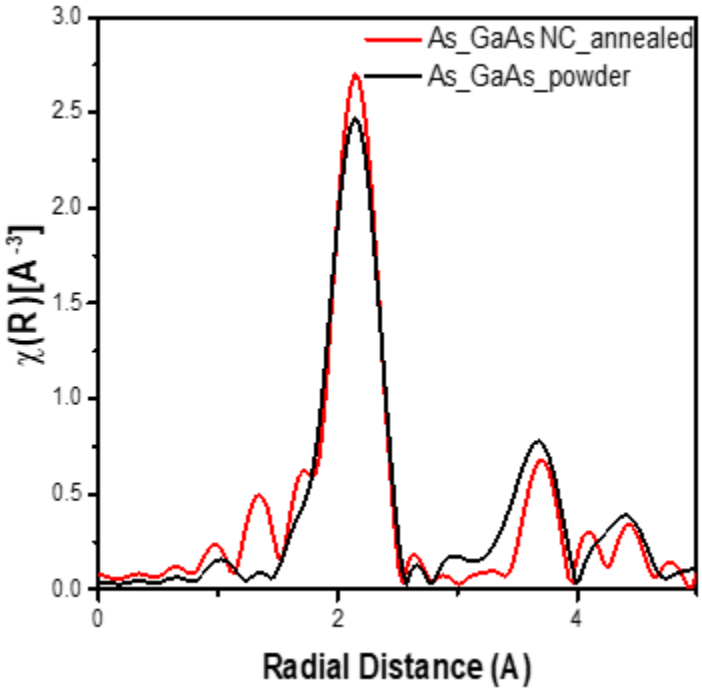

Figure 6.5 EXAFS studies on molten salt annealed GaAs NCs. Comparison of Magnitude of Fourier transforms of k^2 -weighted As K-edge EXAFS measured for GaAs powder (black) and NCs (red).

Annealing of the sample in molten salt eutectic at 500°C in the presence of GaI_3 also resulted in the complete removal of the low temperature EPR signal related to Ga vacancies and formation of a very narrow signal (ΔH_{pp} of 7.4 G) with the g tensor of 2.0031 corresponding to a very small positive shift from the g-value of a free electron spin (Figure 6.6). As all atoms in GaAs sample possess large spin multiplicity (3/2) and large hyperfine splitting, such a narrow signal can

be attributed to motional narrowing effects in well crystallized nanoparticles. Because of high velocity of delocalized electrons in conduction and valence states or in very shallow trapping sites of a well crystallized nanoparticle, electron spin moves rapidly from site to site that is able to experience a complete range of orientational configurations of nuclear moments, and each electron spin experiences an identical, environment-independent, narrow signal with the g tensor close to the one of a free electron spin.

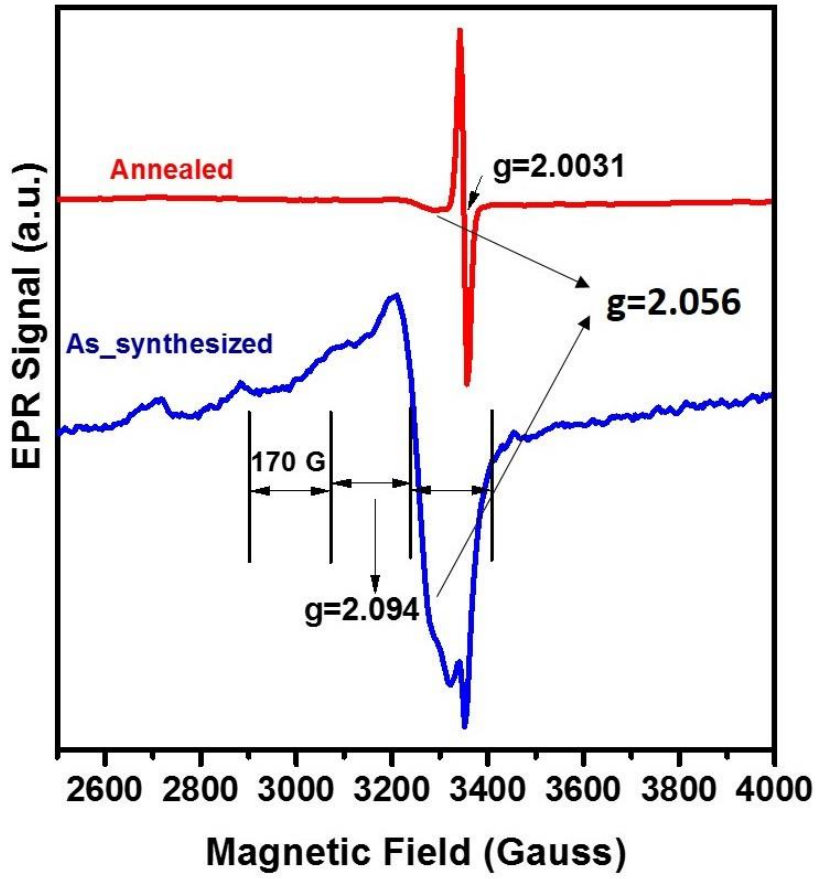

Figure 6.6. EPR spectra of GaAs NCs before (blue) and after (red) annealing in molten salt matrix. EPR spectra were collected at 4K in an X-Band spectrometer. The microwave power was 0.1 mW and the modulation amplitude was 10 G. The signals corresponding to Ga vacancies are completely absent in molten salt annealed GaAs NCs. A broad signal with a g-value of 2.056 is present in both the samples which is attributed to the surface of the NCs.

6.5 Molten salt annealed GaAs NCs: Optical Properties

The annealing of GaAs NCs dispersed in molten salts allowed us to measure the steady state absorption spectra of colloidal solutions of recovered GaAs NCs. The absorption spectrum of a solution of annealed ~ 5nm GaAs NCs shows a marked shoulder centered on 620 nm (Figure 6.7a). The second derivative of the absorption spectrum is also shown in Figure 6.7a (see Figure 6.7b for comparison with as-synthesized sample) which clearly shows a minimum corresponding to the shoulder in the absorption at 621 nm. This corresponds to a ~ 0.55 eV blue-shift with respect to the bulk bandgap, which is in good agreement with theoretical predictions by Brus[14] and Zunger[15], as well as with the experimental data for quantum-confined GaAs nanowires when the dimensionality effect on the quantum confinement is taken into account.[16] Absorption spectra of three different sizes of GaAs NCs recovered after the annealing in molten salt showed expected size-dependent shifts of the excitonic peak (Figure 6.8). The size dependent peak shift is much easily distinguishable in the double derivative of the absorption spectra for different particle sizes (Figure 6.9). Annealed colloidal GaAs NCs also showed a ground state bleach in TA spectra as shown in Figure 6.10a. The spectral position of the TA bleach signal agreed well with the excitonic position ascertained from the second derivative of the steady state absorption as shown in Figure 6.10a. The steady state absorption of the sample corresponding to the TA spectra are shown in Figure 6.10b. The TA bleach feature was short-lived, calling for further improvements in the annealing conditions and GaAs NC surface chemistry. A large width of the excitonic transitions in the absorption and TA spectra of annealed GaAs NCs will require further studies. It could be caused by the fundamental reasons, such as mixing of the excitonic states derived from three proximal valleys in the conduction band of quantum-confined GaAs. An alternative explanation can be the incomplete annealing of structural defects. In the latter case, refinements of the annealing protocol should solve the problem.

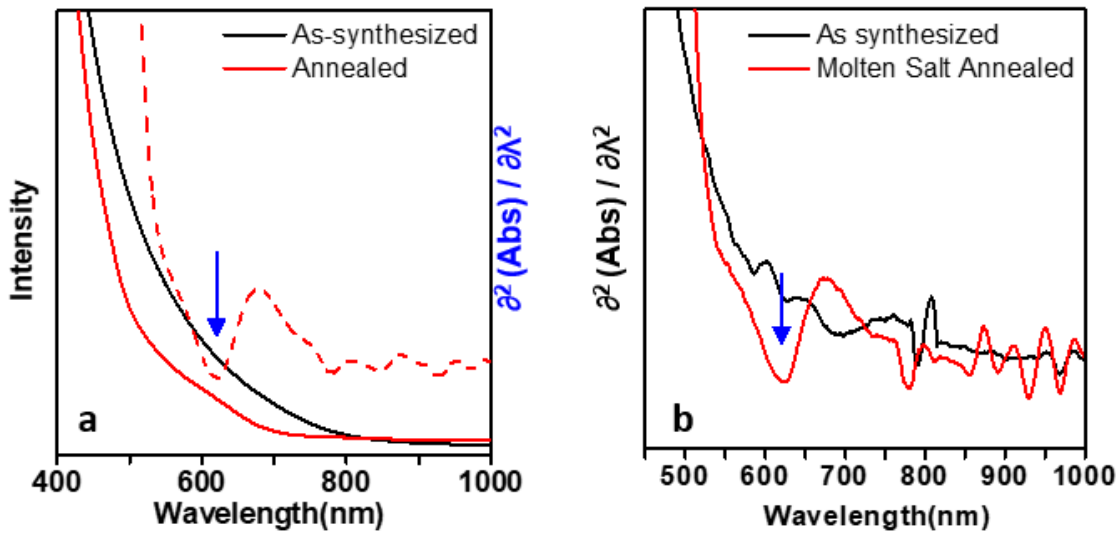

Figure 6.7. Optical Properties of GaAs NCs annealed in molten salt. (a) Absorption spectra of ~5 nm GaAs NCs before (black) and after (red) annealing. The second derivative of the absorption spectrum of annealed GaAs NCs is shown as a dashed line (b) The 2nd derivative of the absorption spectra shown in panel (a) for GaAs NCs before (black) and after (red) annealing.

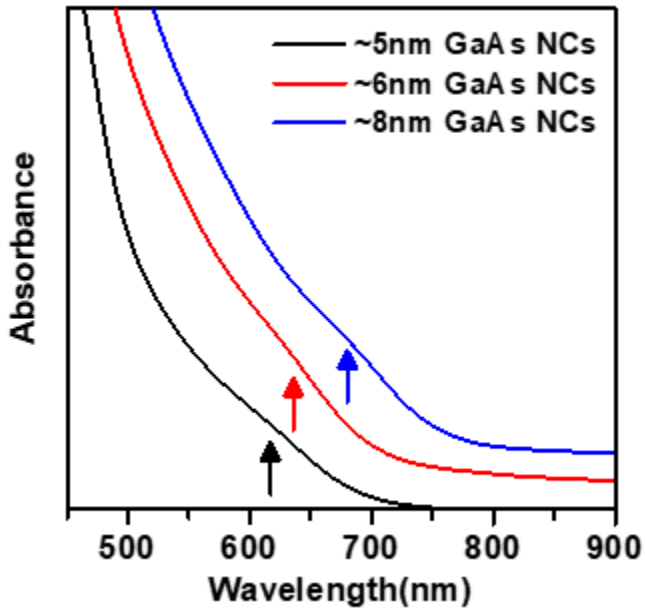

Figure 6.8. Absorption spectra of GaAs NCs with average diameters of ~5 nm, ~6 nm and ~8 nm after annealing in the molten salt eutectics at 500°C

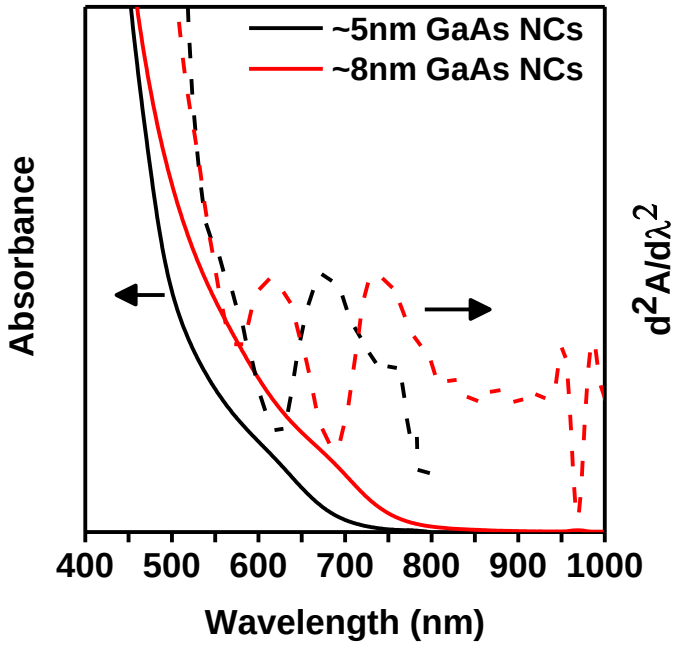

Figure 6.9. Absorption spectra and their 2nd derivatives for ~5nm and ~8nm GaAs NCs recovered after annealing in molten CsBr:KBr:LiBr at 500° C for 1 hour.

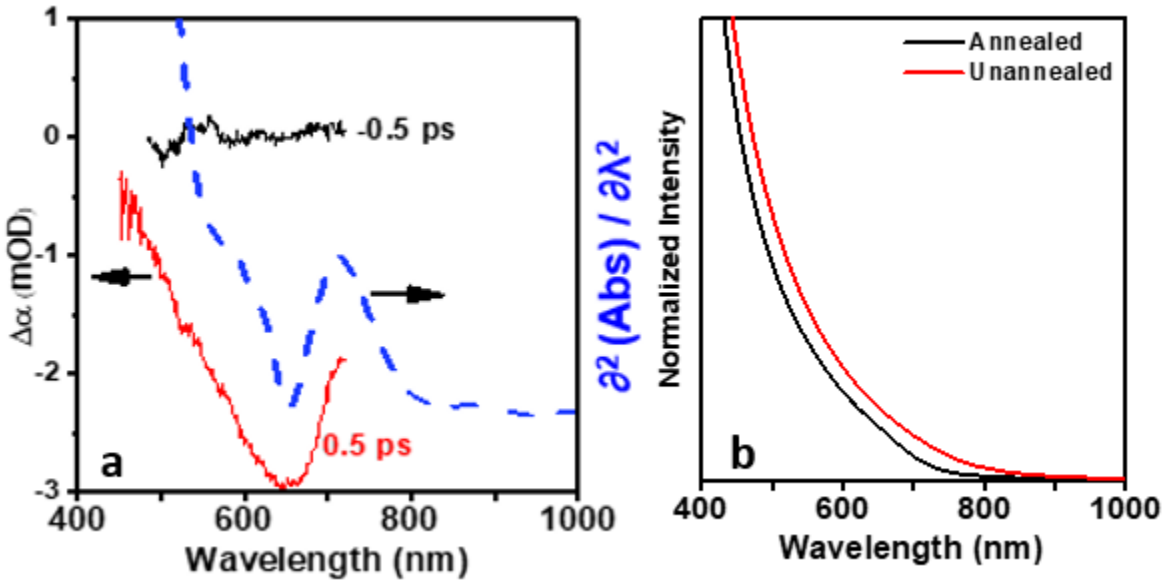

Figure 6.10. (a)Transient absorption time slice of an annealed sample of GaAs NCs along with second derivative of the steady state absorption of the same sample. (b) Absorption spectra of GaAs NCs before and after annealing corresponding to the transient absorption trace shown in panel (a).

6.6 Conclusions

In summary, we demonstrate the use of inorganic molten salts as media to carry out high temperature annealing of GaAs NCs while maintaining their size distribution, an approach not feasible in common organic solvents. The molten salt annealing at high temperatures in the presence of added GaI_3 results in the appearance of size dependent features in steady state and transient absorption spectra of colloidal GaAs NCs. Our results suggest that GaAs NCs retain direct band gap at sub-10 nm size and the excitonic transitions between quantum-confined energy states can be observed once the structural defects are significantly eliminated. This work presents a new perspective on the structural and optical properties of highly covalent semiconductor nanocrystals and highlights the need for new and innovative approaches to synthesize such systems. This ability to manipulate the properties of colloidal semiconductors through high temperature processing paves a pathway for the preparation of novel nanostructures in molten salts at high temperatures which cannot be synthesized by direct colloidal routes.

6.7 References

1. Jones, A. C., Developments in metalorganic precursors for semiconductor growth from the vapour phase. *Chem. Soc. Rev* **1997,** *26* (2), 101-110.
2. Gupta, S.; Whitaker, J. F.; Mourou, G. A., Ultrafast carrier dynamics in III-V semiconductors grown by molecular-beam epitaxy at very low substrate temperatures. *Quantum Electronics, IEEE Journal of* **1992,** *28* (10), 2464-2472.
3. Gant, T. A.; Shen, H.; Flemish, J. R.; Fotiadis, L.; Dutta, M., Raman study of low growth temperature GaAs. *Appl. Phys. Lett* **1992,** *60* (12), 1453-1455.
4. Harmon, E.; Melloch, M.; Woodall, J.; Nolte, D.; Otsuka, N.; Chang, C., Carrier lifetime versus anneal in low temperature growth GaAs. *Appl. Phys. Lett* **1993,** *63* (16), 2248-2250.
5. Kaminska, M.; Weber, E.; Liliental-Weber, Z.; Leon, R.; Rek, Z., Stoichiometry-related defects in GaAs grown by molecular-beam epitaxy at low temperatures. *J. Vac. Sci. Tech.* **1989,** *7* (4), 710-713.
6. Zhang, H.; Dasbiswas, K.; Ludwig, N. B.; Han, G.; Lee, B.; Vaikuntanathan, S.; Talapin, D. V., Stable colloids in molten inorganic salts. *Nature* **2017,** *542*, 328.
7. Liu, X.; Fechler, N.; Antonietti, M., Salt melt synthesis of ceramics, semiconductors and carbon nanostructures. *Chemical Society Reviews* **2013,** *42* (21), 8237-8265.
8. Kovalenko, M. V.; Bodnarchuk, M. I.; Talapin, D. V., Nanocrystal Superlattices with Thermally Degradable Hybrid Inorganic−Organic Capping Ligands. *Journal of the American Chemical Society* **2010,** *132* (43), 15124-15126.

9. Liu, X.; Giordano, C.; Antonietti, M., A molten-salt route for synthesis of Si and Ge nanoparticles: chemical reduction of oxides by electrons solvated in salt melt. *Journal of Materials Chemistry* **2012,** *22* (12), 5454-5459.
10. Liu, X.; Antonietti, M.; Giordano, C., Manipulation of Phase and Microstructure at Nanoscale for SiC in Molten Salt Synthesis. *Chemistry of Materials* **2013,** *25* (10), 2021-2027.
11. Kanady, J. S.; Leidinger, P.; Haas, A.; Titlbach, S.; Schunk, S.; Schierle-Arndt, K.; Crumlin, E. J.; Wu, C. H.; Alivisatos, A. P., Synthesis of Pt3Y and Other Early–Late Intermetallic Nanoparticles by Way of a Molten Reducing Agent. *Journal of the American Chemical Society* **2017,** *139* (16), 5672-5675.
12. Park, J. P.; Lee, J.-J.; Kim, S.-W., Fabrication of GaAs, InxGa1-xAs and their ZnSe core/shell colloidal quantum dots. *J.Am.Chem.Soc.* **2016**.
13. Zhang, H.; Dasbiswas, K.; Ludwig, N. B.; Han, G.; Lee, B.; Vaikuntanathan, S.; Talapin, D. V., Stable Colloids in Molten Inorganic Salts. submitted, 2016.
14. Brus, L. E., Electron–electron and electron-hole interactions in small semiconductor crystallites: The size dependence of the lowest excited electronic state. *J. Chem. Phys.* **1984,** *80* (9), 4403-4409.
15. Luo, J.-W.; Franceschetti, A.; Zunger, A., Quantum-size-induced electronic transitions in quantum dots: Indirect band-gap GaAs. *Phys. Rev. B* **2008,** *78* (3), 035306.
16. Dong, A.; Yu, H.; Wang, F.; Buhro, W. E., Colloidal GaAs Quantum Wires: Solution−Liquid−Solid Synthesis and Quantum-Confinement Studies. *J.Am.Chem.Soc.* **2008,** *130* (18), 5954-5961.

Chapter 7.

Cation Exchange reactions in Molten Salts: Synthesis of Luminescent $In_{1-x}Ga_xP$ and $In_{1-x}Ga_xAs$ Quantum Dots

7.1 Introduction

III-V compounds (GaAs, GaN, InGaP, InGaAs etc) are arguably one of the most important class of semiconductors, along with Si, due to their direct band gaps and superior electronic properties.[1] One of the salient features of these compounds is the ability to make alloys with desired compositions that not only allows the band gaps to be precisely tuned but also allows epitaxial growth of complex multilayer device architectures essential for device function. For instance, epitaxially matched InGaP/GaAs stacks are used for high efficiency multi-junction solar cells.[2-3] Similarly, InGaAs is grown on an epitaxially matched InP substrate for near-infrared (NIR) detector applications.[4]

Colloidal quantum dots (QDs) of III-V compounds have been shown to be promising candidates for a plethora of applications such as display technology,[5] LEDs,[6-7] thin-film transistors[8] and bioimaging[9-10]. In the recent years, InP is replacing CdSe as the material of choice in quantum dot based displays due to its lower toxicity.[11-12] The other members of the III-V family such as InAs and InSb have also seen significant surge in interest as infrared active materials for applications like bioimaging, night vision and telecommunication.[13-14]

Even though the synthetic chemistry of colloidal III-V semiconductors has seen significant progress,[15-17] Ga based III-V QDs remain under-developed. For example , colloidal GaAs QDs are still difficult to synthesize due to crystalline defects formed when GaAs QDs synthesized at temperatures relevant for colloidal chemistry.[18] The covalent character of Ga pnictides and the high oxophilicity of Ga makes the synthesis of Ga containing III-V compounds challenging.[18-21]

Ga containing ternary III-V QDs, e.g., $In_{1-x}Ga_xP$ and $In_{1-x}Ga_xAs$, are technologically important compounds due to the flexibility they offer in terms of band gap and lattice constant engineering. For example, $In_{1-x}Ga_xP$ nanoparticles emitting green light should be more efficient and stable than their InP counterparts due to their larger size (and number of unit cells) and hence larger absorption cross-sections. Moreover incorporation of Ga into the InP lattice, reduces the lattice mismatch with wider gap shell materials such as ZnS making the core shell material less strained.[22] It is impossible to make a graded shell for III-V/II-VI system due to disruption in the electron count. Graded shells have shown to be important for slowing down Auger recombination rates.[23] Core shell nanocrystals with a III-V/III-V interface are also potentially better than III-V/II-VI core shells as they minimize strain and avoid disruption in electron count at the interface.[24] Therefore, we argue, that for the efficient incorporation of III-V nanocrystals into commercial technologies, the ability to engineer their composition will be essential.

Attempts to synthesize III-V nanocrystals with alloy compositions such as $In_{1-x}Ga_xP$ or $In_{1-x}Ga_xAs$ via direct synthetic routes have so far seen only limited success.[20, 25-26] Crystalline $In_{1-x}Ga_xP$ nanocrystals could only be obtained upon annealing the reaction product at 400°C.[20] Cation exchange reactions have proven to be a successful strategy to obtain alloy compositions in ionic nanocrystals.[27-28] However similar attempts on III-V nanocrystals have only resulted in surface exchanges even at elevated temperatures.[22, 24] While the transformation of CdSe to Ag_2Se can be spontaneously achieved at room temperature,[28] the transformation of Cd_3As_2 (II-V compound) to GaAs is only possible at 300°C.[29] This can be attributed to the large difference in the diffusivity of cations in covalent III-V semiconductors as compared to the more ionic II-VI semiconductors.[30] For these reasons, even thermodynamically favorable cation exchange reactions in III-V nanocrystals require high temperatures to overcome diffusion barriers.

The Talapin group recently reported that stable colloids of inorganic nanoparticles can be formed in molten inorganic salts.[31] Many molten salt eutectics are not only stable up to very high temperatures, they also offer an extremely inert environment for air sensitive reactions.[32] Molten salt fluxes have been previously employed for the synthesis of a variety of nanostructured semiconductors and strongly covalent compounds.[32-35] The ability to disperse colloidal nanocrystals in molten salts offers us the unique possibility of performing precise chemical manipulations on them at high temperatures. In this chapter, I demonstrate the synthesis of ternary $In_{1-x}Ga_xP$ and $In_{1-x}Ga_xAs$ QDs via cation exchange reactions performed on pre-synthesized InP and InAs QDs dispersed in molten salts as an example (Figure 7.1a). The resultant ternary III-V QDs show absorption and emission features that are blue shifted in comparison to the starting materials, in line with the expected change in band gap upon alloying (Figure 7.1b). Bright luminescence with quantum yields of up to 50% can be obtained from core-shell $In_{1-x}Ga_xP$ /ZnS nanocrystals making them potential candidates for next generation Cd-free display technology.

7.2 Experimental methodolgy for cation exchange reactions in molten Salts.

Colloidal InP and InAs QDs can be dispersed in a variety of inorganic salt eutectics (See Chapter 5 for details) such as NaSCN/KSCN (26.3:73.7 mol %, m.p. 137°C) or CsBr:LiBr:KBr (25:56.1:18.9 mol%, m.p. 236°C). The native organic ligands were first removed from the QD surface by either using HBF_4 as the stripping agent or by decorating the QDs surface with short inorganic S^{2-} ligands.[36] Dried powders of organic ligand free QDs were stirred in the molten salt at temperatures slightly above their melting point for prolonged periods to obtain stable dispersions (Figure 7.1c). The dispersions of InP and InAs QDs in molten CsBr:LiBr:KBr were stable at temperatures well beyond 400°C. At these temperatures, traditional organic solvents and surface ligands either boil or decompose.[37] The stability of QDs in molten salts has been attributed to the

ability of the salt anions and cations to form strongly ordered templates around the nanocrystal surface (Figure 7.1a).[31] Both halide and SCN^- ions are well-known to bind to the surface of III-V nanocrystals which is essential to induce enhanced ordering of the ions.[38-39]

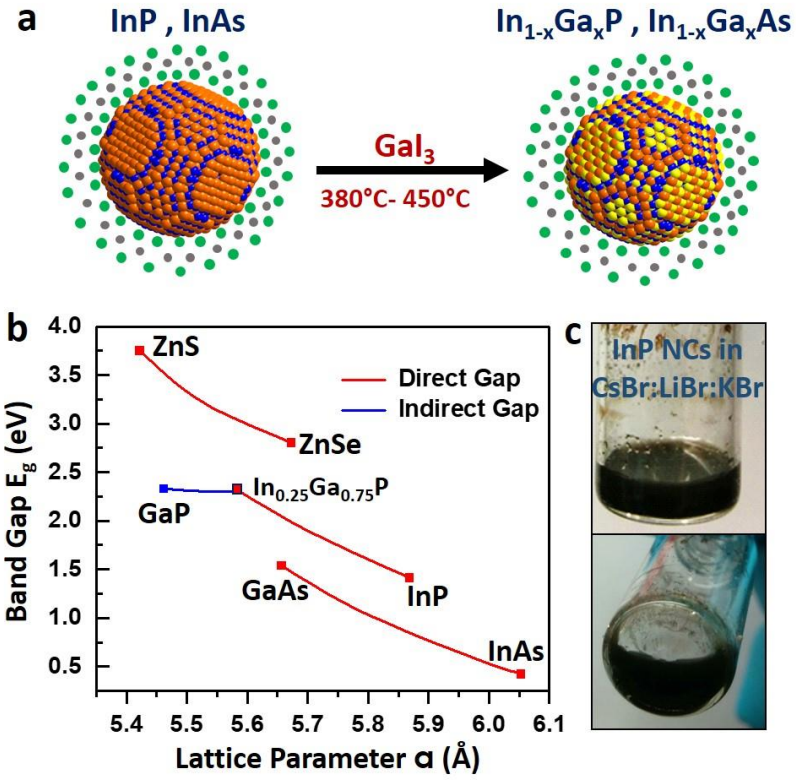

Figure 7.1 Cation exchange on III-V QDs in molten salts (a) Schematic showing the cation exchange process in molten salts. The templating of molten salt ions around the QD surface is responsible for stabilization of QDs in molten salt. The green and grey circles represent the anions and cations respectively. Addition of GaI_3 salt to the molten salt dispersion of InP or InAs QDs leads to cation exchange to form $In_{1-x}Ga_xP$ or $In_{1-x}Ga_xAs$ QDs. (b) The lattice constants and bulk band gaps (at 0 K) of alloys of InP and GaP, InAs and GaAs and ZnS and ZnSe. ZnS and ZnSe are typically used as the wide gap shell materials for InP QDs (c) Pictures of InP NC dispersions in molten CsBr:LiBr:KBr eutectic.

7.2.1 Ligand Exchange on InP and InAs QDs.

The purified InP and InAs QDs (~0.3 mmol QDs) were transferred to the polar formamide (FA) phase using $(NH_4)_2S$ as inorganic capping ligands. 200 uL volume of 40-48% aq. $(NH4)_2S$ solution in 10 mL FA and QDs suspended in toluene were stirred together for 20 min to completely transfer the particles to the polar FA phase. The organic phase was removed and fresh toluene was added and the biphasic mixture was stirred for another 15mins. This process was repeated thrice to completely remove all the organic ligands. The particles were colloidally stable in FA. The particles could be precipitated using excess CH_3CN and dried as powders. These powders were further used for dispersion in the molten salts.

Alternatively, the particles could be transferred from the FA phase to toluene using didodecyldimethylammonium bromide (DDAB) as the phase transfer agent. This ligand decomposes cleanly into gaseous products via Hoffman elimination leaving no organics behind.[37] The toluene phase containing QDs was transferred to a centrifuge tube and precipitated with ethanol to get rid of excess ligands and re-dispersed in 2-3 mL of toluene. This solution was used for dispersion in molten salts. Absorption spectra before and after the ligand exchange were measured in toluene. Bare InP QDs were prepared by stripping with HBF_4 using previously reported protocols.[36] Bare InP QDs were used as powders for dispersion in the molten salts.

7.2.2 Dispersion of InP and InAs QDs in Molten Salt Matrix and Cation Exchange into $In_{1-x}Ga_xP$ and $In_{1-x}Ga_xAs$ QDs.

To perform cation exchange reactions on III-V QDs, we chose the CsBr:LiBr:KBr eutectic due to its high temperature stability, low vapor pressure, high solubility of group III halides and inertness to InP and InAs QDs.[40] QDs capped with sulfide ligands showed better stability in this eutectic mixture and also did not show Ostwald ripening in these salts. A eutectic mixture of CsBr:LiBr:KBr (25:56.1:18.9 mol % , (melting point 236° C)) was taken in a vial and heated to

250° C under inert atmosphere until a complete liquid phase was formed . The molten salt was cooled to r.t. and grinded into a fine powder. ~0.3 mmol InP/InAs QD powders capped with S^{2-} ligands were then added as powder or as a toluene solution (see section above) to the finally grinded eutectic mixture and heated to 275° C under stirring for a few hours until a stable solution was obtained. Similar protocols were used for the dispersion of QDs in other molten salts. For cation exchange, ~4-8 molar equivalents of GaI_3 (0.5g -1 g GaI_3) was added to the QD/molten salt dispersion as a source of Ga^{3+} cations. $GaCl_3$ or $GaBr_3$ could also be added as a source of Ga^{3+}, however best results were obtained with GaI_3 due to its higher boiling point. According to the HSAB principle, the softer In^{3+} should have a higher preference than Ga^{3+} for the soft iodide ion favoring the exchange. The mixture was then further heated at 300° C for 1 h to completely homogenize the QDs and dopant salt. The mixture was cooled to room temperature and then transferred to a furnace where it was further heated at a desired temperature (380°C -500°C) for 1 h in N_2 atmosphere. The mixture was cooled to room temperature and salt matrix was dissolved using excess FA. The cation exchanged QDs were centrifuged. The QDs were washed twice with FA to completely remove the salt matrix. Finally, the QDs were re-dispersed in FA using $NH4_2S$ (~100 uL in 10 mL FA) and transferred to toluene using DDA^+ as the counter-ion and used for further characterization. This surface capping procedure is similar to the one described above. Size selection of the crude solution in toluene into a desired number of fractions was performed by sequential precipitation with an appropriate amount of ethanol.

7.3 Structural Properties of Ternary $In_{1-x}Ga_xP$ and $In_{1-x}Ga_xAs$ alloy QDs.

Gallium pnictides are thermodynamically more stable than their corresponding Indium pnictides. For example, the standard heat of formation of GaP and InP is -103.2 kJ/mol and -70.2 kJ/mol respectively (-87.7 kJ/mol and -60 kJ/mol for GaAs and InAs).[41] Therefore the cation

exchange is only diffusion limited and can be accelerated by increasing the reaction temperature. The extent of Ga incorporation in the QDs could indeed be controlled by the temperature at which the exchange was performed. Figure 7.2a shows X-ray diffraction patterns of $In_{1-x}Ga_xP$ nanocrystals with varying compositions obtained from cation exchange at temperatures ranging from 380°C- 430°C. A consistent shift of all X-ray reflections to higher 2θ values was observed with increasing temperature which suggests increasing Ga incorporation into the lattice with temperature. We obtained similar results for $In_{1-x}Ga_xAs$ NCs (Figure 7.2b), however, the temperature range needed for Ga incorporation was 400°C- 450°C. No change in XRD patterns was observed when the particles were annealed in the absence of GaI_3 (Figure 7.3). The full width at half maximum (fwhm) of the (111) diffraction peak did not appreciably change when the cation exchange reactions were performed at temperatures below 450°C indicating that the QDs did not grow or etch significantly. Although we could drive the composition almost completely to the GaAs phase when the exchange was performed at 500°C, it was accompanied by significant narrowing of the diffraction peaks, indicative of an increase in the particle size (Figure 7.4). The composition of the alloy was estimated from the lattice parameters using the Vegard's law (Figures 7.2a and 7.2b). ICP-OES analysis of the QDs was found to be in a good agreement with the compositions estimated from the X-ray diffractions patterns (Tables 7.1 and 7.2). Further insight into the nature of alloying could be obtained from Raman spectroscopy. Figures 7.2c and 7.2d show the Raman spectra for different alloy compositions of $In_{1-x}Ga_xP$ and $In_{1-x}Ga_xAs$ QDs. A continuous one-mode shift in the TO and LO phonon modes of the parent InP and InAs phase could be seen for $In_{1-x}Ga_xP$ and $In_{1-x}Ga_xAs$ QDs with increasing Ga incorporation indicating that the alloy QDs did not have phase segregated domains of InP and GaP. We observed that the TO and LO phonon features for the alloys with higher Ga component showed significant broadening

indicating the lack of a long range order between In and Ga sub-lattices in the alloy QDs. Similar Raman spectra have been reported for InGaP nanowires grown using the Solution-Liquid-Solid (SLS) method.[42]

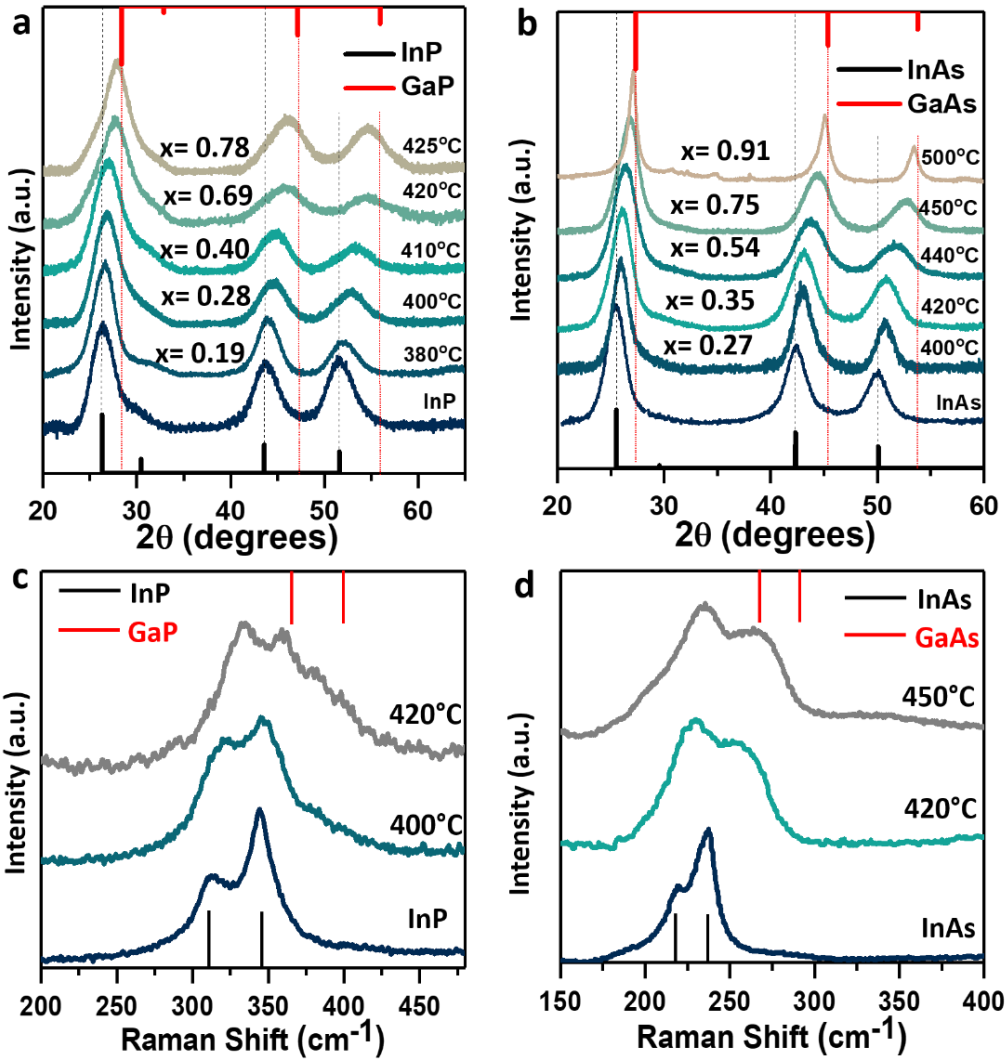

Figure 7.2 Structural properties of alloy QDs (a,b) X-Ray diffraction patterns of $In_{1-x}Ga_xP$ and $In_{1-x}Ga_xAs$ alloy QDs obtained by cation exchange at different temperatures. The vertical lines show the positions and intensities of X-ray reflections of bulk InP, GaP, InAs and GaAs. (c,d) Raman spectra of $In_{1-x}Ga_xP$ and $In_{1-x}Ga_xAs$ alloy QDs obtained by cation exchange at different temperatures. The vertical lines show the corresponding TO and LO phonon modes of bulk InP, GaP, InAs and GaAs.

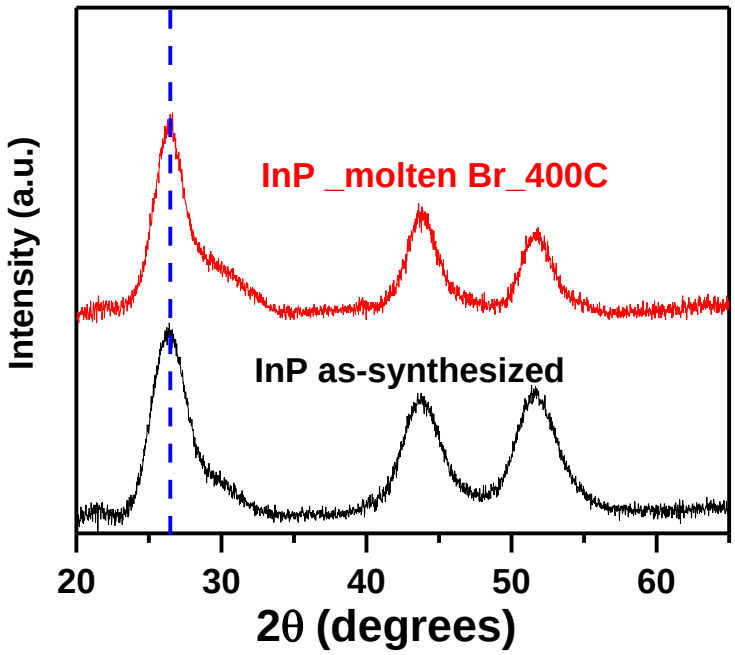

Figure 7.3 X-ray diffraction patterns of as-synthesized InP QDs and InP QDs after annealing in molten CsBr:LiBr:KBr in the absence of GaI_3

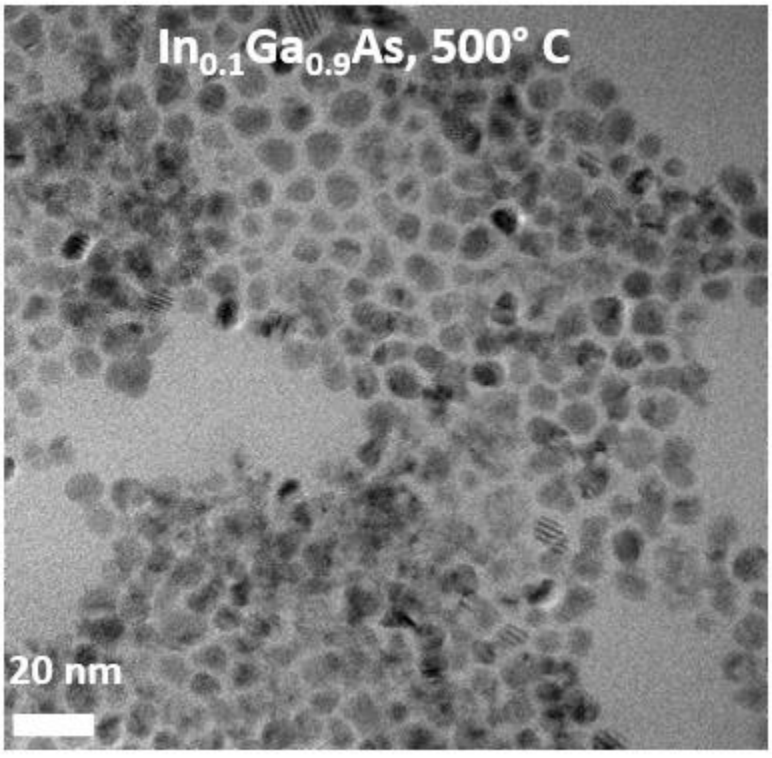

Figure 7.4 TEM image of $In_{0.1}Ga_{0.9}As$ QDs obtained by cation exchange performed at 500°C.

Temperature	Composition from XRD (%Ga)	Composition from ICP-OES	Metal : P ratio
400°C	28%	35%	1.34
410°C	40%	47%	1.37
420°C	69%	68%	1.49
425°C	78%	77%	1.34

Table 7.1 Compositional analysis of $In_{1-x}Ga_xP$ QDs from ICP-OES and its comparison to composition estimated from XRD patterns

Temperature	Composition from XRD (%Ga)	Composition from ICP-OES	Metal : As ratio
400°C	27%	30%	0.94
440°C	54%	61%	1.14
450°C	75%	77%	1.02
500°C	91%	91%	1

Table 7.2 Compositional analysis of $In_{1-x}Ga_xAs$ QDs from ICP-OES and its comparison to composition estimated from XRD patterns.

7.4 Morphological Characterization of ternary $In_{1-x}Ga_xP$ and $In_{1-x}Ga_xAs$ alloy QDs.

We characterized the morphology of the alloy $In_{1-x}Ga_xP$ and $In_{1-x}Ga_xAs$ QDs using electron microscopy. Figure 7.5a shows a representative STEM image of $In_{1.x}Ga_xP$ QDs. A high resolution STEM image showing clear lattice fringes is shown in the inset. The homogeneity of structural

alloying is further supported by high resolution energy dispersive X-ray (EDX) chemical mapping of $In_{1-x}Ga_xP$ QDs (Figures 7.5b). We could detect the presence of both indium and gallium in each individual QD without any apparent phase segregation. Elemental line scans on individual QDs are shown in Figure 7.6. Figure 7.7 shows a STEM-EDS map of an individual $In_{1-x}Ga_xAs$ QD showing the presence of both In and Ga atoms in it. We did not observe a significant change in the size of QDs upon cation exchange. Figures 7.5c and 7.5d show TEM images of the starting InP QDs and the resultant $In_{0.6}Ga_{0.4}P$ QDs obtained after cation-exchange at 410°C for comparison. Small angle X-ray scattering (SAXS) analysis was employed to quantitatively study the change in the size and size distribution of the QDs upon cation exchange (Figures 7.5e). The average size of $In_{0.6}Ga_{0.4}P$ QDs shrunk by ~3% which is consistent with the change in volume expected due to the smaller unit cell of GaP compared to InP (a_{InP}= 0.586 nm and a_{GaP}= 0.545 nm). The size distribution of 11 % for the initial InP dots increased to 13.5 % after the cation exchange. Similar results were obtained when cation exchange was performed on InAs QDs. TEM images of $In_{0.5}Ga_{0.5}As$ QDs and the starting InAs QDs are shown in Figure 7.8. High resolution TEM images of $In_{1-x}Ga_xP$ and $In_{1-x}Ga_x$ As QDs are shown in Figures 7.9 and 7.10. The distance between (111) reciprocal lattice points was estimated from the Fourier transform of the HRTEM image of an individual alloy QD which pointed to the shrinking of unit cell dimension from a= 5.9 Å to a= 5.6 Å (Figure 7.11).

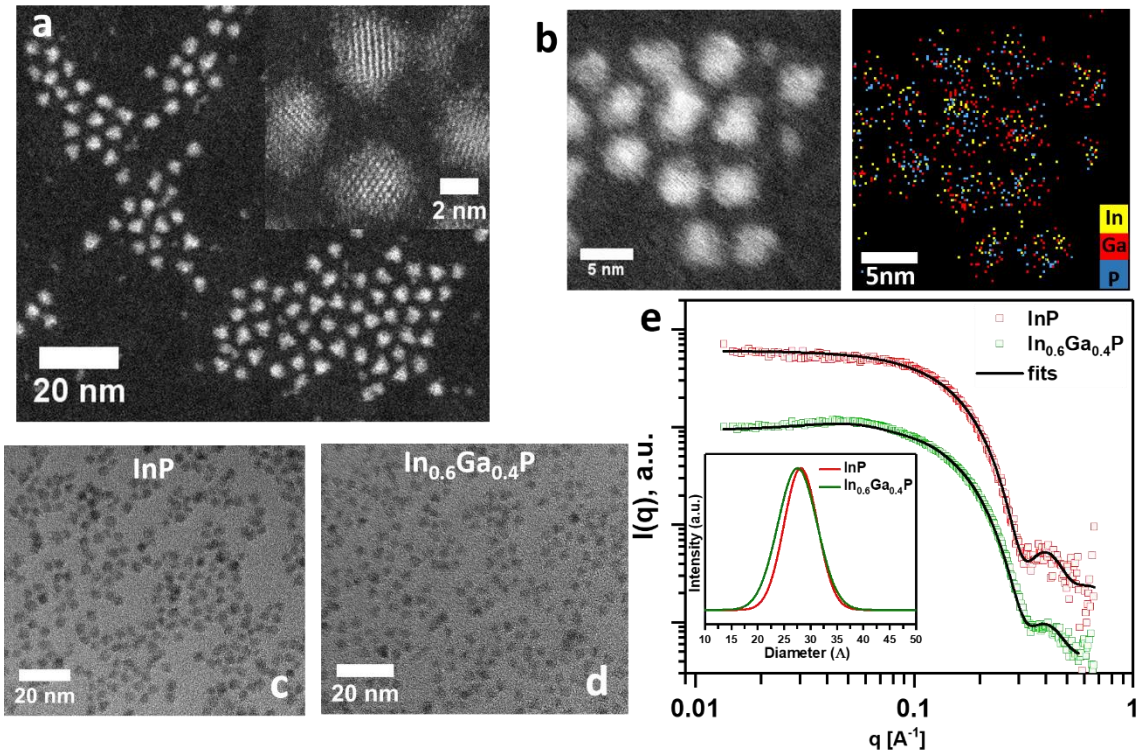

Figure 7.5 Morphology of the alloy QDs (a) STEM image of $In_{1-x}Ga_xP$ QDs. Inset shows a high resolution STEM image with clearly visible lattice fringes (b) Energy dispersive X-ray map and the corresponding STEM image showing a homogenous distribution of indium and gallium in every particle. For Ga and P, the Kα edge was measured whereas for In Lα edge was measured (c,d)TEM image of InP QDs and the $In_{0.6}Ga_{0.4}P$ alloy QDs. (e) Experimental SAXS curves (open squares) and the fits (black lines) for InP and $In_{0.6}Ga_{0.4}P$ QDs. Inset shows the size distributions extracted from the fits.

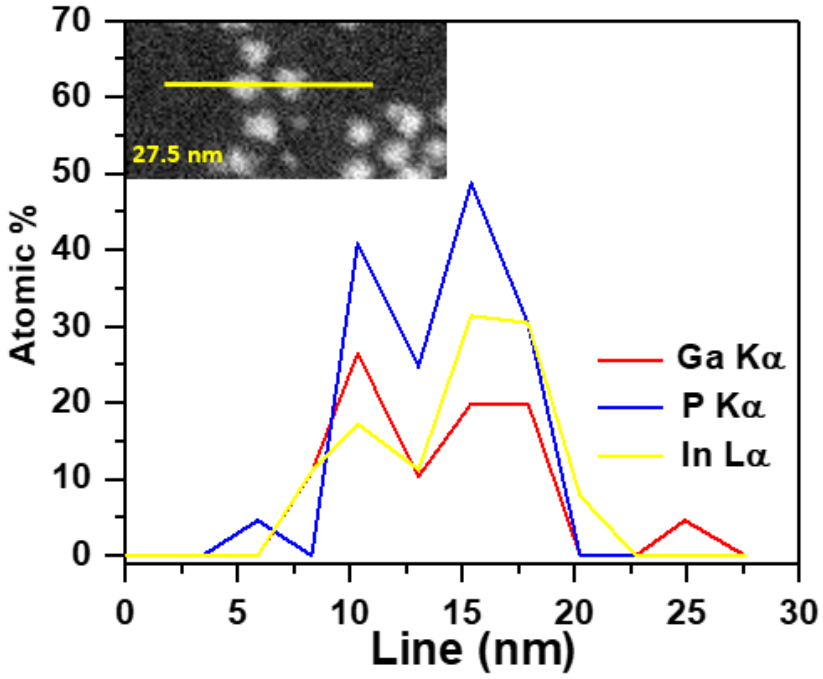

Figure 7.6 EDX line scan showing the intensity profile of each element across the line shown in the STEM image in the inset.

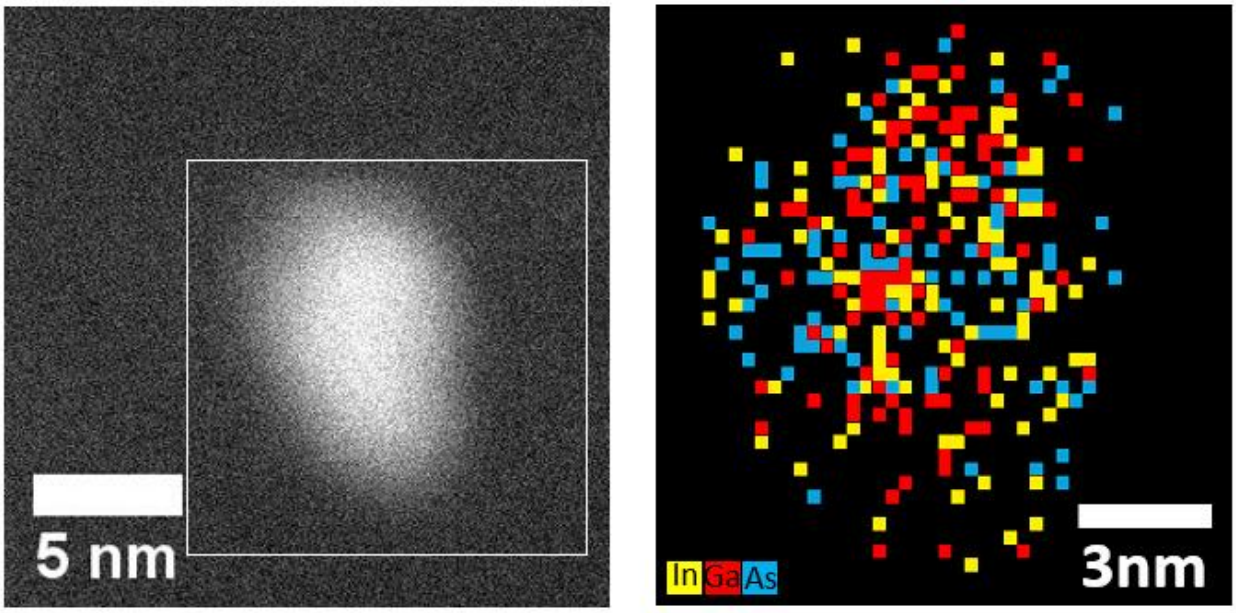

Figure 7.7 STEM image of an $In_{1-x}Ga_xAs$ QD and EDX map of the area inside the square.

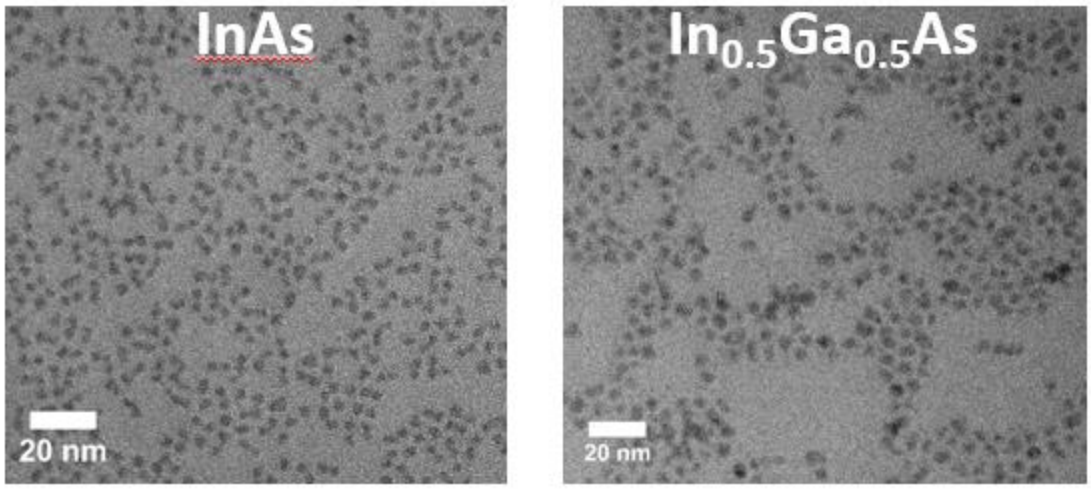

Figure 7.8 TEM image of starting InAs and resultant $In_{0.5}Ga_{0.5}As$ QDs obtained by cation exchange performed at 450°C.

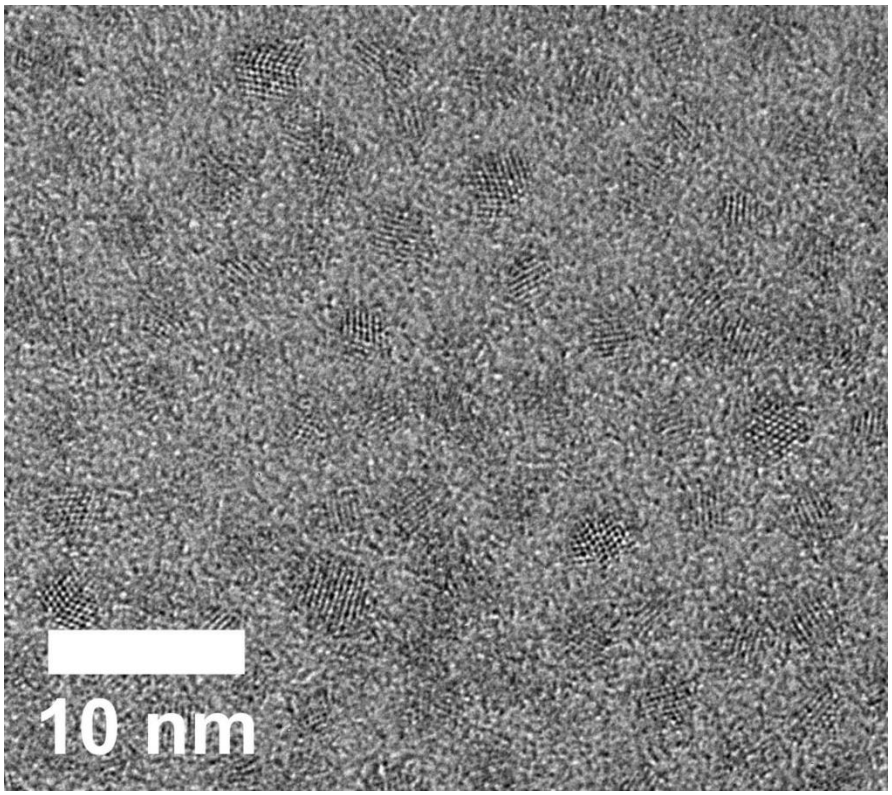

Figure 7.9 HR-TEM image of $In_{1-x}Ga_xP$ alloy QDs

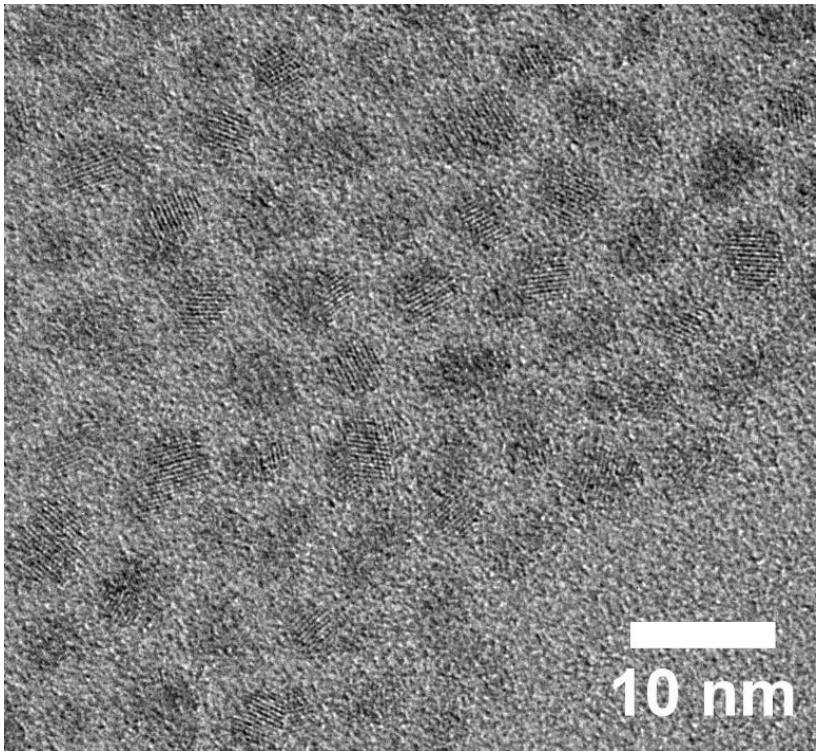

Figure 7.10 HR-TEM image of $In_{1-x}Ga_xAs$ alloy QDs

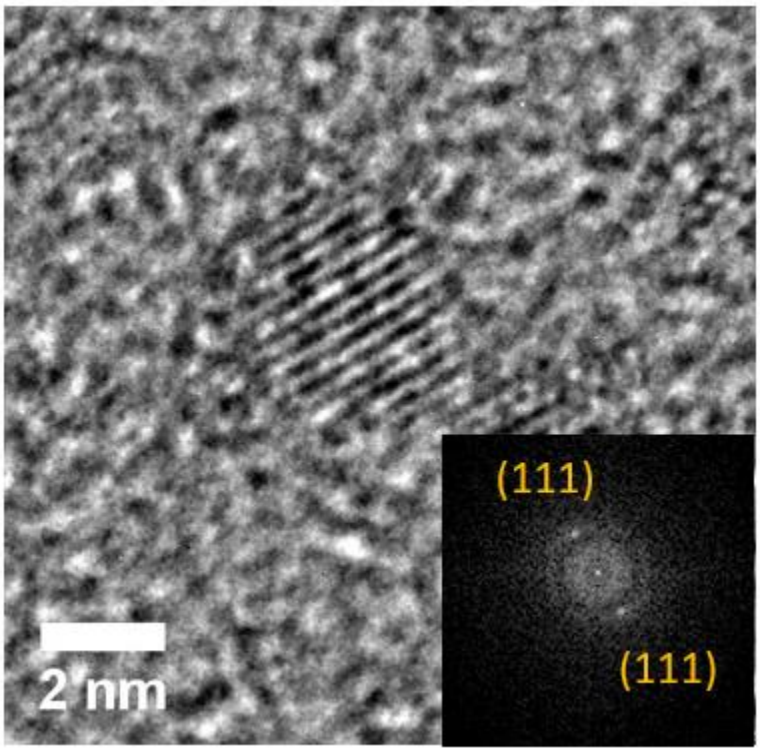

Figure 7.11 HR-TEM image of an individual $In_{1-x}Ga_xP$ alloy QD. The FFT points correspond to the (111) lattice planes.

7.5 Optical Properties of Ternary $In_{1-x}Ga_xP$ and $In_{1-x}Ga_xAs$ alloy QDs.

7.5.1 Optical Properties of Ternary $In_{1-x}Ga_xP$ QDs

Next, we studied the effect of Ga incorporation on the optical properties of InP QDs. InP QDs shelled with a wide band gap II-VI semiconductor such as ZnS are currently used as the red and green emitters in commercial displays, however they suffer from issues like low absorption of blue light (450nm), poor photostability and lower emission quantum yields. Alloyed $In_{1-x}Ga_xP$ QDs are expected to show continuously blue shifted absorption with increasing Ga content as compared to InP QDs of the same size owing to the larger band gap of GaP ($E_{g,bulk}$ = 2.3eV(indirect)/2.77eV(direct)) as compared to InP ($E_{g,bulk}$ = 1.34eV). Figure 4a shows the absorption spectra of $In_{1-x}Ga_xP$ QDs synthesized at different temperatures. The excitonic features were continuously blue shifted with increasing values of x for $In_{1-x}Ga_xP$ alloy QDs. No blue shift of absorption was observed when InP QDs were annealed in molten salts without GaI_3 (red curve in Figure 7.12a). Similar blue shifts were observed upon alloying in InP QDs of all sizes (Figure 7.12b and 7.13). The extent of blue shift was found to vary for different QD sizes and was not linearly correlated to the % of Ga in the lattice, which can be attributed to the band-bowing effect in ternary $In_{1-x}Ga_xP$.[43]

The absorption features for the alloy QDs are generally broader as compared to the starting materials which can be attributed to two factors (1) there may be some heterogeneity in the distribution of Ga in the ensemble and (2) a slight change in size distribution is also observed after cation exchange. We believe that both these factors can be mitigated by mechanical stirring of the reaction mixture during the high temperature cation exchange. Further optimization and scale up of this process should also result in better size dispersions. It should also be noted here that broad absorption features have previously been observed for other QDs with ternary compositions.[25, 44]

We resorted to mild size selective precipitation to partially eliminate the effect of ensemble heterogeneity on the optical properties of the alloy QDs. Size selective precipitation allowed us to separate the particles into smaller batches with tighter size distributions and narrower excitonic features. The absorption spectra of a size-selected fraction of $In_{0.6}Ga_{0.4}P$ QDs and InP QDs with very similar mean size and size distribution are shown in Figure 7.14 for comparison. The absorption features were slightly broader for the alloy QDs as compared to the binary phase which can be attributed to either heterogeneity in Ga incorporation or intrinsic differences in the exciton fine structure.

As-synthesized $In_{1-x}Ga_xP$ QDs also showed band-edge emission which was blue shifted as compared to the starting InP NCs (Figure 7.15). Figure 7.12c shows the representative emission spectra of alloy $In_{1-x}Ga_{1-x}P$ QDs corresponding to their absorption spectra. The full width at half maximum for the PL band was less than 50 nm for all size ranges which is slightly larger than what can now be achieved by state of the art InP QDs.[45] The stokes shift for $In_{1-x}Ga_{1-x}P$ QDs is comparable to that obtained for InP particles emitting at similar wavelengths. We also estimated the molar extinction coefficient of $In_{0.6}Ga_{0.4}P$ alloy QDs and compared it to InP QDs with a similar emission maxima as that of the alloy QDs (Figure 7.12d). The extinction coefficient per particle for the alloy QDs was found to be significantly higher than that of InP QDs. This is expected since the extinction coefficients of QDs scale linearly with the number of unit cells which is higher for InGaP than InP for the same QD size.[46-47] The absorption cross-section at 450nm for the alloy QDs with emission maxima centered at 576 nm was found to be 1.5 times that of InP QDs emitting at the same wavelength. This is of great significance from the point of view of display applications where blue light is used to excite the green and red emitting nanocrystal phosphors.

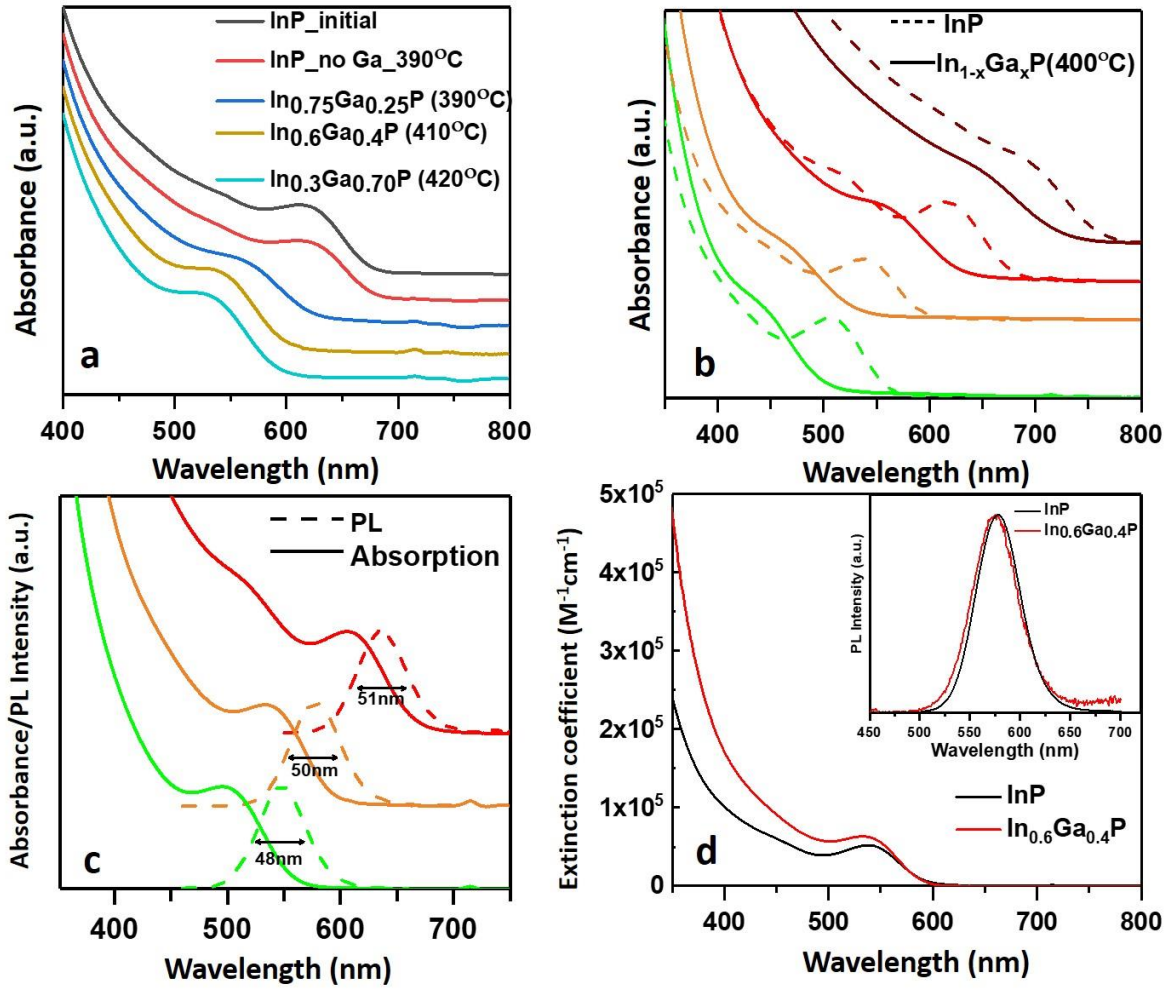

Figure 7.12. Optical properties of $In_{1-x}Ga_xP$ QDs (a) Absorption spectra of starting InP QDs (black), InP QDs after annealing in molten CsBr:LiBr:KBr without GaI_3 (red) and $In_{1-x}Ga_xP$ QDs synthesized from InP QDs at different temperatures. (b) Absorption Spectra of different sizes of InP QDs and $In_{1-x}Ga_xP$ QDs obtained from them after a cation exchange reaction at 400°C. (c) Absorption and Emission spectra of representative $In_{1-x}Ga_xP$ QDs showing stokes shifts and full-width half maximum of the emission bands. (d) Comparison of Molar extinction coefficients (per particle) of InP and $In_{1-x}Ga_xP$ QDs with similar emission profiles (see inset).

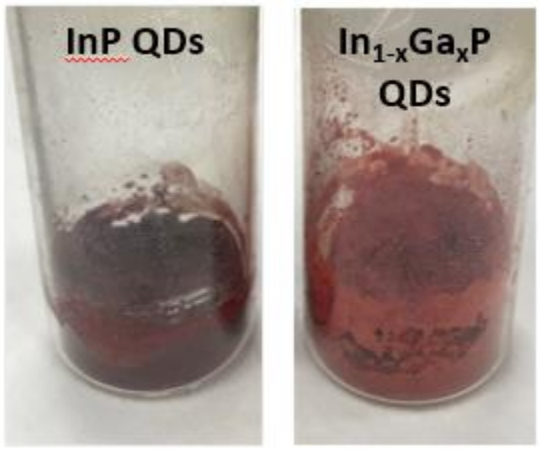

Figure 7.13. Photographs of InP QDs and $In_{1-x}Ga_xP$ QDs dispersed in CsBr:KBr:LiBr eutectic before and after the cation exchange reaction is performed at 400°C. The change in color is indicative of Ga incorporation.

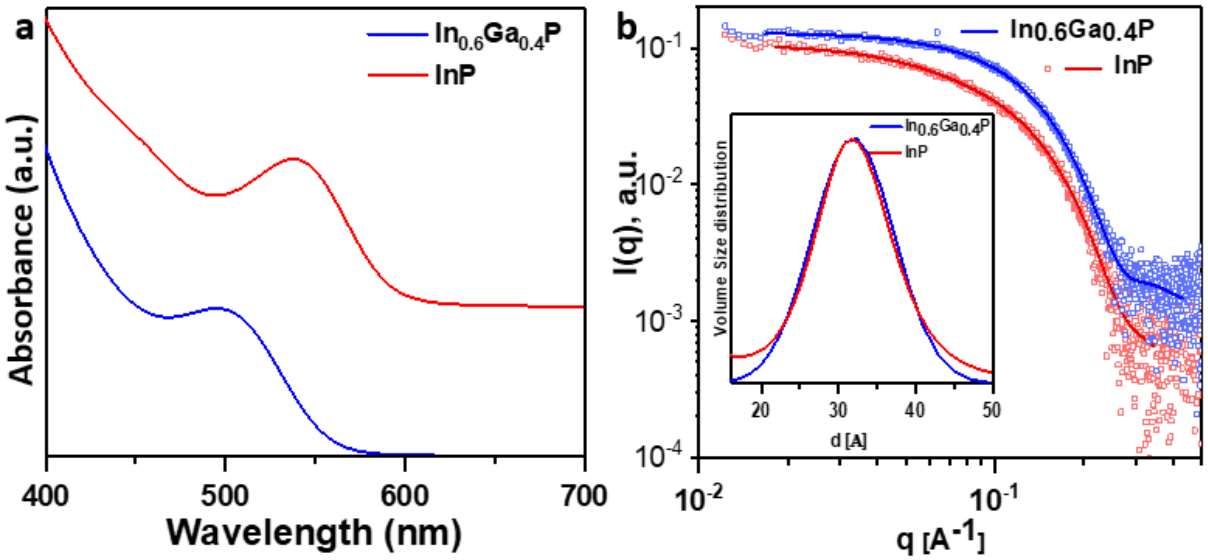

Figure 7.14. Quantifying the blue shift (a) Absorption spectra of InP and $In_{0.6}Ga_{0.4}P$ QDs of similar sizes (b) SAXS curves and corresponding fits for the QDs shown in panel (a). The size distribution fits in the inset show that the mean size and size distribution of both the samples are very similar to each other.

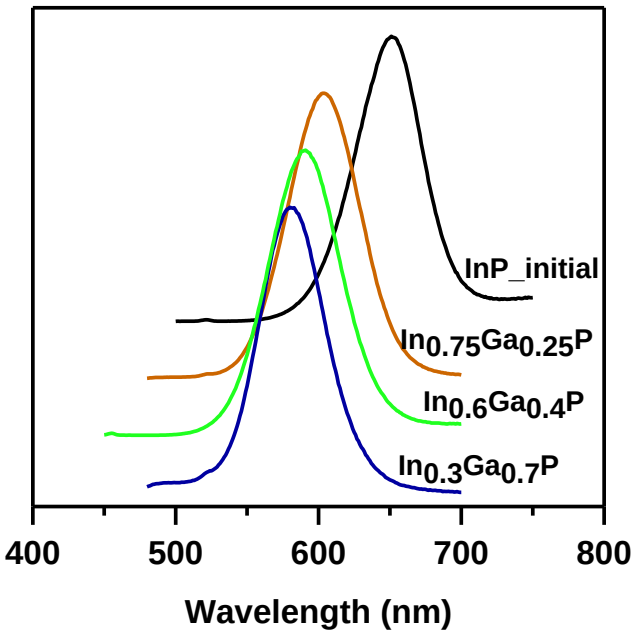

Figure 7.15. PL spectra of $In_{1-x}Ga_xP$ QDs and the starting InP QDs

7.5.2 ZnS shell growth on $In_{1-x}Ga_xP$ QDs

The emission quantum yields of $In_{1-x}Ga_{1-x}P$ QDs could be significantly enhanced upon shell growth. Core-only alloy QDs showed emission quantum yields in the range of 1-5% which increased to 46% upon ZnS shell growth (Figure 7.16a). Shell growth could be tracked by monitoring absorption below 350 nm (Figure 7.17). A type-I band alignment is expected for these core-shell QDs which is evidenced by the lack of substantial red-shift upon shell growth. We could prepare $In_{1-x}Ga_{1-x}P$ /ZnS core shell QDs emitting in the range of ~495 nm to ~640 nm with quantum yields in the range of 30-40% routinely observed across the size range (Figure 7.16b). The incorporation of 50% Ga in InP QDs should reduce the lattice mismatch with the ZnS shell from 7.5% to 4% which can substantially alleviate the interfacial strain between the core and shell.

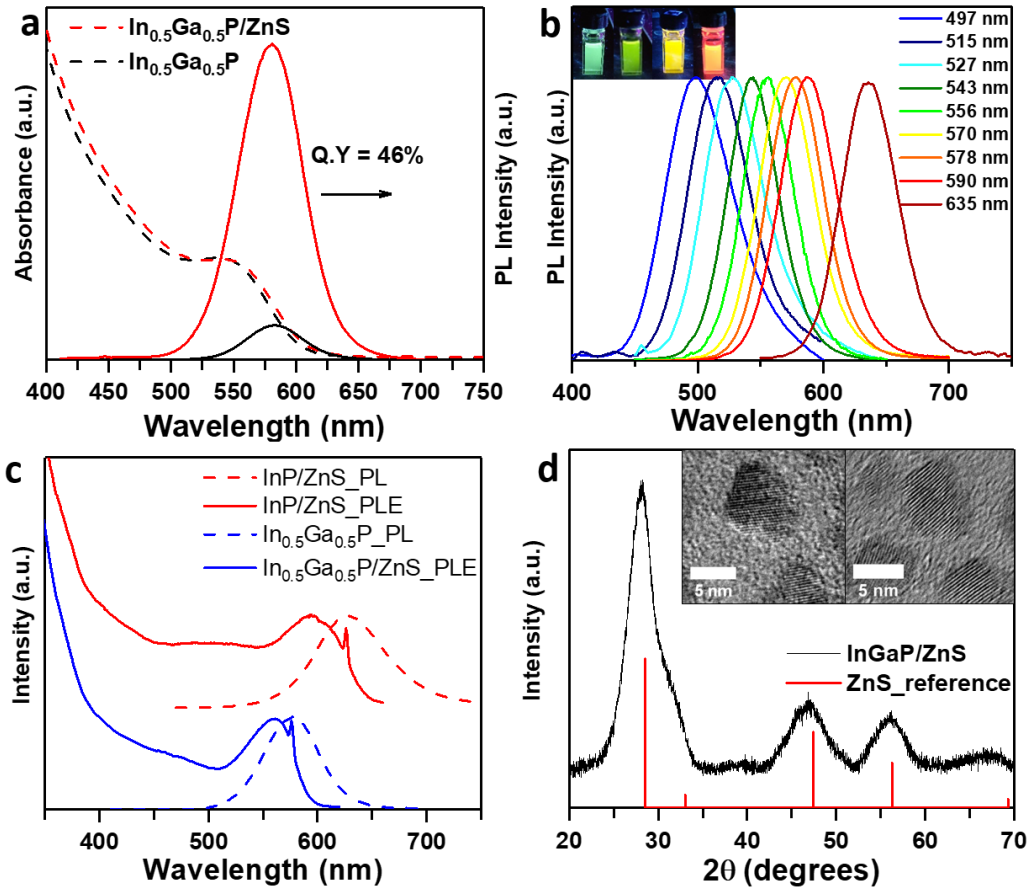

Figure 7.16. ZnS shell growth on $In_{1-x}Ga_xP$ QDs (a) Absorption and PL spectra of $In_{0.5}Ga_{0.5}P$ QD core (black solid and dashed) and $In_{0.5}Ga_{0.5}P$/ZnS core-shell QDs (red solid and dashed). The PL spectra depict the relative change in PL intensity upon shell growth. Data for InGaP/ZnS showing all details. (b) Representative PL spectra of $In_{1-x}Ga_xP$/ZnS core shell QDs extending the range between ~ 490 nm -640 nm showing the range of emission wavelengths accessible by this material. Inset shows photographs of dilute solutions of QDs illuminated by UV-lamp (c) A comparison of photoluminescence excitation (PLE) spectra for InP/ZnS QDs (blue) and $In_{0.5}Ga_{0.5}P$/ZnS QDs (red). The corresponding PL spectra are shown in dashed lines. PLE was measured at the corresponding emission maxima with a slit width of 2 nm. (d)X-ray diffraction pattern of $In_{0.6}Ga_{0.4}P$/ZnS QDs. Inset shows HR-TEM image of individual $In_{1-x}Ga_xP$/ZnS QDs showing clear lattice fringes for the core-shell particles.

We measured photoluminescence excitation spectra of $In_{0.5}Ga_{0.5}P$/ZnS and InP/ZnS core shell nanoparticles of similar sizes (Figure 7.16c). We observed narrower PLE spectra for $In_{0.5}Ga_{0.5}P$ /ZnS QDs in comparison to InP/ZnS QDs of similar sizes (Figure 7.16c). The broadening of PLE

spectra for InP/ZnS core shells can be attributed to the lattice strain in these systems. A graded composition of the $In_{1-x}Ga_xP$ core can also explain this observation which protects significant incorporation of Zn into the QD core thereby reducing disorder related Stokes shift. A series of PLE spectra collected at different positions of the emission band showed a significant distribution of transition energies in the ensemble (Figure 7.18). The X-ray diffraction pattern of $In_{0.6}Ga_{0.4}P$/ZnS QDs is shown in Figure 5d. HRTEM images showing lattices fringes are given in the inset (See Figure 7.19 for a large area TEM image).

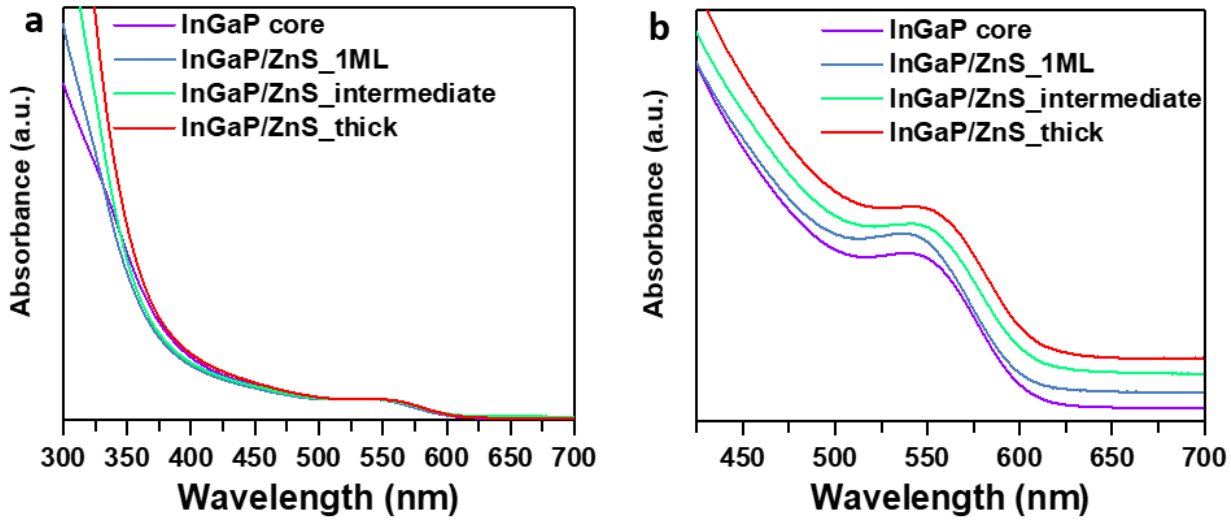

Figure 7.17. Tracking the shell growth (a) Absorption Spectra of InGaP/ZnS core shell QDs at various stages of shell growth. The increase in absorbance below 350 nm shows the increase in ZnS shell thickness. (b) Absorption Spectra of InGaP/ZnS core shell QDs showing the initial blue-shift in absorption maximum at the early stages of shell growth followed by a gradual red shift with increased shell thickness. The slight blue shift at the early stages of shell growth can be attributed to the slight etching of the core which has been previously observed for InP/ZnS QDs.[48]

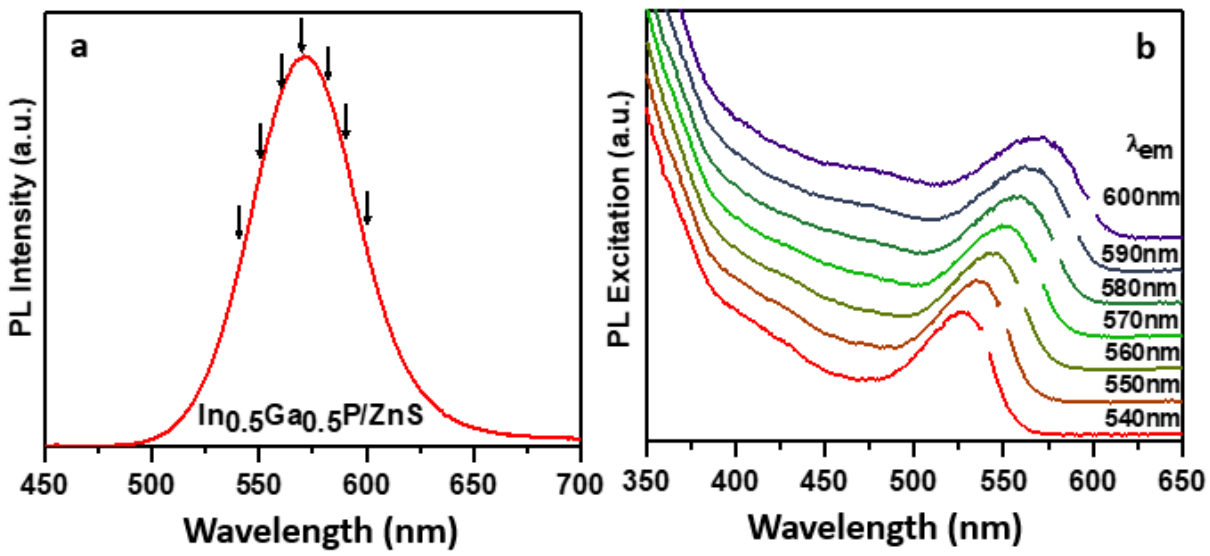

Figure 7.18. (a) PL emission spectrum of $In_{0.5}Ga_{0.5}P/ZnS$ QDs (b) Corresponding PL excitation spectra monitored at different emission wavelengths indicated by arrows in (a)

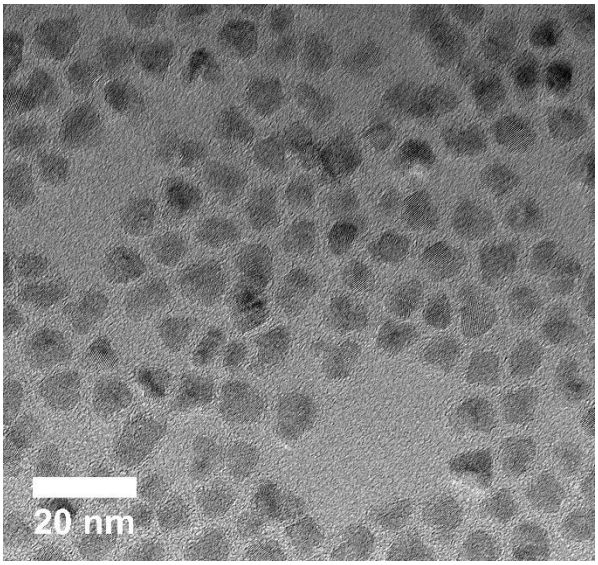

Figure 7.19. A large area TEM image of $In_{0.6}Ga_{0.4}P/ZnS$ core shell QDs

7.5.3 High temperature luminescence of $In_{1-x}Ga_xP$/ZnS QDs and its comparison to InP/ZnS QDs

For the technological implementation of QDs in LEDs, display panels and solar concentrators, the retention of luminescence efficiencies at high temperatures (upto 150°C) is an important requirement.[49-52] The loss in luminescence efficiency at high temperatures is typically attributed to thermally activated trapping of individual carriers.[50] Although luminescence retention at high temperatures is significantly enhanced upon shell growth, factors like core size, synthesis temperature and interfacial strain are known to play an important role in determining the thermal stability of photoluminescence.[52] We examined the effect of Ga incorporation on the thermal stability of photoluminescence in InP/ZnS QDs. We first measured the high temperature PL performance of QDs in solution and compared the results to InP/ZnS QDs. The alloy QDs retained their luminescence better than pure InP based QDs. (Figure 7.20). InP/ZnS QDs and the $In_{0.6}Ga_{0.4}P$/ZnS alloy QDs with similar core sizes were then immobilized in a crosslinked poly-(laurylmethacrylate) matrix and their PL was measured at elevated temperatures upon excitation with a 473 nm laser (Figures 7.21a and 7.21b) (See supporting information for experimental details). Whereas the PL of InP/ZnS QDs decreased drastically beyond 100°C and reduced to ~30% at 150°C, consistent with previous reports[51], the PL of $In_{0.6}Ga_{0.4}P$/ZnS NCs only decreased to ~60% upon heating to 150°C (Figure 7.21c). Similar results were obtained in solution (Figures 7.21d) We attribute this significantly better performance of the alloy QDs to the reduced lattice mismatch and the resultant low strain at the core-shell interface.

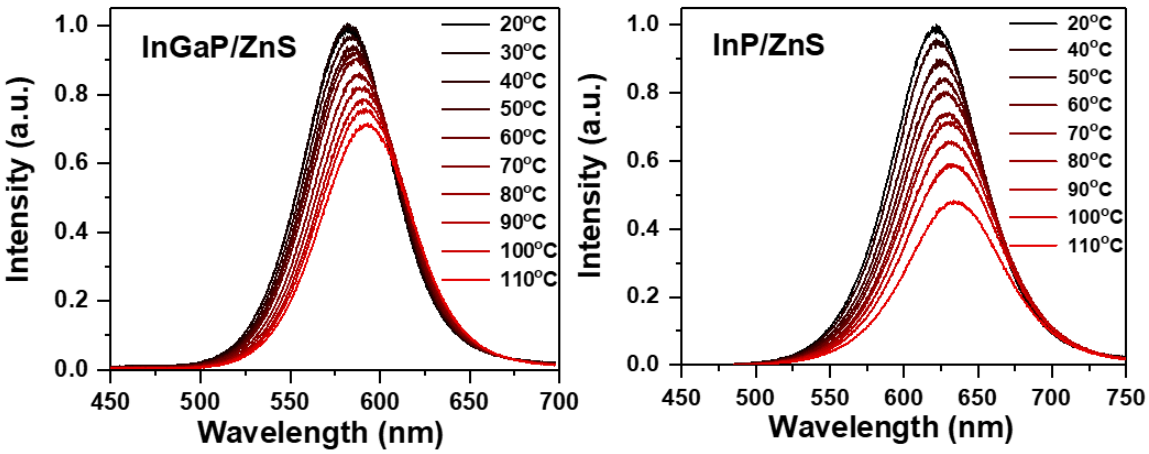

Figure 7.20. Temperature dependent PL spectra of $In_{0.6}Ga_{0.4}P$/ZnS QDs and InP/ZnS QDs dispersed in decane.

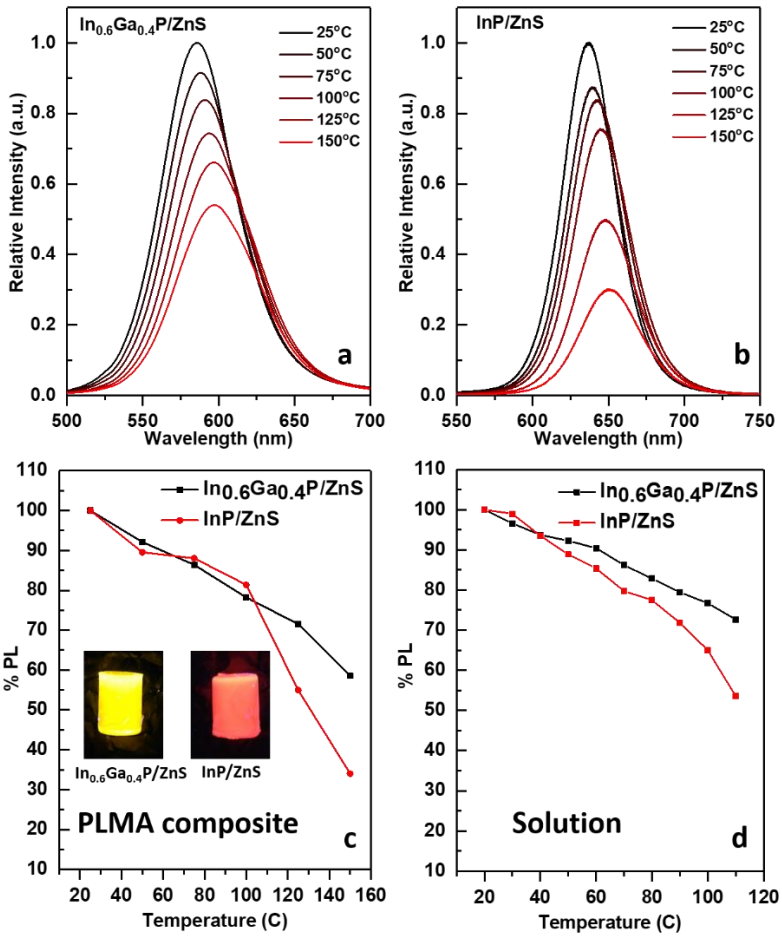

Figure 7.21. Temperature dependent PL spectra of (a) $In_{0.6}Ga_{0.4}P$/ZnS QDs and (b) InP/ZnS QDs immobilized in a matrix of cross-linked poly (lauryl methacrylate). (c) Change in integrated PL

area with increase in temperature for $In_{0.6}Ga_{0.4}P$/ZnS QDs and InP/ZnS QDs immobilized in a polymer matrix. Inset shows photographs of QD-polymer composites (d) Change in integrated PL area with increase in temperature for $In_{0.6}Ga_{0.4}P$/ZnS QDs and InP/ZnS QD solutions.

7.5.4 Optical Properties of Ternary $In_{1-x}Ga_xAs$ QDs and its core shells.

The optical properties of $In_{1-x}Ga_xAs$ alloy QDs were qualitatively similar to $In_{1-x}Ga_xP$ QDs. A continuous blue shift of the absorption edge was observed with increasing Ga content in the alloy QDs (Figure 7.22 a). The excitonic features of the alloys were broader as compared to the initial InAs QDs. Strong band-edge luminescence could be seen upon growing a shell of CdS on $In_{1-x}Ga_xAs$. Shell growth was accompanied by a slight red shift of the excitonic band, likely due to the leakage of the electron wavefunction into the shell. A highest quantum yield of 9.8% was obtained for $In_{0.5}Ga_{0.5}As$/CdS QDs with emission centered at ~860 nm (Figure 7.22b). Emission wavelength could be tuned in the biological tissue transparent window of ~750 nm-950 nm by simply varying the alloy composition (Figure 7.23). InAs QDs are being actively pursued as NIR emitting probes for in-vivo biological imaging.[13, 17] A potential disadvantage of InAs QDs for these applications is that InAs QDs have to be less than ~3 nm in size to emit in the window of ~700-950 nm which makes them rather unstable. Alloying of Ga in InAs QDs affords larger sized QDs emitting in this region. We estimated the size of $In_{0.5}Ga_{0.5}As$ QDs with an excitonic feature around~800 nm to be ~ 4 nm (Figure 7.24). We also measured 3D PL contour maps on luminescent $In_{0.5}Ga_{0.5}As$/CdS QDs to estimate the effect of size homogeneity on their absorption and emission properties (Figure 7.25). The diagonal elongation of spectra features in these PL intensity maps shows that the sample consists of an ensemble of QDs with a range of transition energies. Slicing of these maps gave a series of PL excitation spectra which showed narrow excitonic transitions (Figure 7.26). Similarly PL line narrowing experiments allowed us to selectively excite only a fraction of QDs in the ensemble which showed narrow PL spectra (Figure S22). Both these

experiments demonstrate that the broad emission linewidths in the alloy QDs are not inherent to the alloy and can be improved by further optimization of the synthesis conditions.

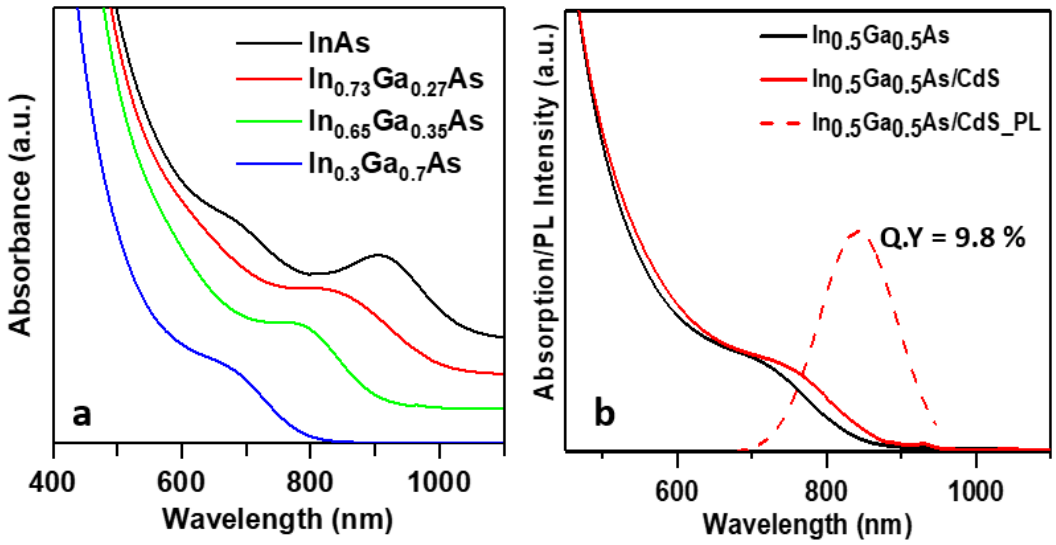

Figure 7.22 Optical properties of $In_{1-x}Ga_xAs$ QDs (a) Absorption spectra of starting InAs QDs, and $In_{1-x}Ga_xAs$ QDs synthesized from InAS QDs at different temperatures. (b) Absorption spectra (solid lines) of $In_{0.5}Ga_{0.5}As$ and $In_{0.5}Ga_{0.5}As$/CdS core-shell QDs and PL spectrum (dashed) of $In_{0.5}Ga_{0.5}As$/CdS core-shell QDs.

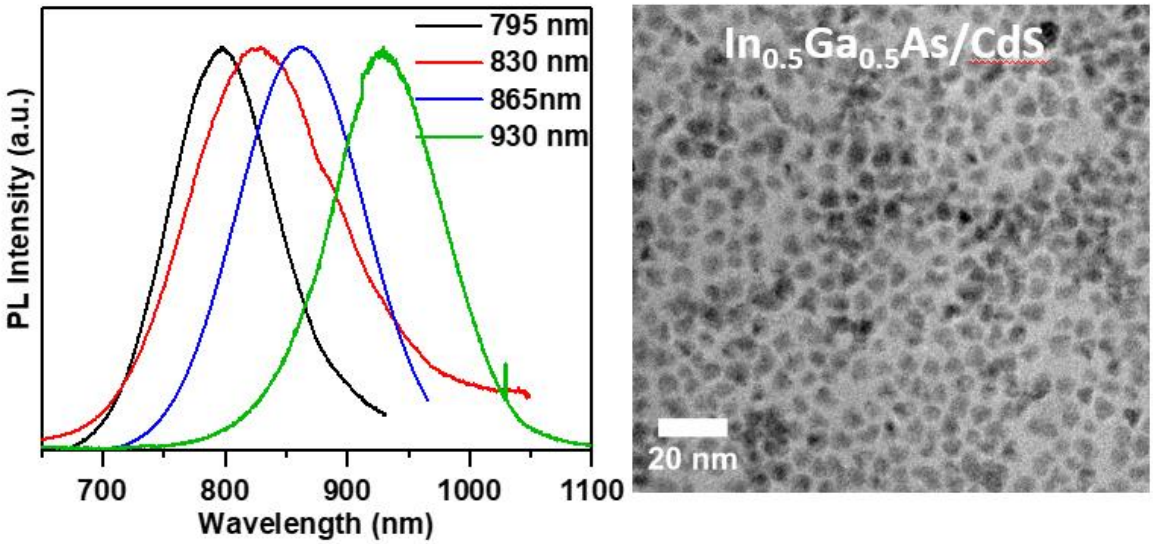

Figure 7.23. Representative Photoluminescence spectra and TEM image of $In_{1-x}Ga_xAs$/CdS QDs

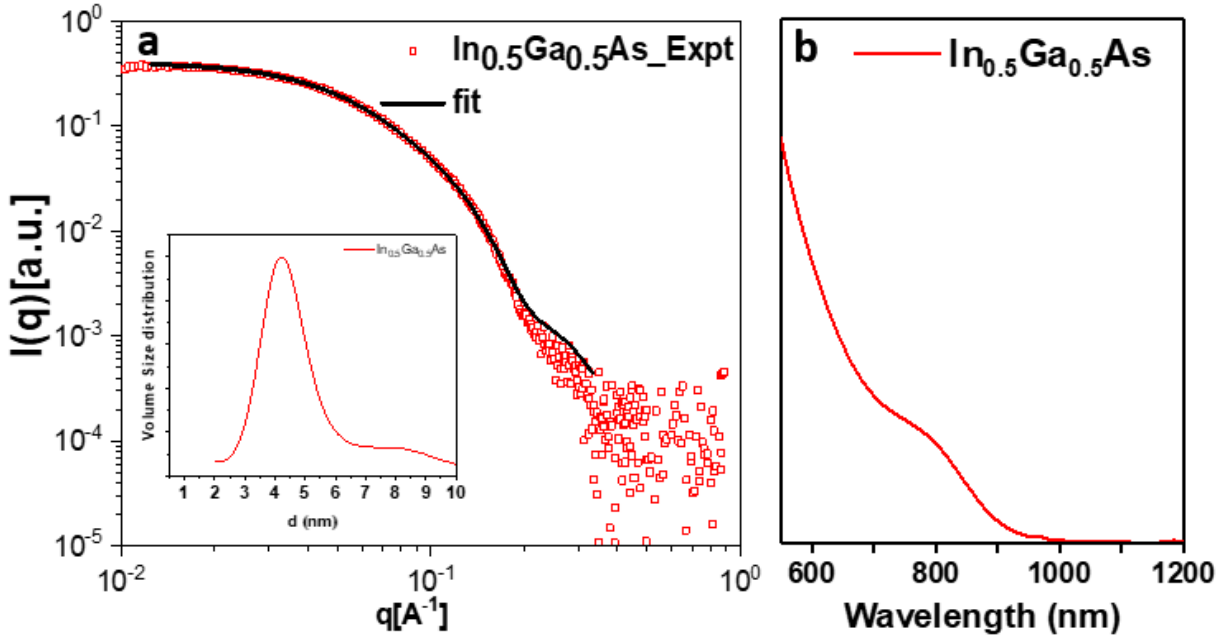

Figure 7.24. SAXS studies on $In_{0.5}Ga_{0.5}As$QDs (a) Small angle X-ray scattering curve and the corresponding fit for $In_{0.5}Ga_{0.5}As$QDs. Inset shows the size distribution extracted from the fit. (b) Absorption spectrum corresponding to the SAXS measurement.

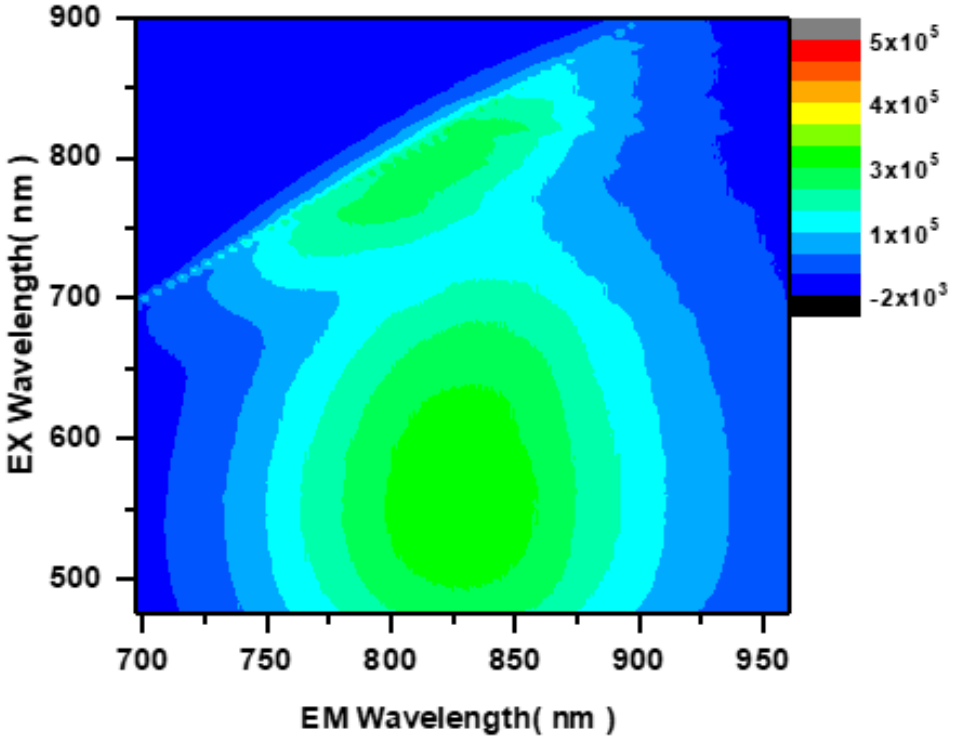

Figure 7.25. A two-dimensional PL map for $In_{0.5}Ga_{0.5}As$/CdS QDs. PL intensity is represented with a color map for every emission wavelength as a function of the excitation wavelength. The diagonal elongation represents heterogeneity of transition energies in the QD ensemble.

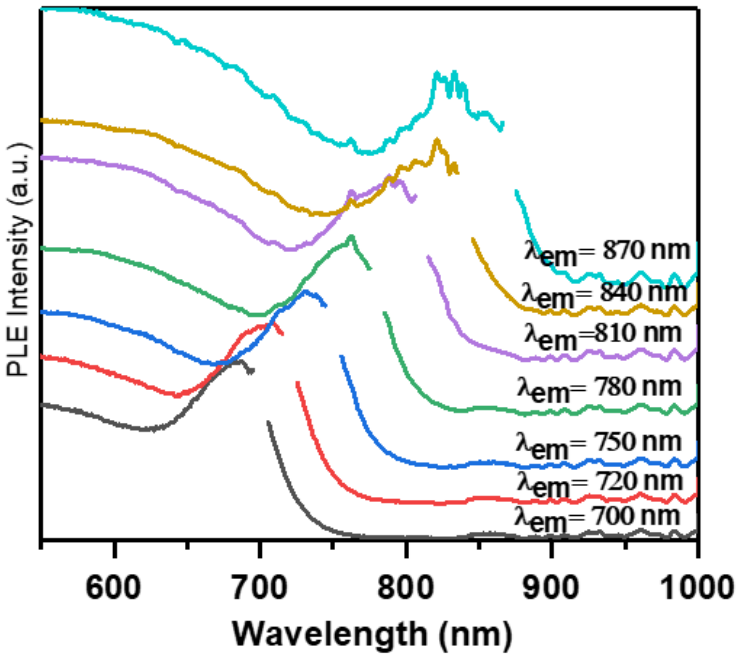

Figure 7.26. Individual PLE spectra at different emission energies sliced from the PL map shown in figure 7.25.

7.6 Conclusions

In summary, a novel approach to high temperature colloidal chemistry by using molten inorganic salts as solvents was described in this chapter. It is shown that InP and InAs QDs can be transformed into $In_{1-x}Ga_xP$ and $In_{1-x}Ga_xAs$ QDs by performing cation exchange reactions in molten salts at high temperatures without a significant change in their morphology. To the best of our knowledge, this work is the first report of cation exchange reactions in covalent III-V compounds. Both $In_{1-x}Ga_xP$ and $In_{1-x}Ga_x$ As QDs show blue shifted absorption compared to the starting materials and strong band edge emission can be observed from the alloy QDs. Nanocrystals phosphors based on InP/ZnE (E=S/Se) core shell structures are not yet on par with CdSe based core/shells in terms of both emission linewidth and quantum yields. This has been attributed to the incorporation of Zn into the InP lattice and significant interfacial strain between the III-V and II-VI core.[53] Creation of a graded III-V/II-VI interface can be useful to alleviate these issues. We

show that the ternary $In_{1-x}GaP$ QDs shelled with ZnS are potentially superior to InP/ZnS QDs in terms of their their optical properties. $In_{1-x}Ga_xAs$ based emitters are potential candidates for bio-imaging applications in the important NIR range of 750 nm -1000 nm. We believe that this work not only shows the power of molten salts as a novel platform for the synthesis of strongly covalent systems in a homogenous colloidal form but also demonstrates the advantage of cation exchange reactions as a lever for band-gap engineering of technologically relevant semiconductor QDs.

7.7 References

1. Adachi, S., *Physical properties of III-V semiconductor compounds*. John Wiley & Sons: 1992.
2. Geisz, J. F.; Kurtz, S. R.; Wanlass, M.; Ward, J.; Duda, A.; Friedman, D.; Olson, J.; McMahon, W.; Moriarty, T.; Kiehl, J. In *Inverted GaInP/(In) GaAs/InGaAs triple-junction solar cells with low-stress metamorphic bottom junctions*, Photovoltaic Specialists Conference, 2008. PVSC'08. 33rd IEEE, IEEE: 2008; pp 1-5.
3. A., G. M.; Yoshihiro, H.; D., D. E.; H., L. D.; Jochen, H. E.; W.Y., H. B. A., Solar cell efficiency tables (version 51). *Progress in Photovoltaics: Research and Applications* **2018,** *26* (1), 3-12.
4. Zhang, J.; Itzler, M. A.; Zbinden, H.; Pan, J.-W., Advances in InGaAs/InP single-photon detector systems for quantum communication. *Light: Science & Applications* **2015,** *4* (5), e286.
5. Owen, J.; Brus, L., Chemical Synthesis and Luminescence Applications of Colloidal Semiconductor Quantum Dots. *Journal of the American Chemical Society* **2017,** *139* (32), 10939-10943.
6. Lim, J.; Park, M.; Bae, W. K.; Lee, D.; Lee, S.; Lee, C.; Char, K., Highly efficient cadmium-free quantum dot light-emitting diodes enabled by the direct formation of excitons within InP@ ZnSeS quantum dots. *ACS nano* **2013,** *7* (10), 9019-9026.
7. Jo, J.-H.; Kim, J.-H.; Lee, K.-H.; Han, C.-Y.; Jang, E.-P.; Do, Y. R.; Yang, H., High-efficiency red electroluminescent device based on multishelled InP quantum dots. *Opt. Lett.* **2016,** *41* (17), 3984-3987.
8. Jang, J.; Liu, W.; Son, J. S.; Talapin, D. V., Temperature-Dependent Hall and Field-Effect Mobility in Strongly Coupled All-Inorganic Nanocrystal Arrays. *Nano Letters* **2014,** *14* (2), 653-662.
9. Bharali, D. J.; Lucey, D. W.; Jayakumar, H.; Pudavar, H. E.; Prasad, P. N., Folate-receptor-mediated delivery of InP quantum dots for bioimaging using confocal and two-photon microscopy. *Journal of the American Chemical Society* **2005,** *127* (32), 11364-11371.
10. Bruns, O. T.; Bischof, T. S.; Harris, D. K.; Franke, D.; Shi, Y.; Riedemann, L.; Bartelt, A.; Jaworski, F. B.; Carr, J. A.; Rowlands, C. J.; Wilson, M. W. B.; Chen, O.; Wei, H.; Hwang, G. W.; Montana, D. M.; Coropceanu, I.; Achorn, O. B.; Kloepper, J.; Heeren, J.; So, P. T. C.; Fukumura, D.; Jensen, K. F.; Jain, R. K.; Bawendi, M. G., Next-generation in vivo optical imaging with short-wave infrared quantum dots. *Nature Biomedical Engineering* **2017,** *1*, 0056.

11. Chibli, H.; Carlini, L.; Park, S.; Dimitrijevic, N. M.; Nadeau, J. L., Cytotoxicity of InP/ZnS quantum dots related to reactive oxygen species generation. *Nanoscale* **2011,** *3* (6), 2552-2559.
12. Lin, G.; Ouyang, Q.; Hu, R.; Ding, Z.; Tian, J.; Yin, F.; Xu, G.; Chen, Q.; Wang, X.; Yong, K.-T., In vivo toxicity assessment of non-cadmium quantum dots in BALB/c mice. *Nanomedicine: Nanotechnology, Biology and Medicine* **2015,** *11* (2), 341-350.
13. Allen, P. M.; Liu, W.; Chauhan, V. P.; Lee, J.; Ting, A. Y.; Fukumura, D.; Jain, R. K.; Bawendi, M. G., InAs(ZnCdS) Quantum Dots Optimized for Biological Imaging in the Near-Infrared. *Journal of the American Chemical Society* **2010,** *132* (2), 470-471.
14. Liu, W.; Chang, A. Y.; Schaller, R. D.; Talapin, D. V., Colloidal InSb Nanocrystals. *Journal of the American Chemical Society* **2012,** *134* (50), 20258-20261.
15. Ramasamy, P.; Kim, N.; Kang, Y.-S.; Ramirez, O.; Lee, J.-S., Tunable, Bright, and Narrow-Band Luminescence from Colloidal Indium Phosphide Quantum Dots. *Chemistry of Materials* **2017,** *29* (16), 6893-6899.
16. Srivastava, V.; Dunietz, E.; Kamysbayev, V.; Anderson, J. S.; Talapin, D. V., Monodisperse InAs quantum dots from aminoarsine precursors: understanding the role of reducing agent. *Chemistry of Materials* **2018**.
17. Franke, D.; Harris, D. K.; Chen, O.; Bruns, O. T.; Carr, J. A.; Wilson, M. W. B.; Bawendi, M. G., Continuous injection synthesis of indium arsenide quantum dots emissive in the short-wavelength infrared. *Nature Communications* **2016,** *7*, 12749.
18. Srivastava, V.; Liu, W.; Janke, E. M.; Kamysbayev, V.; Filatov, A. S.; Sun, C.-J.; Lee, B.; Rajh, T.; Schaller, R. D.; Talapin, D. V., Understanding and Curing Structural Defects in Colloidal GaAs Nanocrystals. *Nano Letters* **2017,** *17* (3), 2094-2101.
19. Lauth, J.; Strupeit, T.; Kornowski, A.; Weller, H., A Transmetalation Route for Colloidal GaAs Nanocrystals and Additional III–V Semiconductor Materials. *Chemistry of Materials* **2013,** *25* (8), 1377-1383.
20. Micic, O. I.; Sprague, J. R.; Curtis, C. J.; Jones, K. M.; Machol, J. L.; Nozik, A. J.; Giessen, H.; Fluegel, B.; Mohs, G.; Peyghambarian, N., Synthesis and Characterization of InP, GaP, and GaInP2 Quantum Dots. *The Journal of Physical Chemistry* **1995,** *99* (19), 7754-7759.
21. Kim, Y.-H.; Jun, Y.-w.; Jun, B.-H.; Lee, S.-M.; Cheon, J., Sterically Induced Shape and Crystalline Phase Control of GaP Nanocrystals. *Journal of the American Chemical Society* **2002,** *124* (46), 13656-13657.
22. Pietra, F.; Kirkwood, N.; De Trizio, L.; Hoekstra, A. W.; Kleibergen, L.; Renaud, N.; Koole, R.; Baesjou, P.; Manna, L.; Houtepen, A. J., Ga for Zn Cation Exchange Allows for Highly Luminescent and Photostable InZnP-Based Quantum Dots. *Chemistry of Materials* **2017,** *29* (12), 5192-5199.
23. Wang, X.; Ren, X.; Kahen, K.; Hahn, M. A.; Rajeswaran, M.; Maccagnano-Zacher, S.; Silcox, J.; Cragg, G. E.; Efros, A. L.; Krauss, T. D., Non-blinking semiconductor nanocrystals. *Nature* **2009,** *459*, 686.
24. Kim, S.; Kim, T.; Kang, M.; Kwak, S. K.; Yoo, T. W.; Park, L. S.; Yang, I.; Hwang, S.; Lee, J. E.; Kim, S. K.; Kim, S.-W., Highly Luminescent InP/GaP/ZnS Nanocrystals and Their Application to White Light-Emitting Diodes. *Journal of the American Chemical Society* **2012,** *134* (8), 3804-3809.
25. Park, J. P.; Lee, J.-j.; Kim, S.-W., Fabrication of GaAs, InxGa1–xAs and Their ZnSe Core/Shell Colloidal Quantum Dots. *Journal of the American Chemical Society* **2016,** *138* (51), 16568-16571.

26. Gerbec, J. A.; Magana, D.; Washington, A.; Strouse, G. F., Microwave-Enhanced Reaction Rates for Nanoparticle Synthesis. *Journal of the American Chemical Society* **2005,** *127* (45), 15791-15800.
27. De Trizio, L.; Manna, L., Forging Colloidal Nanostructures via Cation Exchange Reactions. *Chemical Reviews* **2016,** *116* (18), 10852-10887.
28. Son, D. H.; Hughes, S. M.; Yin, Y.; Paul Alivisatos, A., Cation Exchange Reactions in Ionic Nanocrystals. *Science* **2004,** *306* (5698), 1009-1012.
29. Beberwyck, B. J.; Alivisatos, A. P., Ion Exchange Synthesis of III–V Nanocrystals. *Journal of the American Chemical Society* **2012,** *134* (49), 19977-19980.
30. Shaw, D., *Atomic diffusion in semiconductors*. Springer Science & Business Media: 2012.
31. Zhang, H.; Dasbiswas, K.; Ludwig, N. B.; Han, G.; Lee, B.; Vaikuntanathan, S.; Talapin, D. V., Stable colloids in molten inorganic salts. *Nature* **2017,** *542*, 328.
32. Liu, X.; Fechler, N.; Antonietti, M., Salt melt synthesis of ceramics, semiconductors and carbon nanostructures. *Chemical Society Reviews* **2013,** *42* (21), 8237-8265.
33. Liu, X.; Giordano, C.; Antonietti, M., A molten-salt route for synthesis of Si and Ge nanoparticles: chemical reduction of oxides by electrons solvated in salt melt. *Journal of Materials Chemistry* **2012,** *22* (12), 5454-5459.
34. Liu, X.; Antonietti, M.; Giordano, C., Manipulation of Phase and Microstructure at Nanoscale for SiC in Molten Salt Synthesis. *Chemistry of Materials* **2013,** *25* (10), 2021-2027.
35. Kanady, J. S.; Leidinger, P.; Haas, A.; Titlbach, S.; Schunk, S.; Schierle-Arndt, K.; Crumlin, E. J.; Wu, C. H.; Alivisatos, A. P., Synthesis of Pt3Y and Other Early–Late Intermetallic Nanoparticles by Way of a Molten Reducing Agent. *Journal of the American Chemical Society* **2017,** *139* (16), 5672-5675.
36. Nag, A.; Kovalenko, M. V.; Lee, J.-S.; Liu, W.; Spokoyny, B.; Talapin, D. V., Metal-free Inorganic Ligands for Colloidal Nanocrystals: S2–, HS–, Se2–, HSe–, Te2–, HTe–, TeS32–, OH–, and NH2– as Surface Ligands. *Journal of the American Chemical Society* **2011,** *133* (27), 10612-10620.
37. Kovalenko, M. V.; Bodnarchuk, M. I.; Talapin, D. V., Nanocrystal Superlattices with Thermally Degradable Hybrid Inorganic−Organic Capping Ligands. *Journal of the American Chemical Society* **2010,** *132* (43), 15124-15126.
38. Zhang, H.; Jang, J.; Liu, W.; Talapin, D. V., Colloidal Nanocrystals with Inorganic Halide, Pseudohalide, and Halometallate Ligands. *ACS Nano* **2014,** *8* (7), 7359-7369.
39. Kyungnam, K.; Dongsuk, Y.; Hyekyoung, C.; Sudarsan, T.; Jae-Hyeon, K.; Sungwoo, K.; Yong-Hyun, K.; Sohee, J., Halide–Amine Co-Passivated Indium Phosphide Colloidal Quantum Dots in Tetrahedral Shape. *Angewandte Chemie International Edition* **2016,** *55* (11), 3714-3718.
40. Li, C.-J.; Li, P.; Wang, K.; Molina, E. E., Survey of properties of key single and mixture halide salts for potential application as high temperature heat transfer fluids for concentrated solar thermal power systems. *AIMS Energy* **2014,** *2* (2), 133-157.
41. Yamaguchi, K.; Takeda, Y.; Kameda, K.; Itagaki, K., Measurements of Heat of Formation of GaP, InP, GaAs, InAs, GaSb and InSb. *Materials Transactions, JIM* **1994,** *35* (9), 596-602.
42. Kornienko, N.; Whitmore, D. D.; Yu, Y.; Leone, S. R.; Yang, P., Solution Phase Synthesis of Indium Gallium Phosphide Alloy Nanowires. *ACS Nano* **2015,** *9* (4), 3951-3960.

43. Vurgaftman, I.; Meyer, J. R.; Ram-Mohan, L. R., Band parameters for III–V compound semiconductors and their alloys. *Journal of Applied Physics* **2001,** *89* (11), 5815-5875.
44. Kim, S.-W.; Zimmer, J. P.; Ohnishi, S.; Tracy, J. B.; Frangioni, J. V.; Bawendi, M. G., Engineering InAsxP1-x/InP/ZnSe III−V Alloyed Core/Shell Quantum Dots for the Near-Infrared. *Journal of the American Chemical Society* **2005,** *127* (30), 10526-10532.
45. Ramasamy, P.; Ko, K.-J.; Kang, J.-W.; Lee, J.-S., Two-Step "Seed-Mediated" Synthetic Approach to Colloidal Indium Phosphide Quantum Dots with High-Purity Photo- and Electroluminescence. *Chemistry of Materials* **2018**.
46. Yu, W. W.; Qu, L.; Guo, W.; Peng, X., Experimental Determination of the Extinction Coefficient of CdTe, CdSe, and CdS Nanocrystals. *Chemistry of Materials* **2003,** *15* (14), 2854-2860.
47. Xie, L.; Shen, Y.; Franke, D.; Sebastián, V.; Bawendi, M. G.; Jensen, K. F., Characterization of Indium Phosphide Quantum Dot Growth Intermediates Using MALDI-TOF Mass Spectrometry. *Journal of the American Chemical Society* **2016,** *138* (41), 13469-13472.
48. Ryu, E.; Kim, S.; Jang, E.; Jun, S.; Jang, H.; Kim, B.; Kim, S.-W., Step-Wise Synthesis of InP/ZnS Core−Shell Quantum Dots and the Role of Zinc Acetate. *Chemistry of Materials* **2009,** *21* (4), 573-575.
49. Zhao, Y.; Riemersma, C.; Pietra, F.; Koole, R.; de Mello Donegá, C.; Meijerink, A., High-Temperature Luminescence Quenching of Colloidal Quantum Dots. *ACS Nano* **2012,** *6* (10), 9058-9067.
50. Rowland, C. E.; Schaller, R. D., Exciton Fate in Semiconductor Nanocrystals at Elevated Temperatures: Hole Trapping Outcompetes Exciton Deactivation. *The Journal of Physical Chemistry C* **2013,** *117* (33), 17337-17343.
51. Rowland, C. E.; Liu, W.; Hannah, D. C.; Chan, M. K. Y.; Talapin, D. V.; Schaller, R. D., Thermal Stability of Colloidal InP Nanocrystals: Small Inorganic Ligands Boost High-Temperature Photoluminescence. *ACS Nano* **2014,** *8* (1), 977-985.
52. Diroll, B. T.; Murray, C. B., High-Temperature Photoluminescence of CdSe/CdS Core/Shell Nanoheterostructures. *ACS Nano* **2014,** *8* (6), 6466-6474.
53. Reid, K. R.; McBride, J. R.; Freymeyer, N. J.; Thal, L. B.; Rosenthal, S. J., Chemical Structure, Ensemble and Single-Particle Spectroscopy of Thick-Shell InP–ZnSe Quantum Dots. *Nano Letters* **2018,** *18* (2), 709-716.

Appendix A:
Characterization Techniques and Analysis

Transmission electron microscopy (TEM). The images were obtained using 300KV FEI Tecnai F30 microscope. Samples for TEM were prepared by depositing one droplet of diluted nanocrystal solution in toluene onto a lacey carbon grid from Ted Pella.

Optical absorption measurements. QDs dispersed in toluene or tetrachloroethylene (for IR absorbing materials) were used for absorption measurements. The absorption spectra of the solutions were collected using a Cary 5000 UV-Vis-NIR spectrophotometer. In order to estimate the molar extinction coefficient of NCs, the absorption of thoroughly washed samples of NCs in toluene were first measured and subsequently the concentration of the elements was measured using ICP-OES.

Photoluminescence Measurements

PL and PLE measurements were also performed in solutions. PL and PLE spectra were collected Horiba Fluorolog 3 equipped with Si CCD detector sensitive up to 1050 nm. For IR emission measurements, an InGaAs detector sensitive upto 1600 nm was used. High temperature PL measurements were done in decane as the solvents.

High temperature PL measurements on QD/Polymer composites were carried out on Horiba LabRamHR Evolution confocal Raman microscope. The composites were excited using a 473 nm laser operating at 0.1% of its power using a 50x long path objective. The PL was detected using the Synapse detector.

Wide-angle powder X-ray diffraction (XRD). The diffraction patterns were obtained using a Bruker D8 diffractometer with Cu Kα X-ray source operating at 40 KV and 40 mA and Vantec 2000 area detector.

Inductively coupled plasma optical emission spectroscopy (ICP-OES). ICP-OES analysis was carried out using Agilent 700 Series spectrometer. Samples were digested by a mixture of deionized ultrafiltered water and nitric acid (HNO_3, ≥69.0%, TraceSELECT, for trace analysis, from Sigma Aldrich) or aqua regia (HCl used for aqua regia is purchased from Sigma Aldrich, ≥37%, TraceSELECT, for trace analysis, fuming) in a plastic container.

Raman Spectroscopy Measurements. Raman spectra were collected on films deposited on glass using Horiba LabRamHR Evolution confocal Raman microscope. The samples were excited using a 532 nm laser.

Small-angle X-ray Scattering Measurements: SAXS on the colloidal NPs was collected on SAXSLab Ganesha instrument with Cu Kα radiation. The SAXS curves were analyzed by fitting to a quantitative model in Igor Pro using the Irena package (available at http://usaxs.xray.aps.anl.gov/staff/ilavsky/irena.html from the APS). [1] All scattering curves were firstly fitted with the model independent maximum entropy approach to make sure that the size distributions were symmetric Gaussian. Then the size distributions were extracted using Modelling II module in Irena package. Based on TEM data, the particles' form factor was assumed to be spherical with the aspect ratio of 1. SAXS data on NCs in molten salts were conducted at the XSD-CMS 12-ID-B beamline at the Advanced Photon Source, Argonne National Laboratory.

Transient Absorption Spectroscopy. TA measurements were performed using a 35 fs pulse width, 2 kHz commercial amplified Ti:sapphire laser operating at 800 nm. A portion (5%) of the

amplifier output was time-delayed and then focused into a sapphire plate to produce a UV-Vis white light probe. Except where indicated, the pump wavelength was 400 nm (1.55 eV), and the pump fluence was controllably varied between 0.005 to 2 mJ/cm^2

Extended x-ray absorption fine structure (EXAFS). EXAFS measurements were conducted at the beamlines 20-ID and 20-BM at the Advanced Photon Source, Argonne National Laboratory. Measurements were collected at the As K edge (11,867 eV) and Ga K edge (10,367 eV) for solutions of GaAs NCs and GaAs powder. Solution samples were measured in plastic cuvettes sealed under nitrogen and GaAs powder was prepared as a pellet diluted with BN and sealed in Kapton tape. Reference spectra for the Ga and As edges were measured on Ga and As standards, respectively. Data reduction and analysis were conducted with the Demeter suite of x-ray absorption spectroscopy software.[2]

Electron Paramagnetic Resonance (EPR): EPR measurements were carried out on an X-Band Bruker ESP300E spectrometer equipped with a Varian rectangular cavity TE102 and a variable temperature cryostat (Air Products) cooled to liquid helium temperatures.

Estimation of Quantum Yields

Quantum yields were calculated with respect to Rhodamine 6G (for $In_{1-x}Ga_xP$) or IR-125 dye (for $In_{1-x}Ga_xAs$) as the reference dyes with solution optical density at the excitation wavelength between 0.05 and 0.1. PL spectra were taken and the integrated areas are used in the following calculation of quantum yield:

$$\varphi = \varphi_{ref} \frac{I_x}{I_{ref}} \frac{A_{ref}}{A_x} \frac{\eta_{st}^2}{\eta_{ref}^2}$$

Where x is the sample and ref is Rhodamine 6G/IR-125. The quantum yield of Rhodamine 6G was taken as 0.95 and IR-125 as 0.134. I represents the integrated emission intensity, A represents the

optical density in the absorption spectra, and n representing the refractive indices of the solvents. It is important to note that the samples were excited at the wavelength where optical density is equal.

Estimation of Molar Extinction Coefficients

In order to estimate the values of the molar extinction coefficient of InP, GaAs and $In_{1-x}Ga_xP$ QDs, we characterized thoroughly washed samples by UV-Vis spectroscopy and subsequently dissolved the particles in aqueous HNO_3 digesting solution. The total metal concentration of each sample was determined by ICP-OES. Once the metal concentrations were determined, the particle concentrations were calculated by using bulk lattice parameters and the average particle size which were determined by TEM and SAXS measurements.

References:

1. Ilavsky, J. & Jemian, P. R. Irena: tool suite for modeling and analysis of small-angle scattering. *J. Appl. Cryst.* **2009**, *42*, 347–353.
2. Ravel, B.; Newville, M., ATHENA, ARTEMIS, HEPHAESTUS: data analysis for X-ray absorption spectroscopy using IFEFFIT. *J Synchrotron Radiat* **2005,** *12* (4), 537-541.

Appendix B:

Synthesis of Nanocrystals based on reported protocols

Synthesis of Small InP QDs

Small InP QDs (λ_{max} = 500-540 nm) were synthesized using a slight modification of a reported protocol.[1] Indium acetate (0.45 mmol) and oleic acid (1.4 mmol) were mixed with 10 mL of ODE in a 50 mL three-neck flask and fixed to a Schlenk line with a reflux condenser. The mixture was heated to 120 °C under vacuum for 1 h. Then, the flask was refilled with N_2 and cooled to RT. Then, a solution containing 0.3 mmol (0.25 for particles with λmax =540 nm) of $(TMS)_3P$ and 1 mL of TOP was quickly injected into the flask. Following the injection, the mixture was heated to 305 °C (15 °C/min) and kept at that temperature for 2 min before cooling to RT. The QDs were precipitated with 50 mL of ethanol and collected by centrifugation. The QDs were washed three times by dispersion in hexane, followed by precipitation by addition of ethanol, and stored in hexane in a vial in a N2 filled glovebox.

Synthesis of large InP QDs

Large InP QDs (λ_{max} > 600 nm) were synthesized using a slight modification of reported protocol.[2] Indium acetate (0.45 mmol) and myristic acid (4-6 equivalent, depending on size) were mixed with 10 mL of ODE in a 50 mL three-neck flask and fixed to a Schlenk line with a reflux condenser. The mixture was heated to 120 °C under vacuum for 1 h. Then, the flask was refilled with N_2 and cooled to RT. Then, a solution containing 0.3 mmol (0.25 for particles with λmax =540 nm) of $(TMS)_3P$ and 1 mL of TOP was quickly injected into the flask. Following the injection, the mixture was heated to 305 °C (15 °C/min) and kept at that temperature for 2 min before cooling to RT. The

QDs were precipitated with 50 mL of ethanol and collected by centrifugation. The QDs were washed three times by dispersion in hexane, followed by precipitation by addition of ethanol, and stored in hexane in a vial in a N_2 filled glovebox.

Synthesis of InAs QDs

InAs QDs were synthesized according to protocols detailed in Chapters 2 and 3.

Synthesis of Pt NCs

Pt NCs, ~5 nm in diameter were synthesized based on a reported protocol.[3] Briefly $Pt(acac)_2$ (0.1 g), octadecene (10 mL), oleic acid (OA) (1 mL), and oleylamine (OAm) (1 mL) were mixed under N_2 in a 50 mL 3-neck flask. The mixture was then heated to ~70°C to dissolve $Pt(acac)_2$. The temperature was then raised to about 200°C. 0.1 mL of a stock solution of $Fe(CO)_5$ in hexane (Stock solution: 0.1 mL $Fe(CO)_5$ in 1 mL hexane under argon) was quickly injected into the hot solution. The solution was kept at 200°C for 1 hour before it was cooled down to room temperature. 40 mL of isopropanol was added and then the suspension was centrifuged to separate the NCs. The particles were washed twice from hexane by adding ethanol. The final product was dispersed in10 mL of hexane for further use.

References

1. Ramasamy, P.; Kim, N.; Kang, Y.-S.; Ramirez, O.; Lee, J.-S., Tunable, Bright, and Narrow-Band Luminescence from Colloidal Indium Phosphide Quantum Dots. *Chemistry of Materials* **2017,** *29* (16), 6893-6899.
2. Battaglia, D.; Peng, X., Formation of High Quality InP and InAs Nanocrystals in a Noncoordinating Solvent. *Nano Letters* **2002,** *2* (9), 1027-1030.
3. Chao, W.; Hideo, D.; Taigo, O.; Tetsunori, K.; Shouheng, S., A General Approach to the Size- and Shape-Controlled Synthesis of Platinum Nanoparticles and Their Catalytic Reduction of Oxygen. *Angewandte Chemie* **2008,** *120* (19), 3644-3647.

Appendix C:

Synthesis of AsH_3

It is important to note that Arsine is an extremely dangerous gas and must be handled with appropriate caution. Arsine was produced by reacting Zn_3As_2 with dilute sulfuric acid ($1H_2SO_4$:$2H_2O$) at room temperature. 6.2 g of Zn_3As_2 was loaded into a 100 mL 3-neck flask inside a glove box. The flask was quickly transferred to the schlenk line and attached to the setup shown in Figure 1. 24mL of dilute H_2SO_4 was then quickly injected into the flask and bubbles could be seen which indicated the production of AsH_3 gas. AsH_3 gas is then passed through dessicants phosphorus pentoxide (P_2O_5) and sodium hydroxide (NaOH) with the help of N_2 as the carrier gas, before it condenses in liquid N_2 trap. For further use, the solidified arsine can be evaporated with the help of acetone/dry-ice bath which has a temperature close to the boiling point of arsine (-62°C). Saturated solution of aqueous $CuSO_4$ is used to quench the residual Arsine.

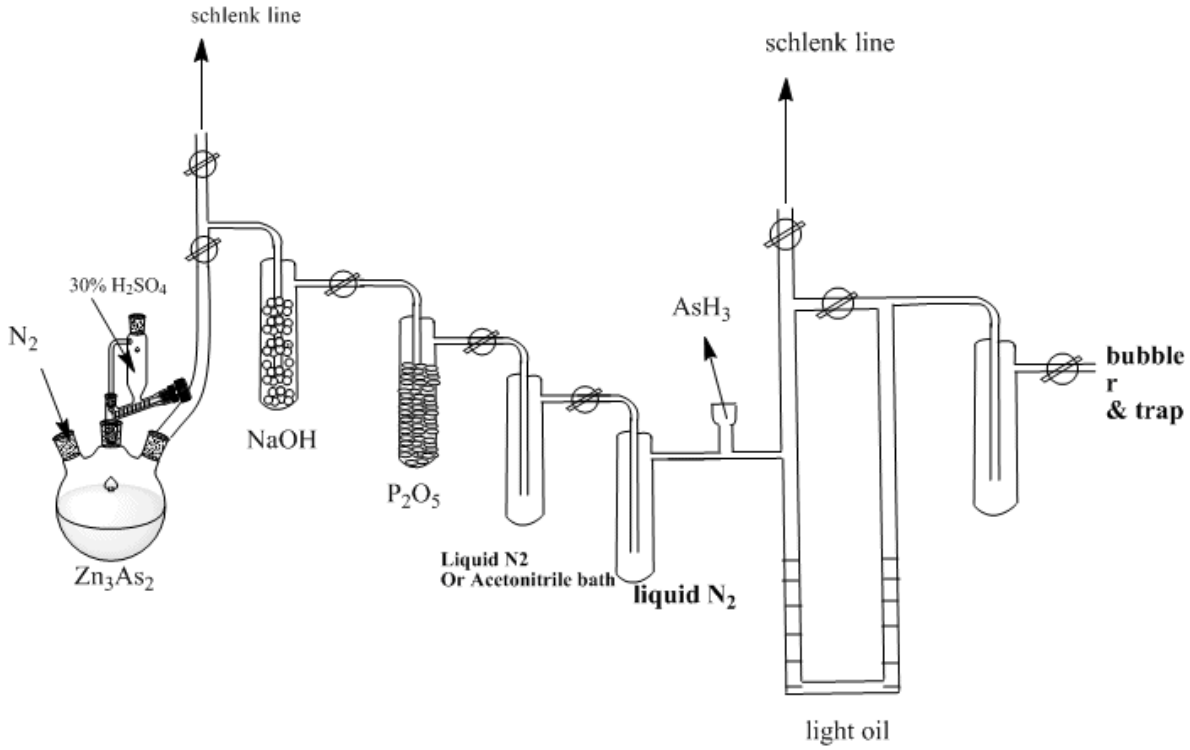

Figure AP1. Scheme for AsH_3 synthesis and handling.